

© Copyright by Charles Plager, 2003

Version 1.1.9

A SEARCH FOR CP VIOLATION IN, AND A DALITZ ANALYSIS OF
 $D^0 \rightarrow \pi^- \pi^+ \pi^0$ DECAYS IN CLEO II.V

BY

CHARLES PLAGER

B.S., University of Illinois at Urbana-Champaign, 1992
M.S., University of Illinois at Urbana-Champaign, 1995

THESIS

Submitted in partial fulfillment of the requirements
for the degree of Doctor of Philosophy in Physics
in the Graduate College of the
University of Illinois at Urbana-Champaign, 2003

Urbana, Illinois

A SEARCH FOR CP VIOLATION IN, AND A DALITZ ANALYSIS OF
 $D^0 \rightarrow \pi^- \pi^+ \pi^0$ DECAYS IN CLEO II.V

Charles Plager, Ph.D.
Department of Physics
University of Illinois at Urbana-Champaign, 2003
Prof. Mats Selen, Advisor

Using the $9fb^{-1}$ data sample collected with the CLEO II.V detector at the Cornell Electron Storage Ring, we study the resonant substructure of the Cabibbo suppressed decay $D^0 \rightarrow \pi^+ \pi^- \pi^0$. We observe significant contributions from the $\rho^- \pi^+$, $\rho^+ \pi^-$, $\rho^0 \pi^0$, and non-resonant channels, and present results of the amplitudes, phases, and fit fractions for these and other sub-modes. No significant evidence for the $\sigma(500)$ or any other resonance was found. \mathcal{A}_{CP} has been measured as $0.01^{+0.09}_{-0.07} \pm 0.09$.

Acknowledgements

During ~~my five year~~, ~~my eight year~~, my really long career as a graduate student, there have been *many* people who have helped and supported me. A complete list is not possible, but I will do my best.

I would like to start by thanking my wife, Kate. Without her love, patience, understanding, and support, I don't think that it would have been possible to finish.

The biggest work influence has been far and away due to my advisor, Mats Selen. I want to thank him for showing me what kind of physicist I can be and what type of boss I want to be. The Illinois CLEO faculty, Jon Thaler, Bob Eisenstein, George Gollin, Gary Gladding, and Inga Karliner have all been invaluable sources of support and knowledge. The three Illinois postdoctoral researchers, Randal Hans, Mark Palmer, and Jesse Ernst were there day in and day out when I needed them. It is because of them that I have impossibly high standards I do for what a post doc should be. And what would graduate school be if not for the other graduate students. Those who came before me, Tim Bergfeld and Ed Johnson, my contemporaries, Mike Marsh, Chris Sedlack, and Jeremy Williams, and the “youngsters”, Norm Lowrey, Scott Davis, and Paras Naik all had very positive impacts on my extended stay. As for our new post-doc Topher Cawfield, I'll use his own words (written on an early copy of my thesis he was proofreading): *And last and probably not least, I'd like to thank Topher Cawfield, for without his friendship, help, support, and interest in the CLEO III Trigger, I would have graduated months ago.*

At Wilson Lab, there are many people who made this journey a pleasant one.

David Kreinick, Jim Alexander, and Ed Thorndike have all been role models as well as great sources of advice. I would be remiss if I didn't mention Tom Meyer, Andreas Warburton, Steve Pappas and all of my fellow "worker bees" for many many hours of amusement, camaraderie, and support. The CLEO collaboration as a whole also gets a big thanks. The years I have spent working on CLEO are some of the happiest and most fulfilling in my life. I hope that I have left as good an impression on them as they have on me.

None of this would have been possible without the behind (and in front of) the scenes support from many people. I (and the whole trigger group) owe a huge debt of gratitude to Mike Haney and the rest of the high energy engineering group. The computing, both at Illinois and Cornell, have been outstanding, and I would like to particularly thank David Lesny, Mike Roman, Rich Shultys, and Seldon Ball. Tom Shaw, Donna Guzy, and Joyce Ruch have all made being an Illinois graduate student off in a strange land as painless as possible.

David Saltzberg, Jay Hauser, and the rest of the UCLA high energy physics group also deserve mention. It was much easier to leave Illinois and CLEO knowing that I was moving to UCLA and the CDF experiment at Fermilab.

The support given to me by my parents, Shelly and Max, and my sister, Debbie has been non-stop and greatly appreciated. I would like to thank them for having faith in me all of these years that I would finish.

It would be most unfortunate if I left out the physics teacher from with whom I have spent the most time in the classroom. Mr. Gilbert Martin was my high school physics teacher my freshman and senior years. This class was far and away the best I ever took in high school, both in terms of how much I learned and how much fun I had.

Last but definitely not least, I would like to thank three individuals who went well above the call of duty. Jean and Howard Osborn and Lynn Phillips all housed me for much longer than I had any reason to expect they would when I was temporarily homeless. In both cases, I was made to feel at home and I can't thank them enough

for that.

This material is based upon work supported by the National Science Foundation under Grant PHY 9553157 FFW and the Department of Energy under Grant DE FG02 91ER40677.

Contents

Chapter 1 Introduction	1
1.1 The Standard Model	1
1.2 The CKM Matrix	4
1.3 CP Violation	5
1.3.1 Parity Symmetry	6
1.3.2 Charge Conjugation Symmetry	7
1.3.3 CP	7
1.3.4 The CKM Matrix, Revisited	9
1.4 A Brief Review of Relativistic Mechanics	10
1.5 An Event at CLEO	10
1.6 Finding $D^0 \rightarrow \pi^- \pi^+ \pi^0$ Events	12
1.7 A Quick Word About Units	14
1.7.1 Electron-Volts	14
1.7.2 Luminosity and Cross Sections	15
Chapter 2 Cæsar and Cleopatra	19
2.1 CESR	19
2.2 CLEO II.V	21
2.2.1 The Silicon Vertex Detector	24
2.2.2 Drift Chambers	25
2.2.3 Time of Flight	27
2.2.4 Crystal Calorimeter	28

2.2.5	Superconducting Magnet	28
2.2.6	Muon Detector	29
2.2.7	Data Acquisition and Trigger	29
2.3	Particle Identification	30
2.4	Monte Carlo	32
Chapter 3 Dalitz Analysis of $D^0 \rightarrow \pi^- \pi^+ \pi^0$		34
3.1	Introduction	34
3.1.1	Motivation	34
3.1.2	Three Body Decays	35
3.1.3	Dalitz Plots	37
3.2	Theory	38
3.2.1	Representations of the Resonances	38
3.2.2	How We Treat $D^0 \rightarrow K_S^0 \pi^0$	44
3.3	Analysis	45
3.3.1	General Overview	46
3.3.2	Event Selection	49
3.3.3	Possible Resonances	52
3.4	Dalitz Fitter	52
3.4.1	Theory	52
3.4.2	Fitter	56
3.4.3	Goodness of Fit	57
3.4.4	Fit Fractions	58
3.4.5	\mathcal{A}_{CP}	59
3.5	Efficiency	63
3.6	Background	64
3.7	Signal Fraction	67
3.8	Results	69
3.8.1	\mathcal{A}_{CP}	78

3.9	Systematic Errors	80
3.9.1	General Method	80
3.9.2	Efficiency	80
3.9.3	Background	80
3.9.4	Signal Fraction	82
3.9.5	Event Selection	82
3.9.6	Total Systematic Errors	82
3.10	Final Results	88
3.11	Conclusions	89
Chapter 4 The CLEO III Trigger		90
4.1	CLEO III Detector	90
4.2	Trigger Requirements and Realities	90
4.3	Hardware Implementation	93
4.4	Crystal Calorimeter Trigger	94
4.4.1	Analog Crystal Calorimeter Trigger	95
4.4.2	Digital Crystal Calorimeter Trigger	96
4.5	Tracking Trigger	97
4.5.1	Axial Tracking Trigger	99
4.5.2	Stereo Tracking Trigger	100
4.5.3	The Axial Processor and the Tracking Correlator	101
4.6	The Level 1 Decision and Data Flow Control	103
4.7	The CLEO III Stereo Trigger In Depth	105
4.7.1	Simulation Basics	105
4.7.2	Stereo Blocks	105
4.7.3	Stereo Trigger Tracks	108
4.7.4	Maintenance	109
Chapter 5 Final Remarks		113

Appendix A Driver++ Analysis Tools	114
A.1 Driver	114
A.2 C++ access to FORTRAN common blocks	115
A.3 Additional Tools	116
Appendix B Block patterns for the Stereo Trigger	119
B.1 The Patterns	119
B.2 Superlayer 8	119
References	125
Vita	127

List of Figures

1.1	Feynman Diagrams for $D^{*+} \rightarrow D^0\pi^+$, $D^0 \rightarrow \pi^-\pi^+\pi^0$	3
1.2	$e^+e^- \rightarrow c\bar{c}$ at $t = 0$ s	11
1.3	Hadronization at $t \sim 10^{-23}$ s	12
1.4	Strong decays at $t \sim 10^{-20}$ s	13
1.5	Weak decays at $t \sim 10^{-12}$ s	14
1.6	Particles are Observed by CLEO at $t \sim 10^{-9}$ s	15
1.7	Ideal D^0 Mass Distribution	16
1.8	D^0 Mass Distribution for Signal Events Only	16
1.9	D^0 Mass Distribution for All Events	17
1.10	Actual D^0 Mass Distribution	18
2.1	Layout of CESR	20
2.2	CESR Pretzel	22
2.3	CLEO	23
2.4	SVX Detector	24
2.5	VD Detector	26
2.6	Main Drift Chamber	27
2.7	dE/dx Distributions	31
3.1	$D^0 \rightarrow ABC$ through an AB Resonance.	35
3.2	Examples of Feynman Diagrams for $D^0 \rightarrow \pi^-\pi^+\pi^0$	36
3.3	Dalitz Plot of $D^0 \rightarrow \pi^-\pi^+\pi^0$ from Data	39
3.4	Dalitz Plot and Projections	40

3.5	Dalitz Plot and Rotated Projections	41
3.6	Angular Distribution of $D^0 \rightarrow \rho^0\pi^0$	44
3.7	Amplitude Distribution of $D^0 \rightarrow \rho^0\pi^0$	45
3.8	D^0 Mass Distributions with Mass Difference Cuts	47
3.9	Vertexing Slow Pion	49
3.10	π^0 Cuts	51
3.11	D^0 Mass Cuts	53
3.12	Mass Difference Cuts	54
3.13	D^{*+} Momentum Fraction Cuts	55
3.14	Binning for Calculating χ^2	58
3.15	Fit Fraction Error Distributions	60
3.16	Efficiency Fits	64
3.17	Sidebands	65
3.18	Background Fits	69
3.19	Signal Fraction from D^0 Mass and Mass Difference Distributions	70
3.20	\mathcal{A}_{CP} Results	79
4.1	CLEO III Detector	91
4.2	CLEO III Trigger Timing	92
4.3	CLEO III Trigger Overview	94
4.4	Trigger Board Overview	95
4.5	CC Tiles Turn-on Curves	97
4.6	TilePro Functions	98
4.7	AXTR Functions	99
4.8	STTR Functions	100
4.9	AXPR Timing Algorithm	102
4.10	Blocks 19 through 21 in Superlayer 6	107
4.11	Block 20 Patterns	108
4.12	Layout of Stereo Section of Drift Chamber	112

B.1	Patterns for Superlayers 1 - 7	120
B.2	Patterns for Superlayer 8	123

Chapter 1

Introduction

1.1 The Standard Model

Our current understanding of matter is that it is made up of spin $\frac{1}{2}$ fermions and that these fermions interact through spin 1 gauge bosons.¹ The fermions are further divided into two distinct types: quarks and leptons.

The six types of leptons are often grouped into three generations as follows:

$$\begin{pmatrix} e^- \\ \nu_e \end{pmatrix}, \begin{pmatrix} \mu^- \\ \nu_\mu \end{pmatrix}, \begin{pmatrix} \tau^- \\ \nu_\tau \end{pmatrix}$$

The top row of leptons all have the same electric charge and vary in mass from $511 \text{ keV}/c^2$ for the electron up to $1.78 \text{ GeV}/c^2$ for the tau. The bottom row neutrinos all have zero electric charge and are almost² massless.

As with the leptons, the six flavors of quarks are grouped into three generations:

$$\begin{pmatrix} u \\ d \end{pmatrix}, \begin{pmatrix} c \\ s \end{pmatrix}, \begin{pmatrix} t \\ b \end{pmatrix}$$

¹Gravity may turn out to be mediated by a spin 2 or higher gauge bosons.

²The least studied neutrino (the tau neutrino) has its mass measured to be less than $18 \text{ MeV}/c^2$ [1]. Recent experimental results indicate that at least some (if not all) of the neutrinos have mass, albeit tiny.[2]

The upper quarks all have an electric charge of two-thirds the charge of the proton, and the lower quarks all have an electric charge of minus one-third of the proton's charge. In addition, quarks also have a "color" charge (see below).

Every particle (i.e. all quarks and all leptons) has an anti-particle that has the opposite electric and color charge but the same mass and spin.

There are four known forces: strong, electromagnetic, weak and gravity. Of these forces, only the first three are important on the scales that we are investigating. Other than gravity, the electromagnetic force is what people are most familiar with. It is mediated by massless photons and only affects particles with electric charge (i.e. all of the quarks and the charged leptons). Photons themselves do not have any charge and therefore will not interact with other photons. An example of the electromagnetic force in action is the binding of electrons to the nuclei of atoms.

The strong force is the strongest of the three, but only acts at very short distances. It is mediated by massless gluons and only affects particles with color charge (i.e. all of the quarks and none of the leptons). Unlike photons, gluons themselves do carry color charge and will therefore interact with other gluons. An example of the strong force in action is the binding nucleons within nuclei.

Not surprisingly, the weak force is the weakest of the three. Unlike the strong force and electromagnetism, the weak force is mediated by *massive* bosons: the electrically-charged W bosons ($80.4 \text{ GeV}/c^2$) and the electrically neutral Z bosons ($91.2 \text{ GeV}/c^2$). [1] This force affects all particles (all quarks and all leptons), regardless of electric or color charge. An example of the weak force in action is the decay of neutrons ($n \rightarrow p e \bar{\nu}_e$). In the Standard Model, the electromagnetic and the weak forces are considered different aspects of the same force (called the Electroweak force).

Unlike leptons, which are (more or less) readily found in nature, quarks are never found alone. This phenomenon, known as confinement [3], is described by Quantum Chromodynamics (QCD), the theory of strong interactions. QCD says that there are

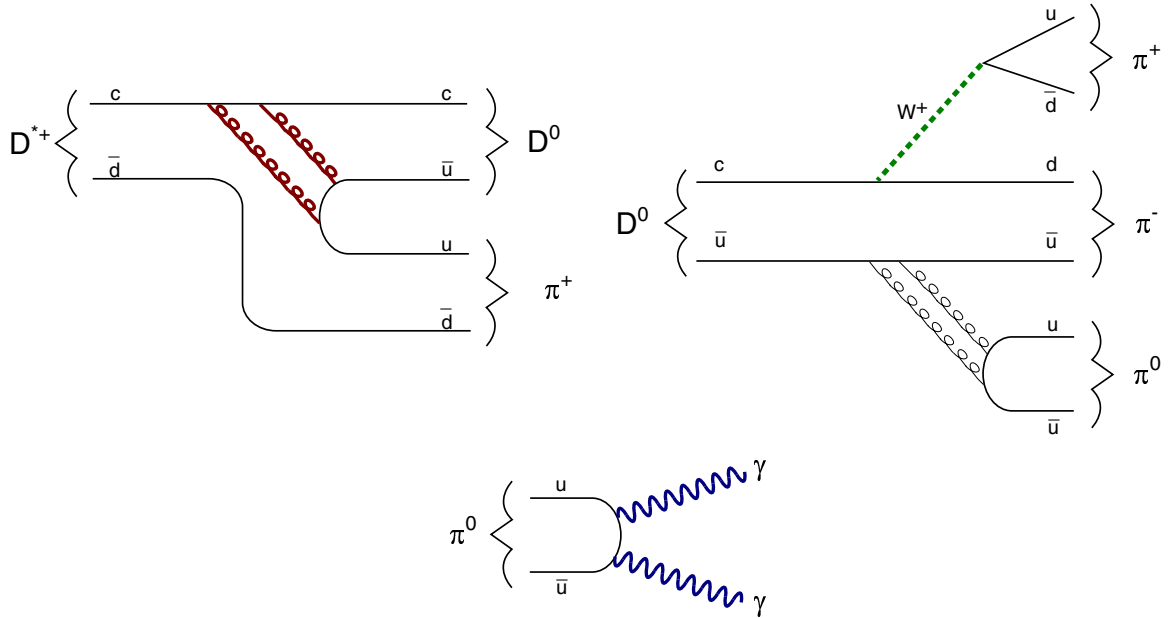


Figure 1.1: Possible Feynman diagrams for the decay chain $D^{*+} \rightarrow D^0\pi^+$, $D^0 \rightarrow \pi^-\pi^+\pi^0$, $\pi^0 \rightarrow \gamma\gamma$. The D^{*+} decays **strongly**, the π^0 decays **electromagnetically** and the D^0 decays **weakly**.

three distinct “color” charges often referred to as red, blue, and green³. Antiquarks⁴ have anti-color: anti-red, anti-blue, and anti-green (also known as cyan, yellow, and magenta respectively). According to QCD, only colorless objects can exist in nature. Three examples of this are mesons (a quark - antiquark group where the pair is a mixture of red - anti-red, blue - anti-blue, and green - anti-green⁵: $q_1\bar{q}_2$), baryons (three quarks where all three colors are present: $q_1q_2q_3$), and anti-baryons ($\overline{q_1q_2q_3}$)⁶. Hadron is the term that refers to any particle that interacts strongly (all baryons and mesons are hadrons, while leptons are not).

³Red, blue and green are almost always the colors used in the U.S. In other countries, they often use the colors of their flag (if there are three colors that are not white).

⁴Antiquarks are the antiparticles of the quark.

⁵More precisely, mesons are in a color singlet $\frac{1}{\sqrt{3}}(\text{red} - \overline{\text{red}} + \text{blue} - \overline{\text{blue}} + \text{green} - \overline{\text{green}})$.

⁶According to QCD, (anti-)baryons and mesons are not the only allowed combinations quarks and antiquarks. There has not been, however, any confirmed experimental evidence seeing any other states (e.g. $qqqqq$, $qqqq\bar{q}$, etc.).

If allowed, mesons will usually decay via the strong interaction (usually one quark emits one or more gluon which decays to another quark - antiquark pair; see the $D^{*+} \rightarrow D^0\pi^+$ decay in figure 1.1). If the quantum numbers or mass of the meson forbid it from decaying strongly, it may decay via the electromagnetic force (usually the quark and antiquark annihilate, producing at least 2 photons; see the $\pi^0 \rightarrow \gamma\gamma$ decay in figure 1.1). If it is unable to decay electromagnetically, it may decay weakly (see the $D^0 \rightarrow \pi^-\pi^+\pi^0$ decay in figure 1.1). Most of the particles discussed in this paper are not stable and will decay. There are, however, several particles (along with their respective anti-particles) that are believed to be stable: the electron, the lepton neutrinos, the proton, and the neutron⁷. All other baryons, mesons, and charged leptons are known to decay.

1.2 The CKM Matrix

The weak force is the only one that can change the flavor of quarks. A Weak decay usually changes quarks within a generation (e.g. $c \rightarrow W^+s$), but it can also change between generations (e.g. $c \rightarrow W^+d$). This all comes about because the mass eigenstates of the quarks are *not* the same as the weak force eigenstates.[3] Instead of

$$\begin{pmatrix} u \\ d \end{pmatrix}, \begin{pmatrix} c \\ s \end{pmatrix}, \begin{pmatrix} t \\ b \end{pmatrix}$$

as shown above for the mass eigenstates, the weak force pairs are

$$\begin{pmatrix} u \\ d' \end{pmatrix}, \begin{pmatrix} c \\ s' \end{pmatrix}, \begin{pmatrix} t \\ b' \end{pmatrix}$$

⁷Free neutrons (those not in nuclei) do decay with a half life of 15 minutes. Bound neutrons do not generally decay.

where the unitary matrix known as the Cabibbo-Kobayashi-Maskawa (CKM) matrix describes the change in basis:

$$\begin{pmatrix} d' \\ s' \\ b' \end{pmatrix} = \begin{pmatrix} V_{ud} & V_{us} & V_{ub} \\ V_{cd} & V_{cs} & V_{cb} \\ V_{td} & V_{ts} & V_{tb} \end{pmatrix} \begin{pmatrix} d \\ s \\ b \end{pmatrix} \quad (1.1)$$

If the CKM matrix were the identity matrix, the weak decay would not be able to change generations (e.g. the decay $c \rightarrow W^+s$ would be allowed, but the decay $c \rightarrow W^+d$ would not be). As it turns out, the CKM is measured to be close to the identity matrix, but with significant non-zero off-diagonal terms. The absolute values of the elements are:[1]

$$\begin{pmatrix} 0.9741 \text{ to } 0.9756 & 0.219 \text{ to } 0.226 & 0.0025 \text{ to } 0.0048 \\ 0.219 \text{ to } 0.226 & 0.9732 \text{ to } 0.9748 & 0.038 \text{ to } 0.044 \\ 0.004 \text{ to } 0.014 & 0.037 \text{ to } 0.044 & 0.9990 \text{ to } 0.9993 \end{pmatrix} \quad (1.2)$$

Since the diagonal elements are much bigger than the off-diagonal elements, weak decays that do not change generations are classified as ‘‘Cabibbo favored’’ decays (e.g. $D^0 \rightarrow K^- \pi^+ \pi^0$) while those decays which are generation-changing (e.g. $D^0 \rightarrow \pi^- \pi^+ \pi^0$) are less common and are said to be ‘‘Cabibbo suppressed.’’

1.3 CP Violation

CP violation refers to decays which violate the Charge-Parity symmetry. To talk about CP symmetry, it is instructive to first discuss charge and parity symmetries separately.

1.3.1 Parity Symmetry

Forces that respect parity are invariant under a reflection and inversion of spatial coordinates (i.e. the spatial vector $\vec{v} = (x, y, z)$ is transformed to $-\vec{v} = (-x, -y, -z)$). It is important to note that under parity, not all vectors change sign. All spatial vectors (e.g. position and momentum) do, while spin and angular momentum do not. This can be seen easily for angular momentum since it can be thought of as a cross product of two vectors ($\vec{L} = \vec{r} \times \vec{p}$). Under a parity transformation, $\vec{r} \Rightarrow -\vec{r}$, $\vec{p} \Rightarrow -\vec{p}$ and therefore $\vec{L} \Rightarrow -\vec{r} \times -\vec{p} = \vec{L}$. These vectors are called Pseudovectors. The strong and electromagnetic forces are two examples of such forces. It turns out, however, that the weak force does not respect parity.

The famous experiment which first showed parity violation in weak interactions was conducted in 1956 by C.S. Wu[3]. Wu and her coworkers carefully set up radioactive Cobalt 60 nuclei so that their nuclear spins were pointing up. When the Cobalt underwent beta decay ($n \rightarrow pe^- \bar{\nu}_e$), almost all of the electrons came out against the direction of the nuclear spin (in other words, the electron went in the $-\hat{z}$ direction). Under a parity transformation, the direction of the electron (a regular vector) would change sign, but the spin of the Cobalt would not. So the spin and the electron are aligned in one version but not in the other; the parity symmetry has been violated.

When dealing with massless particles (e.g. photons, neutrinos), the spins are either aligned with the direction of motion or against the direction of motion. If the spin and direction of motion are aligned, the particle is referred to as right-handed; if they are opposite, the particle is left-handed. Until Wu's experiment, it was widely believed[3] that half the neutrinos are right handed and half are left handed. What Wu showed, however, is that all neutrinos are left-handed and all antineutrinos are right-handed.

If we apply the parity operator, P , twice, we end up where we started. In other words, $P^2 = I$, the identity operator, and parity has eigenvalues of $+1$ and -1 .

Quantum Field Theory states[3] that hadrons are eigenstates of the parity operator and that the parity of a fermion (a particle with half-integer spin) has to be opposite to that of its anti-particle, while a boson (integer spin) has the same parity as its anti-particle. It is commonly taken that quarks have positive parity and anti-quarks have negative parity. The parity of a composite system is the product of the parities of the parts multiplied by a factor of $(-1)^l$ where l is the orbital angular momentum of the system. For example, $P | \pi^0 \rangle = - | \pi^0 \rangle$. The photon is a vector particle and has intrinsic parity -1.

1.3.2 Charge Conjugation Symmetry

Charge conjugation simply swaps anti-particles for their particles (and vice versa). As with the parity operator, applying the charge conjugation operator twice puts us back where we started. Unlike parity, however, most hadrons are not eigenstates of charge conjugation (e.g. $C | \pi^+ \rangle = | \pi^- \rangle$).

1.3.3 CP

The strong and electromagnetic forces both respect charge conjugation, while the weak force does not. Let's consider the decay $n \rightarrow pe^- \bar{\nu}_e$. As seen above, the $\bar{\nu}_e$ is always right-handed. If we applied charge conjugation to this decay, we'd get $\bar{n} \rightarrow \bar{p}e^+ \nu_e$ where the neutrino would still be right-handed (this decay is not allowed). Since only parity changes handedness, not charge conjugation, why not apply both operators. We would then end up with $\bar{n} \rightarrow \bar{p}e^+ \nu_e$ where the neutrino is left-handed (this decay is allowed). So maybe the weak decay respects the combination of charge and parity symmetries together.^{8?}

In a famous paper, Gell-Mann and Pais[4, 3] proposed that one should be able to

⁸Since the strong and electromagnetic decays respect parity and charge conjugation symmetries individually, they respect their combination as well.

see some very interesting behavior with neutral Kaon mesons. The K^0 is a meson made up of a s and a \bar{d} and its antiparticle, the \bar{K}^0 is a $d\bar{s}$ pair. Using a weak process, it is possible for the K^0 to turn into a \bar{K}^0 .

Both of the neutral kaons are pseudoscalars, so we have

$$P | K^0 \rangle = - | K^0 \rangle \text{ and } P | \bar{K}^0 \rangle = - | \bar{K}^0 \rangle.$$

According to the definition of the charge conjugation operator:

$$C | K^0 \rangle = | \bar{K}^0 \rangle \text{ and } C | \bar{K}^0 \rangle = | K^0 \rangle.$$

If we want to make eigenstates of CP, we can have

$$| K_\alpha^0 \rangle = \frac{| K^0 \rangle - | \bar{K}^0 \rangle}{\sqrt{2}} \text{ and } | K_\beta^0 \rangle = \frac{| K^0 \rangle + | \bar{K}^0 \rangle}{\sqrt{2}}$$

With these definitions, it follows that $CP | K_\alpha^0 \rangle = | K_\alpha^0 \rangle$ and $CP | K_\beta^0 \rangle = - | K_\beta^0 \rangle$.

K^0 and \bar{K}^0 decays to pions ($\pi^-\pi^+$ as well as $\pi^-\pi^+\pi^0$). Both final states have $C = +1$ and since pions have negative parity, the final state with two pions has $CP = +1$ and the final state with three pions has $CP = -1$. If CP is not violated, then we will always have $K_\alpha^0 \rightarrow \pi^-\pi^+$ and $K_\beta^0 \rightarrow \pi^-\pi^+\pi^0$.

Since the K_α^0 decays to two light pions, there is a lot of energy released in its decay which in turn means that there is a lot of phase space available for this decay to happen and it decays “quickly”. The K_β^0 , on the other hand, releases very little energy and therefore takes much longer to decay. In 1956, evidence for both of these particles had been found and the lifetime of K_α^0 was measured $8.9 \cdot 10^{-12}$ s where the lifetime of K_β^0 was $5.2 \cdot 10^{-8}$ s.[3]

If we were to make a beam of K^0 particles, we should see a lot of two pion decays (but very few three pion decays) near the source of the beam. As we get further and further away from the source of the beam, we should see more and more three pion decays (and fewer and fewer two pion decays). Cronin, Fitch, and collaborators did exactly such an experiment in 1964.[3, 5] After 17 m they found 45 two pion decays

out of over 22,000 total decays. This tiny (1 in 500) but very significant fraction was conclusive evidence that the Weak force violates the CP Symmetry.⁹

This was a very interesting and exciting time in physics history. Up until then, it was believed that there was symmetry in the way matter and anti-matter interacted. A symmetry that had been a core belief that many never questioned turned out not to be respected by nature. CP violation has since become one of the largest motivations for experimental searches in particle physics. It has even been suggested that CP violation is responsible for the excess of matter over anti-matter in our universe.[3, 9]

Until very recently, CP violation has only been seen in the neutral kaon system (Belle[6] and Babar[7, 8] have now recently reported seeing evidence for CP violation in the B mesons). One of the big motivations of our analysis is looking for the possibility of observing a difference between the decays $D^0 \rightarrow \pi^- \pi^+ \pi^0$ and $\overline{D}^0 \rightarrow \pi^+ \pi^- \pi^0$, which would provide the first evidence of CP violation in D mesons.

1.3.4 The CKM Matrix, Revisited

As shown in Equation 1.1, the CKM matrix represents the change from the mass eigenstates to the weak eigenstates. In Equation 1.2, I gave the approximate magnitudes of all 9 elements. However, the elements do not have to be real, and in order to explain CP violation¹⁰ at least some of the elements must be complex. The common way of parameterizing the complex CKM matrix is: [1]

$$\begin{pmatrix} 1 - \lambda^2/2 & \lambda & A\lambda^3(\rho - i\eta) \\ -\lambda & 1 - \lambda^2/2 & A\lambda^2 \\ A\lambda^3(1 - \rho - i\eta) & -A\lambda^2 & 1 \end{pmatrix} + \mathcal{O}(\lambda^4) \quad (1.3)$$

⁹The CP eigenstates K_α^0 and K_β^0 are not the same as the particles K_S^0 and K_L^0 . In terms of these CP eigenstates, $|K_S^0\rangle = |K_\alpha^0\rangle + \epsilon |k_\beta^0\rangle$ and $|K_L^0\rangle = |K_\beta^0\rangle - \epsilon |k_\alpha^0\rangle$ where $|\epsilon| \ll 1$.

¹⁰At the time that CP violation was discovered, the charm quark had not yet been discovered and nobody was even theorizing about the third generation of quarks. Kobayashi and Maskawa realized that when you have a 2×2 matrix (for the two generations), it was always possible to make it real. So if CP violation exists, there must be a third generation of quarks.[10, 3]

where A , ρ , and η are real numbers of order unity and λ is a real number $\ll 1$. The imaginary part of the CKM matrix is not large, but very, very important.

1.4 A Brief Review of Relativistic Mechanics

In non-relativistic mechanics, momentum is a three-vector $\vec{p} = (p_x, p_y, p_z)$. In relativistic mechanics, the energy of the particle is also included in the four-momentum vector: $p^\nu = (E/c, p_x, p_y, p_z)$ where $E^2 = m^2c^4 + p^2c^2$. One of the reasons that this is so useful is that the scalar product of two four-vectors of momentum is invariant regardless of the reference frame in which the momentum is measured. In particular, the scalar product of a momentum with itself: $p^\nu p_\nu = \frac{E^2}{c^2} - p_x^2 - p_y^2 - p_z^2 = m^2c^2$.

Consider an example of $\rho^0 \rightarrow \pi^-\pi^+$. By conservation of momentum we have $p_\rho^\nu = p_{\pi^-}^\nu + p_{\pi^+}^\nu$. If we have detected two pions and want to know if they came from a ρ^0 , one way to establish this as a possibility is to check the invariant mass (or invariant mass squared) of the pair of particles. In other words, does $(p_{\pi^-} + p_{\pi^+})^\nu (p_{\pi^-} + p_{\pi^+})_\nu$ equal $m_{\rho^0}^2$? This type of invariant mass calculation is frequently used throughout the analysis in this thesis.

1.5 An Event at CLEO

In the analysis that will be presented, we are looking at the following decay: $D^0 \rightarrow \pi^-\pi^+\pi^0$. Let's look at a typical event that contains our decay. The first thing to note is that during the time scales that we are interested in (a few nanoseconds), there are five particles (and their anti-particles) that are considered "stable": the light leptons (electrons and muons), two mesons (kaons and pions), protons and photons. As we will see, we only use pions and photons in this analysis. All other particles decay before we ever get a chance to "see" them. To get a clearer picture of this, let's follow an example decay.

At CESR, the electron and positron often annihilate through the electromagnetic force and form a $q\bar{q}$ pair (Figure 1.2).

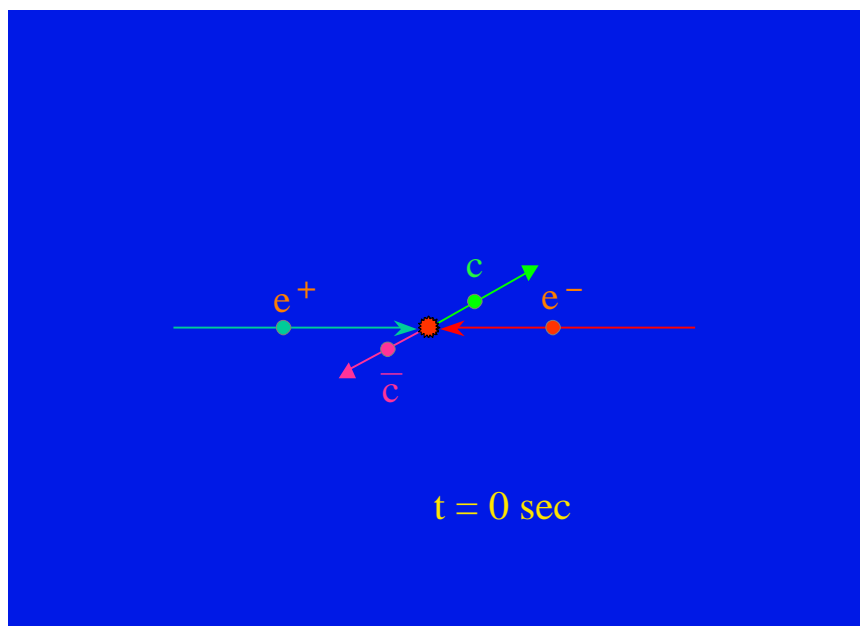


Figure 1.2: $e^+e^- \rightarrow c\bar{c}$.

As the $c\bar{c}$ quarks move apart from each other, more and more energy is stored in the attraction between the quarks. After an amount of time on the order of 10^{-23} seconds, it becomes favorable to use the energy stored in the attraction to form one or more additional $q\bar{q}$ pairs. This is known as hadronization. (Figure 1.3).

At an approximate time of 10^{-20} seconds, mesons that can decay strongly do so. (Figure 1.4).

Electromagnetic decays are next after approximately 10^{-16} seconds.

Finally, particles that are going to decay weakly start to do so after 10^{-12} seconds. (Figure 1.5).

After $t \approx 10^{-9}$ seconds, the particles start making it to the CLEO detector. (Figure 1.6) Many of the particles that we want to study, the D^0 for example, have long since decayed.

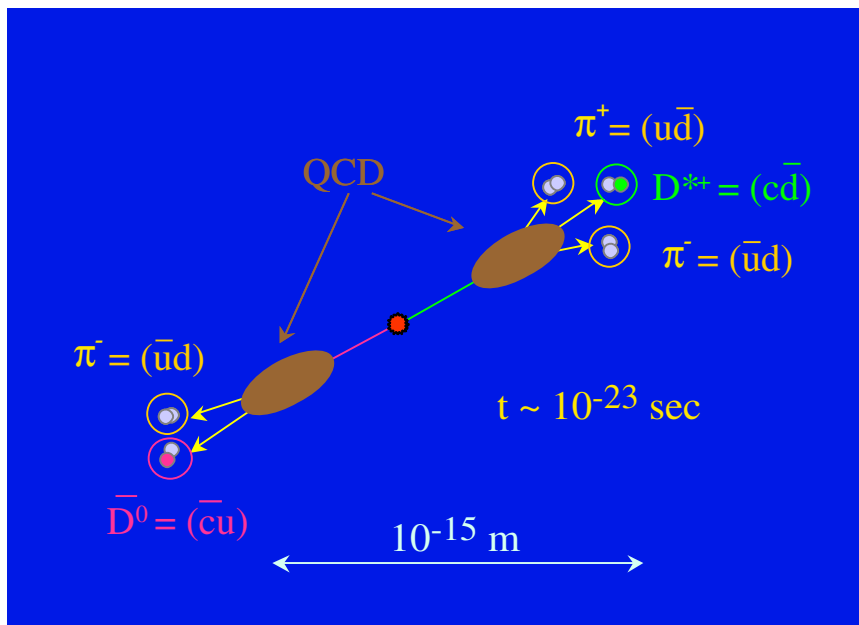


Figure 1.3: After a very short period of time, hadronization occurs. In this case, one $u\bar{u}$ and two $d\bar{d}$ pairs were formed. These quarks and the original $c\bar{c}$ pair form a π^- and a \bar{D}^0 on one side and a D^{*+} and two charged pions on the other.

1.6 Finding $D^0 \rightarrow \pi^- \pi^+ \pi^0$ Events

Now that we have seen how a $D^0 \rightarrow \pi^- \pi^+ \pi^0$ event happens in CLEO, let's examine how we search for them. We are looking for the following decay chain (red particles are directly observed):

$$D^0 \rightarrow \pi^- \pi^+ \pi^0$$

$\searrow \gamma \gamma$

Suppose every event has exactly one of these decays and nothing else. We first find the π^0 by reconstructing the γ daughters of the π^0 . Next, we can calculate the Lorentz-invariant mass of the $\pi\pi\pi$ triplet. If we plot the invariant mass for a large number of such events in a histogram, we get a distribution about the D^0 mass. The width of this distribution is convolution of the D^0 width (Γ_{D^0}) with the detector resolution (σ_{detector}). In this case, since $\sigma_{\text{detector}} \gg \Gamma_{D^0}$, the width of the

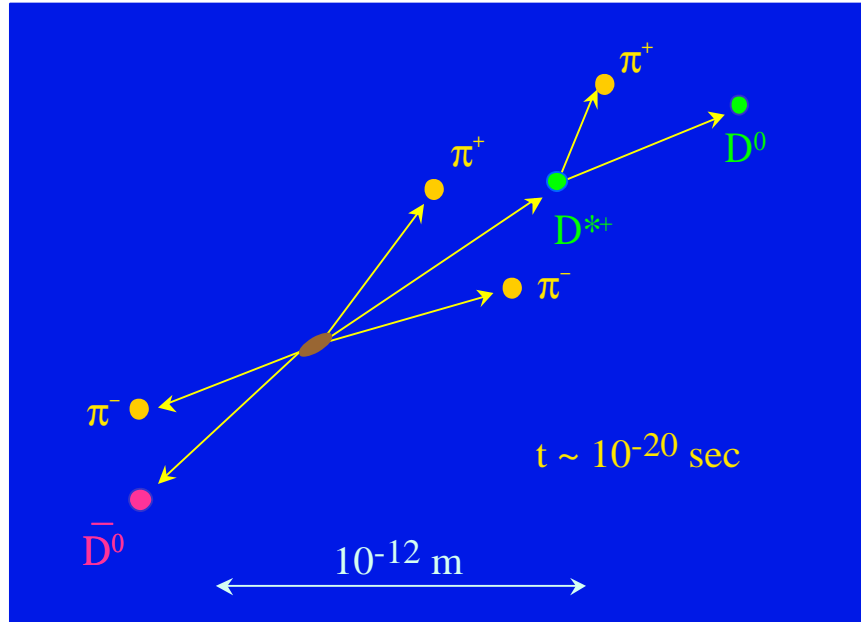


Figure 1.4: At $t \approx 10^{-20}$ seconds, we have strong decays. In this case, the $D^{*+} \rightarrow D^0 \pi^+$.

mass distribution can be considered uniquely a result of the detector resolution itself. See Figure 1.7.

Realistically, however, signal events are going to have many tracks that are not part of the decay. There is no way to be certain which belong to the D^0 . For every signal event, we will have one right and many wrong combinations. See Figure 1.8.

Unfortunately, most events do not have the decay we are looking for, which means we have even more background. See Figure 1.9.

Luckily, looking at certain characteristics of the event (“making event selection cuts”), we can greatly reduce the size of the background without a big loss to the signal (see Figure 1.10).

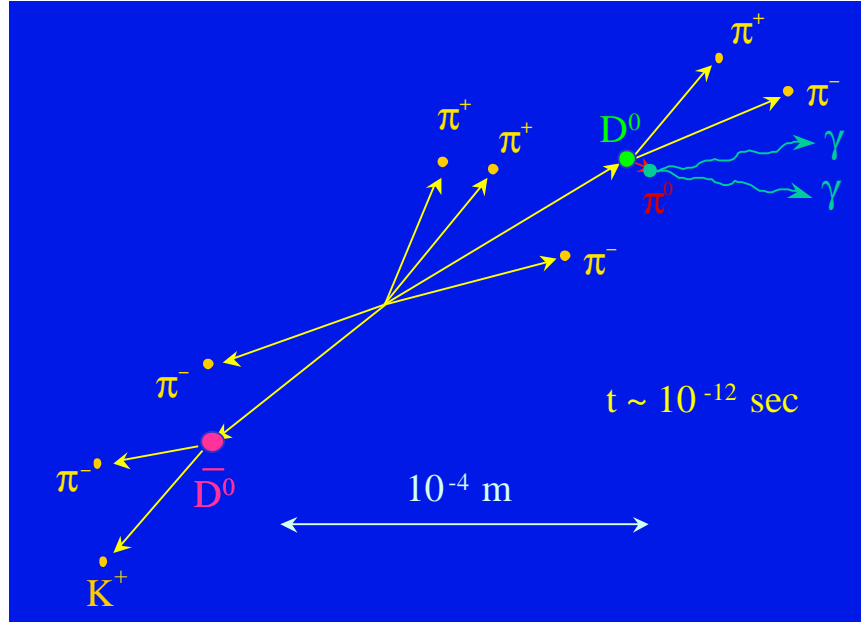


Figure 1.5: After approximately 10^{-12} seconds, weak decays start. In our case, the $\bar{D}^0 \rightarrow K^+\pi^-$ and $D^0 \rightarrow \pi^-\pi^+\pi^0$. On the weak time scale, the π^0 decays almost immediately (since it decays electromagnetically) into two photons.

1.7 A Quick Word About Units

1.7.1 Electron-Volts

Particle physicists are unique in the units that they use. Their favorite unit of energy is the electron-volt (eV), which is defined as the energy that an electron gains when accelerated in a 1 V potential difference ($= 1.602 \cdot 10^{-19}\text{ J}$).

It is possible to use the electron-volt to measure momentum and mass as well. $1 \frac{eV}{c} = 5.344 \cdot 10^{-28} \frac{kg \cdot m}{s}$ for momentum and $1 \frac{eV}{c^2} = 1.782 \cdot 10^{-36}\text{ kg}$ for mass (In these units, the electron has a mass of $511\text{ keV}/c^2$ and the proton's mass is $938\text{ MeV}/c^2$). It's not too hard to see that these units work much better on our scale than joules, $\frac{kg \cdot m}{s}$, and kilograms.

A common practice in particle physics is to pick units so that the speed of light is equal to 1. In this case, the electron-volt is now a unit for energy, momentum, and

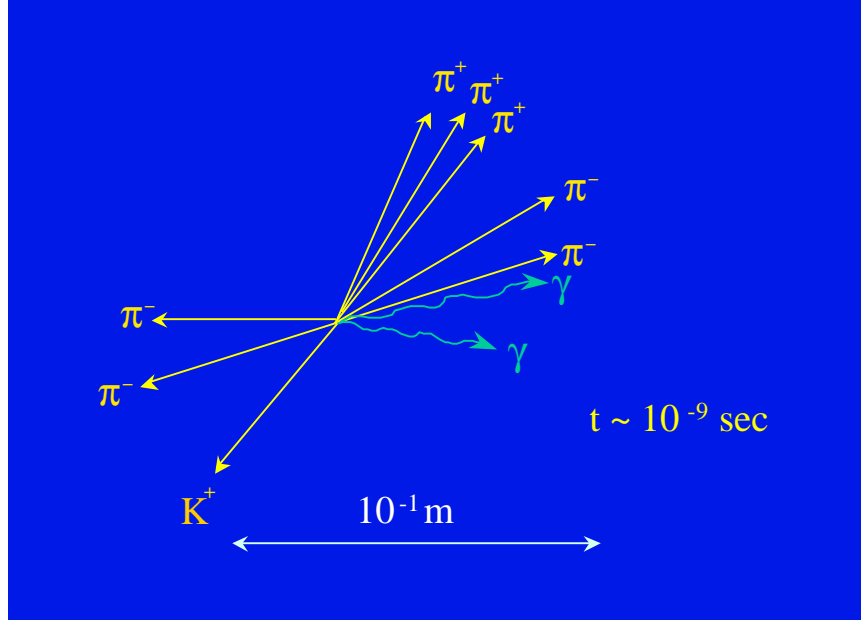


Figure 1.6: Particles have finally travelled far enough after about 10^{-9} seconds to be observed by the CLEO detector.

mass.

1.7.2 Luminosity and Cross Sections

When looking for a particular decay at a collider, it is common to calculate the total number of expected events that contain said decay:

$$\mathcal{N}_{events} = \mathcal{L}_{int} \cdot \sigma \quad (1.4)$$

where \mathcal{N}_{events} is the expected number of events, \mathcal{L}_{int} (integrated luminosity) is a measurement of how many particle collisions we have had and σ (Cross Section) is an area¹¹ corresponding to the likelihood of having the specific decay. Since the number of events is unitless, integrated luminosity must have units of inverse area. Since we are dealing with small particles, cm^2 is generally considered much too big to

¹¹That cross sections are thought of as area extends from the idea of classical collisions and targets.

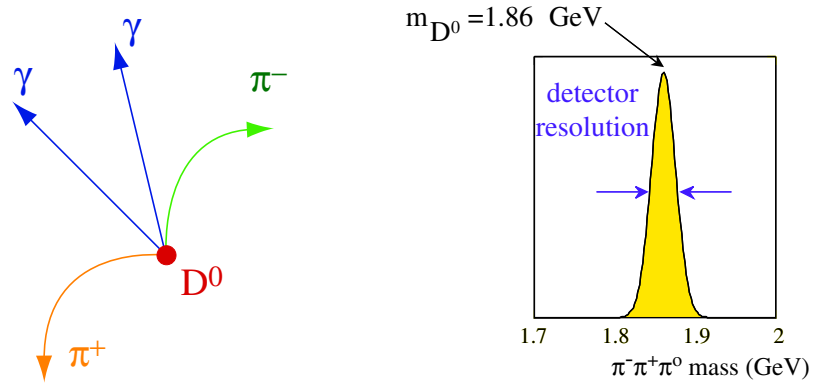


Figure 1.7: A D^0 mass distribution assuming there is nothing in the events except the particles we are looking for. The width of the distribution is a measure of detector resolution since the intrinsic width of the D^0 is so small.

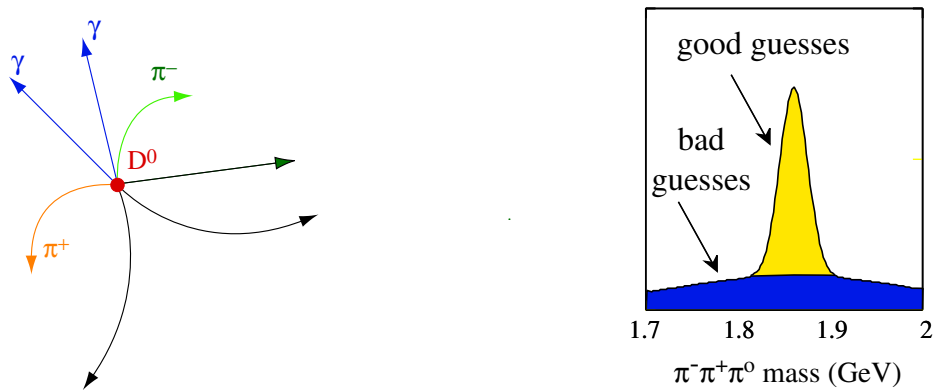


Figure 1.8: A D^0 mass distribution assuming every event has the decay chain we are looking and that other charged and neutral particles are also present.

be useful. Instead, particle physicists start off with the barn ($1 b = 10^{-24} \text{ cm}^2$). Even these diminutive units are frequently too large and are often found as nanobarns (nb), picobarns (pb), and even femtobarns (fb). Corresponding, integrated luminosities are often measured in inverse nanobarns (nb^{-1}), inverse picobarns (pb^{-1}) and inverse femtobarns (fb^{-1}). It is worth explicitly mentioning that inverse femtobarns are a thousand times bigger than inverse picobarns which are in turn a thousand times bigger than inverse nanobarns.

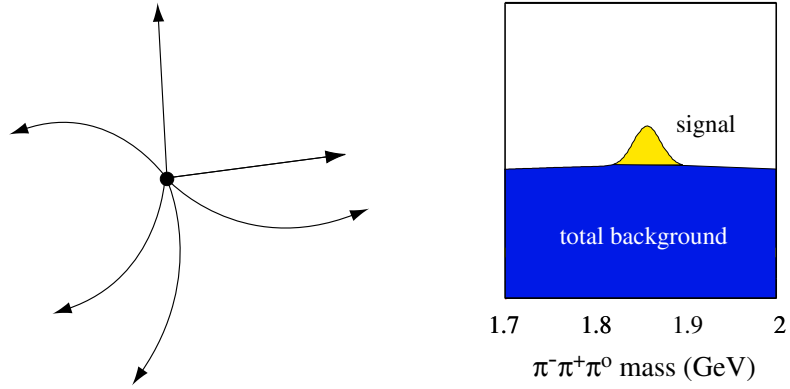


Figure 1.9: A D^0 mass distribution assuming some events have the decay chain we are looking for, but most do not.

Let's look at an example relevant to CLEO. The cross section for $e^+e^- \rightarrow c\bar{c}$, is approximately 1 nb . CLEO integrated 9 fb^{-1} . This means that we have $\mathcal{N}_{c\bar{c}} = \sigma_{e^+e^- \rightarrow c\bar{c}} \cdot \mathcal{L}_{int} = 9 \cdot 10^6$. In other words, CLEO II.V collected almost 10 million $c\bar{c}$ events.

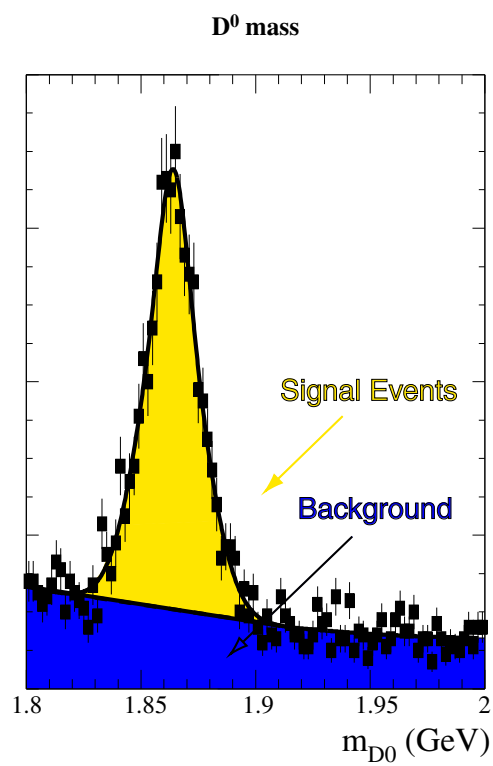


Figure 1.10: The distribution of D^0 mass in data using event selection criteria. The number of signal and background events can be determined by fitting this distribution to a background piece and a signal piece. See Section 3.7 for a more complete discussion about counting signal and background events.

Chapter 2

Cæsar and Cleopatra

This chapter is about the Cornell Electron Storage Ring (CESR) and the CLEO II.V Detector, both of which are located on the Cornell University campus in Ithaca, New York. CESR is the source of accelerated electrons and positrons and CLEO¹ is the detector we use to study the collisions.

2.1 CESR

CESR is a 242 *m* diameter ring located 10 *m* below Cornell's Alumni Fields that has simultaneous electron and positron currents circulating in opposite directions. The particles are travelling just below the speed of light and make almost 400,000 revolutions per second. For almost the entire history of CLEO II.V, CESR has been operating with a center of mass energy at or just below the mass of the $\Upsilon(4s)$ ($10.58 \text{ GeV}/c^2$) with an energy of 5.29 *GeV* per beam.

The manner in which the electrons and positrons end up in the storage ring is very interesting and deserves a closer look. Electrons and positrons traverse similar paths. The path of the electrons will be described first, followed by a description of

¹For those of you who are wondering, CLEO does not stand for anything. The storage ring was named CESR (pronounced Cæsar) and it seemed natural to want to name the detector after Cleopatra. The original plan was to go back and decide for what CLEO was an acronym, but it never happened.

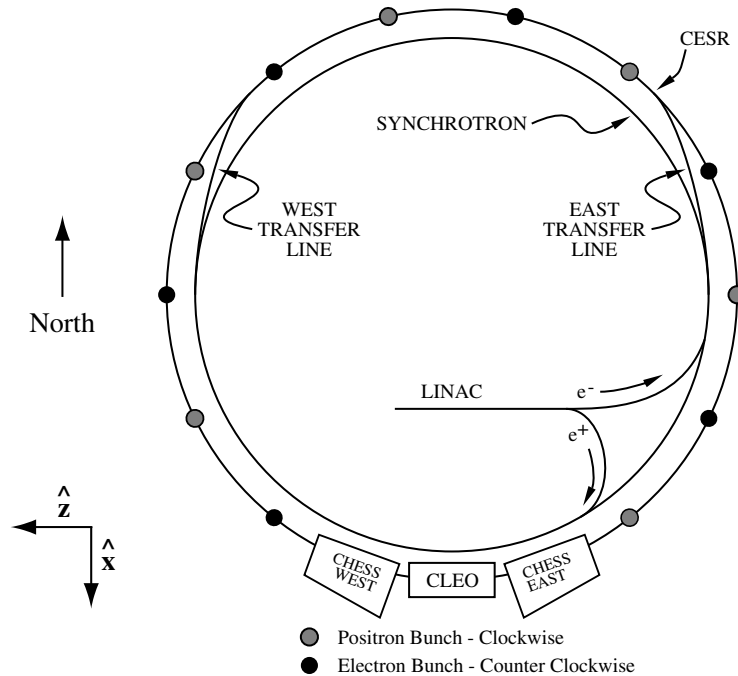


Figure 2.1: A layout of CESR. Note that “up” is North, \hat{x} is South and \hat{z} is West.

the differences for the positrons.

The first thing needed is a source of electrons. This is accomplished by heating a filament (this is very similar to the cathode ray tube found in monitors and televisions) and applying a voltage differential to separate electrons from the filament. The electrons are then accelerated to an energy of 300 MeV in a 30 m Linear Accelerator (LINAC) using varying electric fields generated by radio frequency cavities.

At the end of the LINAC, the electrons are injected into the synchrotron. The synchrotron is a ring a few meters smaller in diameter than CESR. The electrons are accelerated to their final energies in about 7000 revolutions (approximately 18 ms). After reaching their final energy, the electrons are transferred into CESR (see Figure 2.1).

There is, unfortunately, no such easily available source for positrons. To make positrons, a tungsten target is inserted half-way down the LINAC (at 15 m). At this

point, the electrons have approximately 150 MeV of energy and the collision produces many particles including positrons². The positrons are captured and steered using magnets, and are then accelerated to 150 MeV in the remaining 15 m of the LINAC. They are then injected into the synchrotron, accelerated up to their final energy, and moved into CESR.

Because of the nature of the CESR accelerating RF cavities, the electrons and positrons do not travel in a continuous ribbon, but rather in bunches. At the end of CLEO II.V operations, CESR was running with nine groups (called trains) of electrons and positrons with each group having three distinct bunches (called cars).

When CESR first started to operate, it was run with only one bunch of electrons and one bunch of positrons. The beams were injected into CESR in such a way that they only collided in the north and south interaction regions.³ In order to increase the luminosity, it was decided that running with more than one bunch was necessary. Unfortunately, with the electrons and positrons travelling in circles, this would lead to collisions in several other places around the ring. In order to assure that the beams collide only in the south interaction region, both beams are forced to follow a “pretzel”-shaped orbit (see Figure 2.2) which insures that collisions will only happen in one place around the ring.

2.2 CLEO II.V

The CLEO II.V detector is an upgrade [13] to the CLEO II detector⁴, which has been well described in the literature[11]. In this section, I will discuss the CLEO II.V detector briefly.

² Electrons, X-rays, and protons are also very common byproducts of this collision.

³When CESR was first commissioned, there were two simultaneous experiments: CLEO at the southern interaction region and CUSB (Columbia University and State University New York at Stony Brook) at the north. CUSB was later taken out.

⁴The inner-most straw tracker was replaced by a precision silicon tracker and the argon-ethane gas in the drift chambers was replaced with a helium-propane mixture.

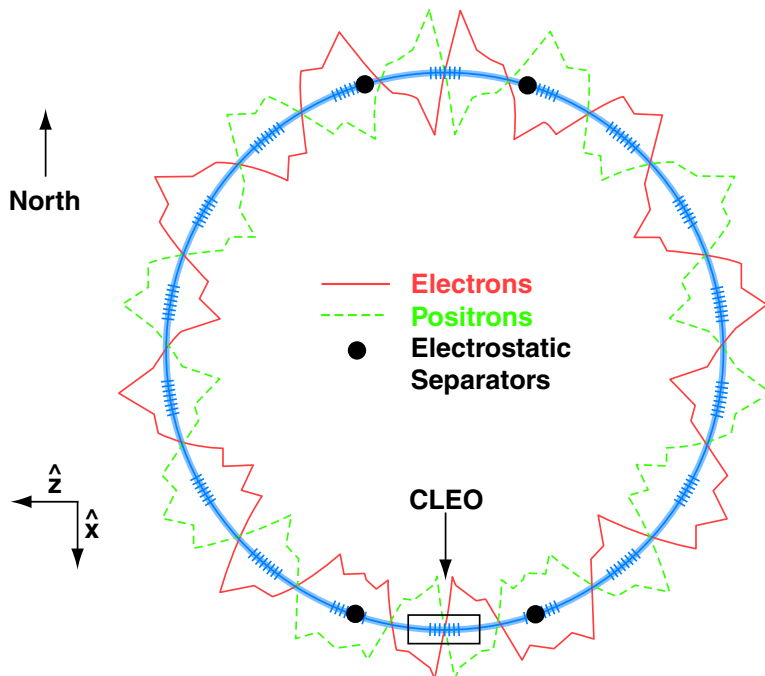


Figure 2.2: A diagram of CESR pretzel orbit. The extent to which the orbit deviates from circular is greatly exaggerated for illustration purposes.

CLEO II.V is a cylindrical detector that has almost complete 4π solid angle coverage ($> 95\%$). The beams collide in a vacuum inside of the 1 mm thick beryllium beam pipe. Surrounding on the 1.875 cm radius beam-pipe there is a three-layer silicon vertex detector. Moving outward are the drift chambers (the vertex detector and the main drift chamber). Together these three detectors are used to reconstruct the path of charged particles. A time-of-flight detector, located outside the main drift chamber, is used both for triggering⁵ and for particle identification. The crystal calorimeter is used for detecting photons as well as charged particles. All of these detector components are located within a 1.5 tesla superconducting solenoid. Muon chambers, used for differentiating muons from other charged particles, are mounted outside the solenoid. See Figure 2.3 for a view of CLEO.

⁵The trigger is the part of the CLEO that decides when to read out the detector. See Section 2.2.7 for a complete discussion.

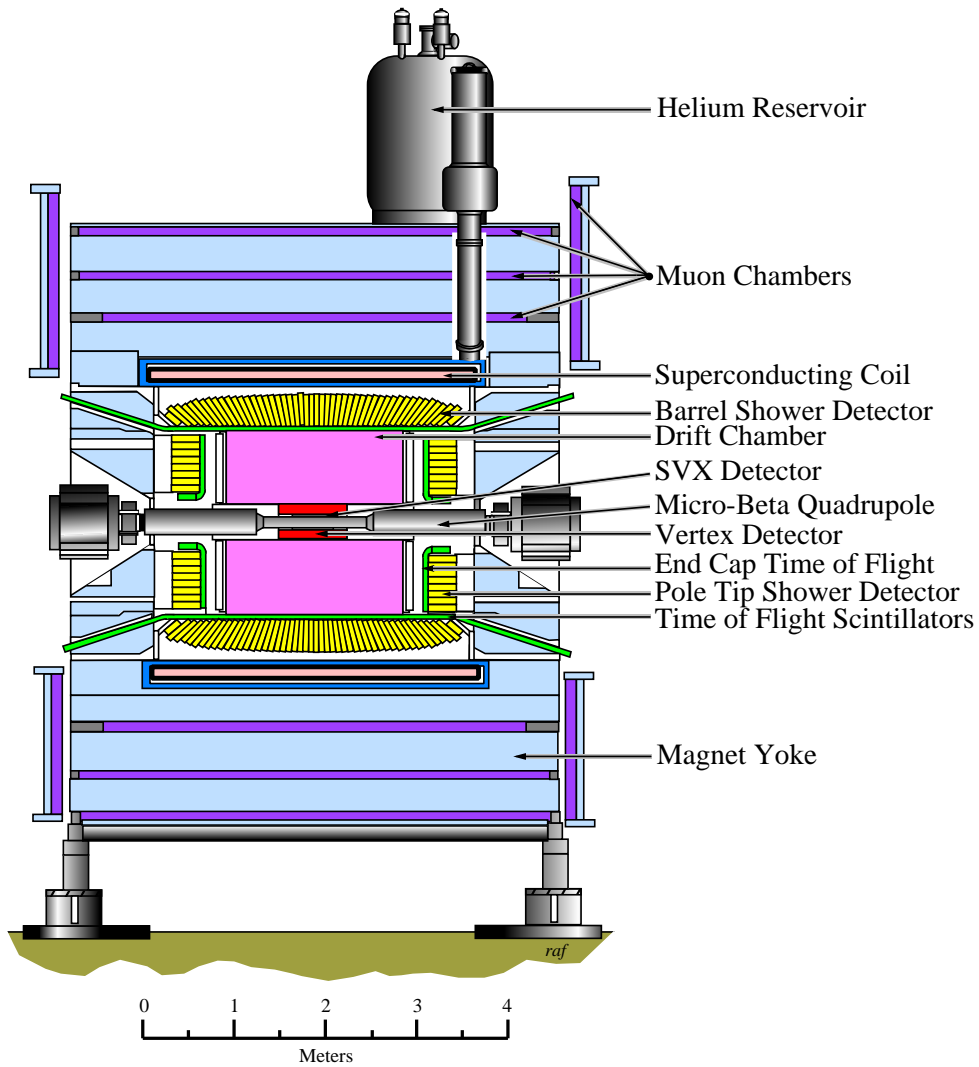


Figure 2.3: A picture of CLEO.

Before continuing, let's define our coordinate system. We choose \hat{z} to be the direction of motion of the positrons (due West). \hat{x} is pointing South (out of the ring) and \hat{y} is up. ϕ is an angle measured in the x - y plane ($\phi = 0$ is in the \hat{x} direction). θ is measured with respect to the z axis.

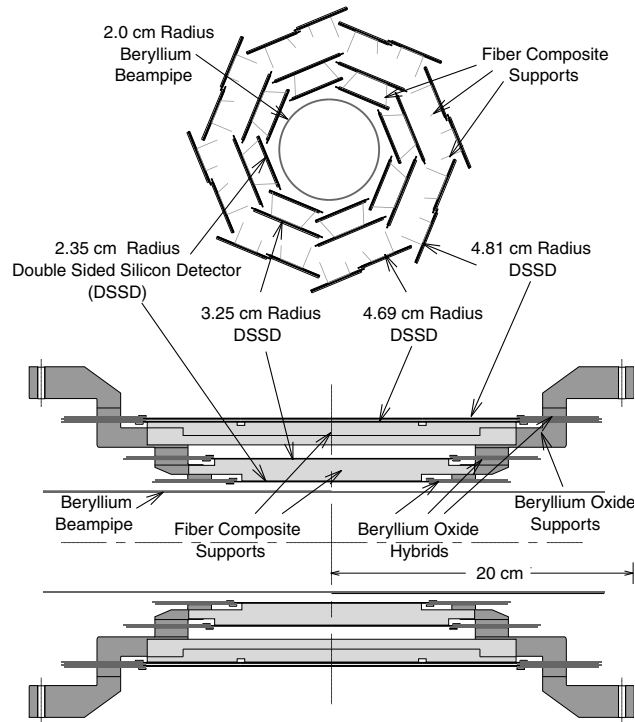


Figure 2.4: A view of the CLEO II.V Silicon Vertex Detector.

2.2.1 The Silicon Vertex Detector

The Silicon Vertex Detector (SVX) is a microstrip detector that has an inner radius of 2.25 cm and an outer radius of 4.7 cm . It is a three-layer device made of 96 wafers. Each wafer has two sides: the inner side gives precision z measurement; the outer gives a precision $r - \phi$ measurement. Resolutions on the z side are on the order of $100\ \mu\text{m}$ while the $r - \phi$ side has a resolution of about half that. The entire detector has more than 26,000 channels. See Figure 2.4 for a diagram of the silicon detector.

2.2.2 Drift Chambers

The drift chambers (the Vertex Detector and the main Drift Chamber) are both based on the same principle: When a charged particle travels through certain gases (a 60% – 40% Helium Propane mixture in our case), it ionizes the gas. With nearby wires⁶ providing a carefully controlled electric field, the electrons drift to the wires and deposit a charge. We get both drift distance information (i.e. how close the track passed to the wire) and charge deposition⁷ information from the sense wires.

Because these two chambers are in a constant magnetic field (see the Superconducting Magnet below), we can make transverse momentum measurements⁸.

The tracking resolution of the drift chambers is described by Equation 2.1 below:

$$\left(\frac{\delta p_t}{p_t}\right)^2 = (0.0011 \cdot p_t/1 \text{ GeV})^2 + (0.0067)^2 \quad (2.1)$$

where p_t is transverse momentum (momentum perpendicular to the magnetic field). A 5.3 GeV muon has a resolution of 47 MeV where a muon with transverse momentum of 200 MeV would have an uncertainty of less than 1.5 MeV.

The Vertex Detector consists of 10 layers of axial⁹ sense wires; the inner five layers have 64 sense wires per layer while the outer five have 96 (for a total of 800 sense wires). At the inner and outer radii, 6 mm cathode pads are placed that give us z information as to when the charged particle enters and leaves the chamber. See Figure 2.5 for the position of the VD.

The Main Drift Chamber has 40 axial and 11 stereo¹⁰ layers. The number of sense

⁶As shown in Figure 2.5, for every “sense” wire (i.e. the wires with the positive voltage), there are several “field” wires (at zero volts) to shape the electric field.

⁷The amount of charge deposited on a sense wire helps us determine what type of particle made the track. See Section 2.3.

⁸Recall that a charged particle with charge q momentum p moving perpendicular to a magnetic field B travels in a circle of radius $= \frac{p}{qB}$. Therefore, in determining the radius of curvature of a charged particle, we can calculate its transverse (perpendicular to the beam pipe and magnetic field) momentum.

⁹Axial means that the wires are parallel to the beam pipe.

¹⁰Stereo layers deviate very slightly from being perfectly parallel (from 3.5° to 7°) to the beam pipe.

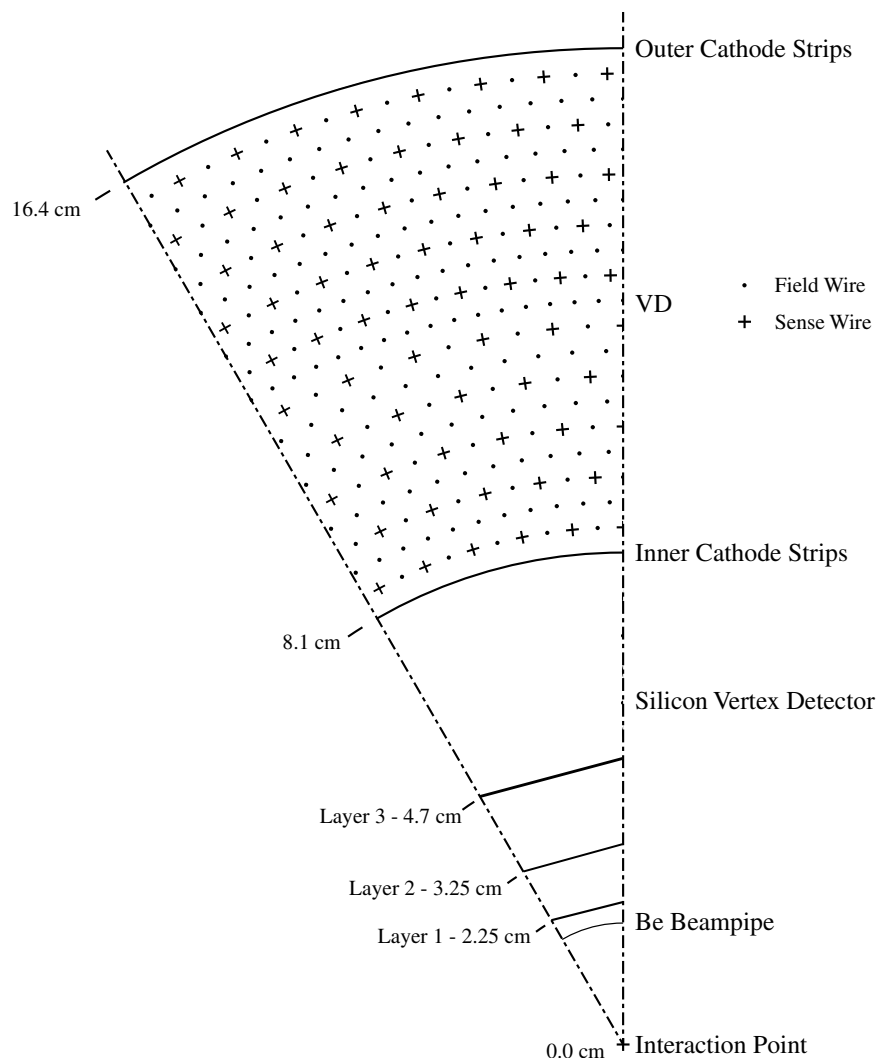


Figure 2.5: A diagram showing the relative positions of the Beam Pipe, Silicon Vertex Detector and the Vertex Detector.

wires per layer varies from 96 wires to 384 wires with a total of over 12,000 sense wires in the whole chamber. As in the Vertex Detector, there are inner and outer cathode pads (1 *cm* wide instead of 6 *mm* as in the VD) to give z information as to where particles enter and leave the chamber. See Figure 2.6 for the layout of the Drift Chamber.

When tracks are completely reconstructed, the tilt of the wires leads to additional z information.

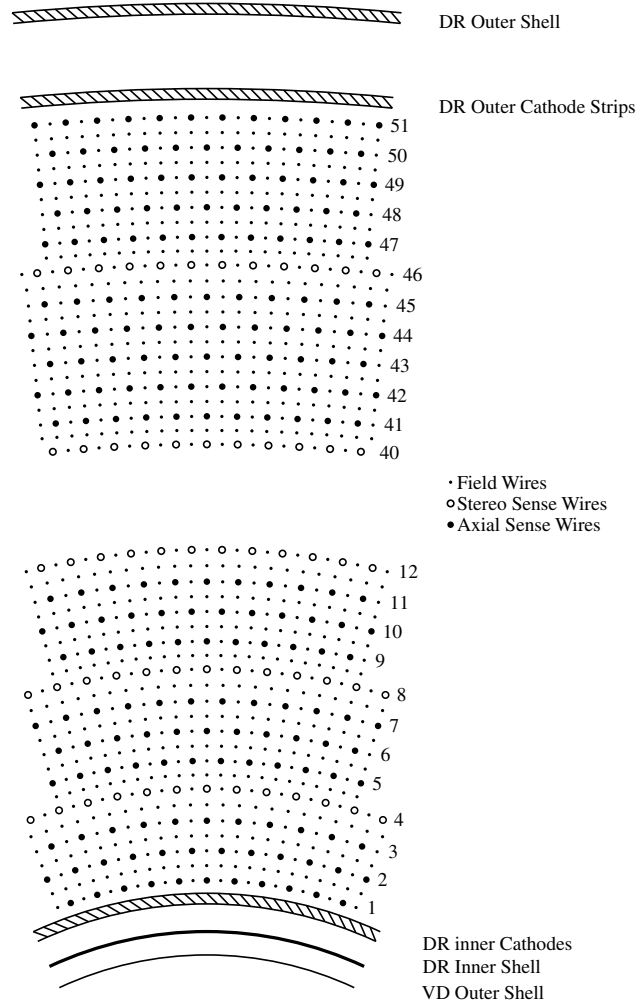


Figure 2.6: A diagram of the Main Drift Chamber.

2.2.3 Time of Flight

The Time of Flight (TOF) detector is made of plastic scintillator bars. Its purpose is to give us very accurate information about the time when tracks pass through it. This information is used both in the trigger (see Section 2.2.7) and for particle identification (see Section 2.3). All of the detectors inside the TOF are arranged cylindrically around the beam pipe. The Time of Flight is arranged in two separate

components. The barrel TOF which is arranged cylindrically around the beam pipe covers about 80% of the solid angle. The Endcap TOF is arranged perpendicularly to the beam pipe and covers approximately 10% of the solid angle. See Figure 2.3 for a view of the position of the TOF in CLEO.

2.2.4 Crystal Calorimeter

Since the installation of the Crystal Calorimeter (CC), CLEO's ability to detect photons has been one of its greatest strengths. The CC is made up of 7,800 thallium-doped cesium-iodide crystals, each 5 *cm* square by 30 *cm* in length and read out with photodiodes. The barrel CC consists of 6,144 crystals and covers 71% of the solid angle. Each endcap has 828 crystals and covers an additional 11% of the solid angle (the total solid angle coverage is 93%).

In the barrel, the energy resolution is better than 1.5% for a 5 *GeV* shower and just under 4% for a 100 *MeV* deposit of energy. The numbers are slightly worse but comparable for the endcap (2.6% for a 5 *GeV* photon and 5% for a 100 *MeV* shower). The angular resolution is equally impressive: usually less than 10 *mrad* in the barrel CC and 20 *mrad* in the endcap.

2.2.5 Superconducting Magnet

All of the detectors mentioned up to this point are inside the Superconducting Magnet. This magnet produces a 1.5 *T* magnetic field in the \hat{z} direction. The magnetic field is uniform to better than 0.1% over a cylindrical volume with a radius of 1 *m* and length of 2 *m*[11]. The magnetic field allows us to not only differentiate between positively and negatively charged particles, but also provides precision momentum measurements as described above.

2.2.6 Muon Detector

The muon detector is similar to the Vertex Detector and Drift Chamber, except that it is embedded between layers of iron located outside of the magnet. It was designed to be efficient while having a low occurrence of hadrons faking muons. The barrel Muon Detector consists of 3 detectors that are located after 36, 72, and 108 *cm* of iron. The total equivalent thickness of iron varies from 7 to 10 nuclear absorption lengths ($\lambda = 16.8 \text{ cm}$) depending on the direction of the charged particle. [11] Our current analysis does not use any of the information provided by the muon detector.

2.2.7 Data Acquisition and Trigger

At the end of the CLEO II.V era, the Data Acquisition system (DAQ) was capable of reading out events at rates up to 50 *hz*. It was the job of the trigger to decide which events should be read out while keeping the data rate from getting too big. The trigger had three hardware components (Level 0, Level 1, and Level 2) and one software component (Level 3). In order to be written out to tape, an event had to successfully pass all 4 levels.

Just after every crossing, the Level 0 trigger looked at data from the time of flight detectors, the vertex detector, and the crystal calorimeter. When the Level 0 trigger determined that nothing of interest happened, there was no dead time associated with its decision. If, however, the event passes the Level 0 criteria, the trigger suppresses the gates of the entire detector while the Level 1 trigger looks at the event. This causes a deadtime of 2.2 μs while the Level 1 trigger looks at the main drift chamber and the calorimeter.

If the event does not exceed the Level 1 criteria, the detector is reset to start looking at data again and no further loss is incurred. Events that do pass Level 1 are sent to the Level 2 trigger and cause an additional deadtime of 40 μs . Level 2 uses information from the calorimeter and both drift chambers to decide if the event is of

interest. If the event does not pass, the detector is reset to resume data collection with no further dead time. If the event passes Level 2, the event is read out, taking over 2 *ms* to move the data from the data boards to the CPUs in their respective crates. After this time, the detector is again reset and data collection continues.

Even though the detector can be reset, the event is not finished. It takes 16 *ms* to sparsify the data¹¹ and get the data into the Level 3 software trigger. The Level 3 trigger looks at all of the detectors to weed out noise events (e.g. events where electrons from one beam interact with gas in the beampipe). The events passing Level 3 are written to tape.

2.3 Particle Identification

Of the five stable charged particles detected at CLEO, two of them (electrons and muons) are fairly easy to distinguish from the rest. Since muons interact very weakly with matter, one can get a fairly pure sample of muons by insisting that the particles leave tracks in the muon chambers which are behind many interaction lengths of steel. Electrons are not quite as clean, but by using calorimeter information, we have relatively good success at getting a pure sample. Electrons leave almost all of their energy in the calorimeter while the other four stable particles leave a smaller fraction. By looking at the ratio E/p where E is the energy left in the calorimeter and p is the magnitude of the measured momentum, electrons can be identified.

Separating kaons, pions, and protons, however, is a much more difficult task. CLEO II.V had, however, two tools to help the situation. The first was examining the total charge left on sense wires in the drift chambers. The second was using the time of flight system.

When travelling through gas, charged particles ionize the gas which causes them

¹¹When reading out a detector, it is almost always the case that there is useful information from only a subset of the channels. Sparsification is the process of keeping only the information that is needed in order to reduce the size of the data being read out.

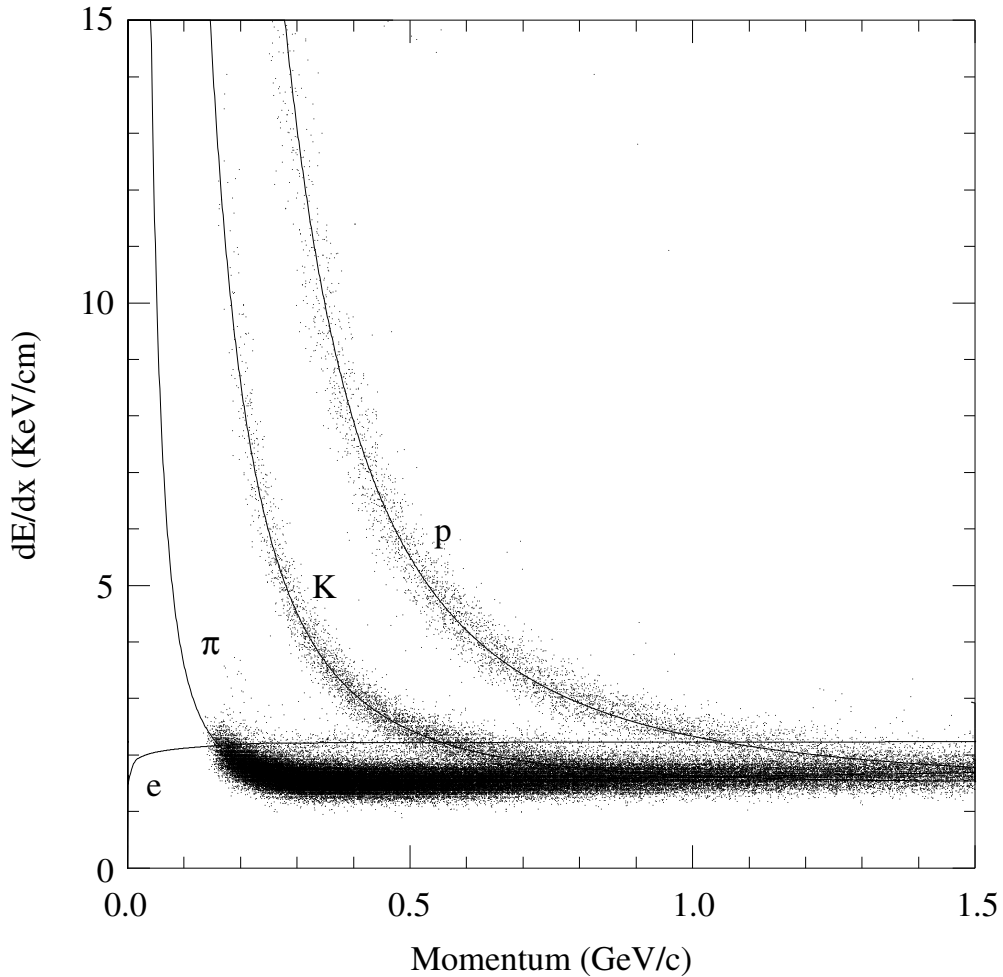


Figure 2.7: Energy loss per unit length of travel. The solid lines are averages for a given type of particle while the dots are data from real tracks. Notice that kaon-pion separation above 700 MeV is almost impossible.

to lose energy. The amount of energy lost depends on particle speed. Since an electron with a momentum of 200 MeV/c is moving much faster than a proton with the same momentum, both particle type and momentum are important (see Figure 2.7). When a track is reconstructed, the average charge per unit length deposited along the track (this quantity is known as dE/dx) can be calculated. Using this

information, it is often possible to state with some certainty what type of particle we have reconstructed. This generally works with fair accuracy at low momentum but quickly gets unusable at higher momentum.

With the constant magnetic field in the CLEO II.V drift chambers, it is possible to get fairly precise measurements of momentum. But using the magnetic field alone, it is not possible to tell the difference between a 200 MeV pion and a 200 MeV kaon. If it were possible to determine the speed of the particle, one could deduce the mass and therefore particle type. That is exactly the idea behind using the time of flight system. For relatively slow moving particles, we can use the TOF detector to determine the length of time it took for a particle to go from the interaction point to the detector. After calculating the path length, the speed is now known.

Neither method works well with high momentum tracks since the speed of a particle is then very close to the speed of light regardless of particle type. It was this shortcoming that became one of the largest motivations for the upgrade to CLEO III.

2.4 Monte Carlo

In addition to using the data CLEO collected when CESR is running, we also use simulated data called Monte Carlo (MC) for the purposes of testing analysis programs and measuring efficiencies. At CLEO, the generation of Monte Carlo has two steps. The first program, called “QQ” simulates $e^+e^- \rightarrow q\bar{q}$ production followed by hadronization and decays all of the unstable¹² particles¹³. The second program, CLEOG (which is based on CERN’s Geant[14]), simulates the passage of these decay products through the material of the CLEO detector and simulates the responses of the detectors. The CLEOG output is then analyzed as if it were raw data.

¹²On the time scale that CLEO is dealing with, electrons, muons, kaons, pions, protons, and photons are all considered stable. Almost everything else is either unstable or undetectable by CLEO’s detectors.

¹³All of the short-lived particles have their decays and momenta calculated in QQ. Longer lived particles (e.g. K_S^0 and Λ s) have their decays calculated in the next step, CLEOG.

Monte Carlo is generated in two different ways: Signal MC and Generic MC. Signal MC is where every event generated has the decay chain that you are looking for and it is useful for calculating efficiency. Generic MC is generated so that the types of particles and decay modes match our best knowledge of what actually happens at an accelerator like CESR. On CLEO, we often divide generic MC into subtypes: $b\bar{b}$ and continuum. $b\bar{b}$ generic MC means $e^+e^- \rightarrow b\bar{b}$. Continuum MC has $e^+e^- \rightarrow q\bar{q}$, where $q = u, d, s,$ and c .

A final note about Monte Carlo. In addition to everything that is available for real data, we also have a list of what the decay in each event really is. This information lets us “tag” a reconstructed track candidate with a generated track. Later, we will see just how useful this information is.

Chapter 3

Dalitz Analysis of $D^0 \rightarrow \pi^- \pi^+ \pi^0$

3.1 Introduction

3.1.1 Motivation

We are studying the resonant substructure of the Cabbibo suppressed decay $D^0 \rightarrow \pi^- \pi^+ \pi^0$ using the Dalitz Plot technique. There are two recently published Dalitz analyses to which it would be interesting to compare the analysis presented here: CLEO's $D^0 \rightarrow K^- \pi^+ \pi^0$ and E791's $D^+ \rightarrow \pi^- \pi^+ \pi^+$. [18, 19]

Studying the Cabbibo favored decay $D^0 \rightarrow K^- \pi^+ \pi^0$ at CLEO uses much of the same machinery needed to investigate $D^0 \rightarrow \pi^- \pi^+ \pi^0$. Since $D^0 \rightarrow \pi^- \pi^+ \pi^0$ is Cabbibo suppressed, the expected number of signal events should be smaller than $D^0 \rightarrow K^- \pi^+ \pi^0$, also suggesting that the signal fraction will be smaller.

The E791 Dalitz analysis of $D^+ \rightarrow \pi^- \pi^+ \pi^+$ found significant evidence for a new broad scalar neutral resonance ($\sigma(500)$). With a mass around 500 MeV and a width of about 300 MeV , this new resonance accounted for a fit fraction over 45% ¹. If such a scalar exists and $D^+ \rightarrow \sigma(500) \pi^+$ has been seen at such significant levels, it would be very interesting to see how important $D^0 \rightarrow \sigma(500) \pi^0$ is in our case.

Finally, since $D^0 \rightarrow \pi^- \pi^+ \pi^0$ is a CP eigenstate, we can also look for CP violation. With no CP violation, $D^0 \rightarrow \rho^+ \pi^-$ should have the same amplitudes

¹Fit fractions can add up to more than 100% due to interference. See Section 3.4.4 for more details.

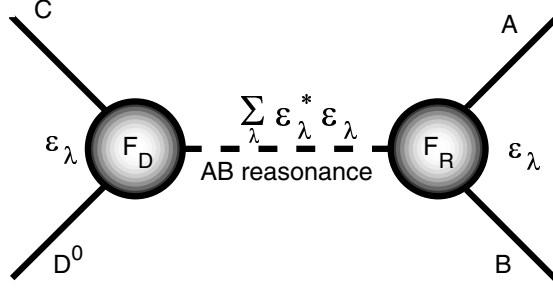


Figure 3.1: A representation of $D^0 \rightarrow ABC$ through an AB resonance. Since the initial and final states have no angular momentum, the intermediate spin states are summed over.

and phases as $\overline{D^0} \rightarrow \rho^- \pi^+$. Recent theoretical works suggest that CP violation in $D^0 \rightarrow \pi^- \pi^+ \pi^0$ may be as large as 0.1%. [20, 21], and this is one of the main motivations for doing this analysis.

3.1.2 Three Body Decays

When discussing three body final states, it is important to distinguish between the two different decay modes: resonant and non-resonant. In the former, the D^0 can decay into an intermediate resonance and one final state daughter and the intermediate resonance then decays into the two other daughters, as shown in Figure 3.1. In the latter, the D^0 can decay directly into the three daughters.

- Examples of Resonant Decays:

$$D^0 \rightarrow \begin{matrix} \rho^0 \pi^0 \\ \swarrow \searrow \\ \pi^- \pi^+ \end{matrix} \quad D^0 \rightarrow \begin{matrix} \rho^+ \pi^- \\ \swarrow \searrow \\ \pi^+ \pi^0 \end{matrix} \quad D^0 \rightarrow \begin{matrix} \rho^- \pi^+ \\ \swarrow \searrow \\ \pi^- \pi^0 \end{matrix}$$

- Non Resonant decay

$$D^0 \rightarrow \pi^- \pi^+ \pi^0$$

See Figure 3.2 for examples of Feynman diagrams. It is important to note that $D^0 \rightarrow K_S^0 \pi^0$, $K_S^0 \rightarrow \pi^- \pi^+$ is essentially two two-body decays since the K_S lives so long. We therefore do not expect it to interfere with the other resonances (see Section 3.2.2 for more on the K_S^0).

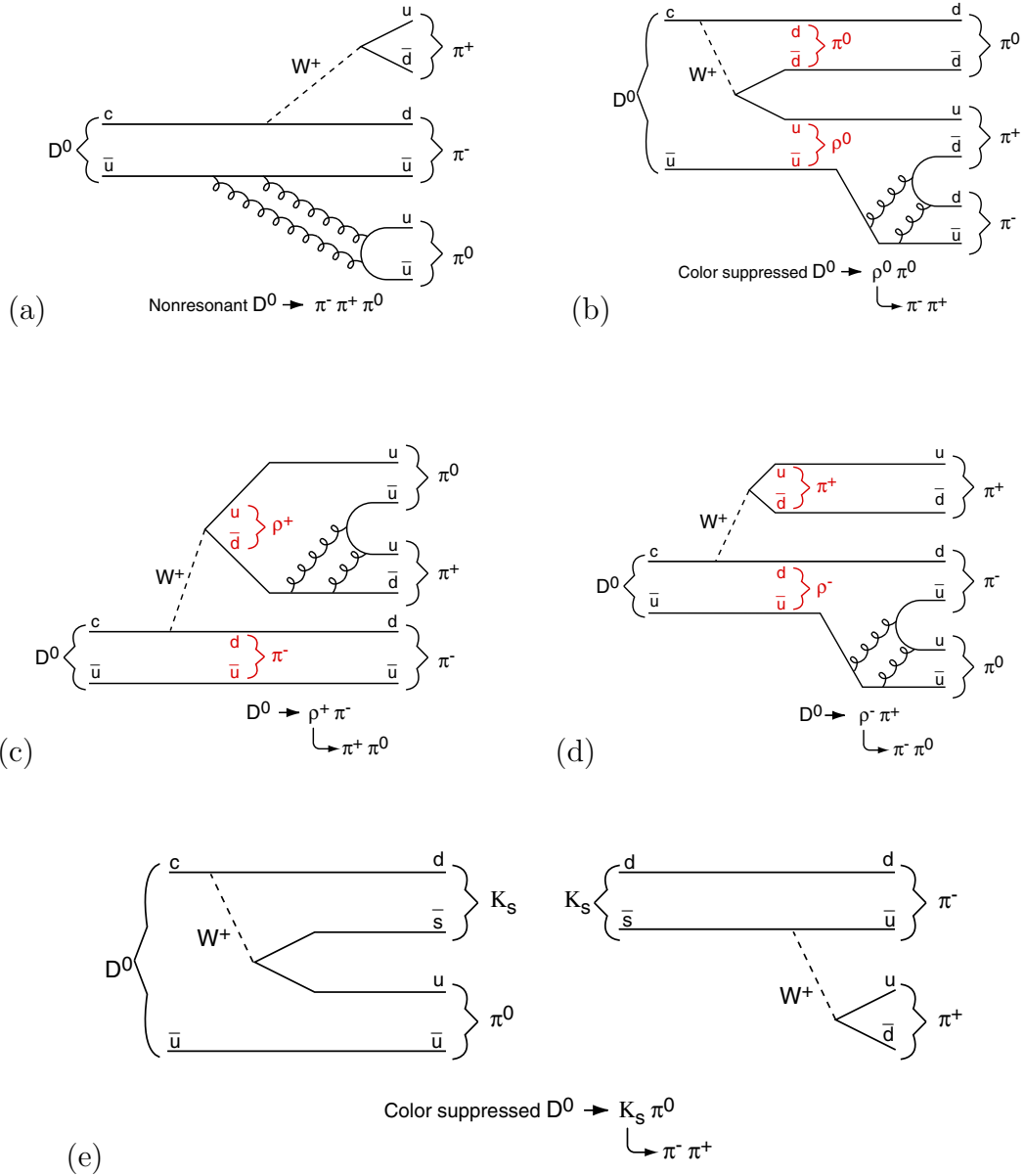


Figure 3.2: Shown are examples of (a) a nonresonant decay, (b) a neutral intermediate state (ρ^0), (c) a positively charged intermediate state (ρ^+), (d) a negatively charged intermediate state (ρ^-), and (e) $D^0 \rightarrow K_S^0 \pi^0$.

In this analysis we are looking at a spin 0 particle decaying into three spin 0 particles. Since there is no spin in either the initial or final states, only two degrees of freedom are needed to describe this system. To see this, we start with the D^0 in its rest frame. The three daughters each have four degrees of freedom (their four momentum). We have three constraints (one for each daughter) because the mass of each daughter is known, and four more constraints due to conservation of energy and momentum. Finally, since the D^0 is a spinless particle, the three constraints describing the orientation of the decay are irrelevant (i.e. $12 - 3 - 4 - 3 = 2$). It is conventional to pick the mass-squared of two of the three daughter particles as the degrees of freedom (i.e. $m_{\pi^-\pi^+}^2$, $m_{\pi^+\pi^0}^2$, and $m_{\pi^-\pi^0}^2$). It is important to note that only two of these three variables are independent since conservation of energy yields:

$$m_{D^0}^2 + m_{\pi^-}^2 + m_{\pi^+}^2 + m_{\pi^0}^2 = m_{\pi^-\pi^+}^2 + m_{\pi^+\pi^0}^2 + m_{\pi^-\pi^0}^2 \quad (3.1)$$

Choosing two of the $\pi\pi$ mass squared terms as our parameters turns out to be an appropriate choice since, when averaged over intermediate spin states, the partial width is proportional to the matrix element squared (i.e. it does not depend on its position in $m_{\pi^-\pi^+}^2 - m_{\pi^+\pi^0}^2$ space):

$$d\Gamma = \frac{1}{256 \pi^3 m_{D^0}^2} |\mathcal{M}|^2 dm_{\pi^-\pi^+}^2 dm_{\pi^+\pi^0}^2 \quad (3.2)$$

3.1.3 Dalitz Plots

As mentioned above, there are two independent variables in the three $\pi\pi$ mass squared combinations. We are going to pick two and use them as the x and y variables. A “Dalitz Plot” is simply a scatter plot of all candidates in the x, y plane. In our $D^0 \rightarrow \pi^-\pi^+\pi^0$, we plot $m_{\pi^+\pi^0}^2$ versus $m_{\pi^-\pi^+}^2$ (see Figure 3.3). As one would hope, we can use any of the six possibilities for x and y and it will not change the results.²

²For a complete look at how x and y are defined for $\overline{D^0} \rightarrow \pi^+\pi^-\pi^0$, please see Section 3.3.1

The reason that Dalitz Plots are so useful is apparent from Equation 3.2. Any structure that shows up in the Dalitz plot is due entirely to \mathcal{M} . Intermediate resonances will show up as bands on the plot. With our choices of x , y , and z ($\equiv m_{\pi^-\pi^0}^2$), neutral resonances will show up as vertical bands, positively charged resonances as horizontal bands, and negatively charged resonances as diagonal bands. To illustrate this, consider $D^0 \rightarrow K_S^0 \pi^0$ where $K_S^0 \rightarrow \pi^-\pi^+$. The K_S^0 is a particle with a very narrow mass distribution. In other words, we expect the invariant mass of its daughters to be closely distributed around the known K_S^0 mass. For D^0 s that decay via $K_S^0 \pi^0$, the invariant mass squared of the π^- and π^+ should be distributed about $m_{K_S^0}^2$. Since $m_{\pi^-\pi^+}^2$ is our x variable, we will see the K_S^0 as a vertical band (See the Figure 3.4 (a)).

When comparing Dalitz plot fits to data, it is customary to compare the three projections ($x = m_{\pi^-\pi^+}^2$, $y = m_{\pi^+\pi^0}^2$, $z = m_{\pi^-\pi^0}^2$ for $D^0 \rightarrow \pi^-\pi^+\pi^0$; please see Section 3.3.1 for $\overline{D}^0 \rightarrow \pi^+\pi^-\pi^0$ definitions of x , y , and z .) as shown in Figure 3.4. For spin 1 (and higher) resonances, the ‘‘reflection’’ of a resonance shows up on the other two axes. For a more intuitive look at how the projections are made, see Figure 3.5.

3.2 Theory

3.2.1 Representations of the Resonances

When deciding how to represent a resonant decay (e.g. $D^0 \rightarrow (AB)_{res} C$, $(AB)_{res} \rightarrow A B$), it is most instructive to start with the Feynman rules. If the D^0 and the resonance were point-like particles, we would have:

$$\begin{aligned} \mathcal{M}_{D^0 \rightarrow AB_{res} C} &= (P_D + P_C)_\mu (\text{Massive Propagator})^{\mu\nu} (P_A - P_B)_\nu \\ &= (P_D + P_C)_\mu \frac{\Sigma_\lambda \epsilon_\lambda^{\mu*} \epsilon_\lambda^\nu}{M_{res}^2 - M_{AB}^2 - im_{res} \Gamma_{res}} (P_A - P_B)_\nu \end{aligned} \quad (3.3)$$

These particles are not, however, point-like and do have a finite size. As a result, there are decay form factors added at each vertex. In general these are unknown,

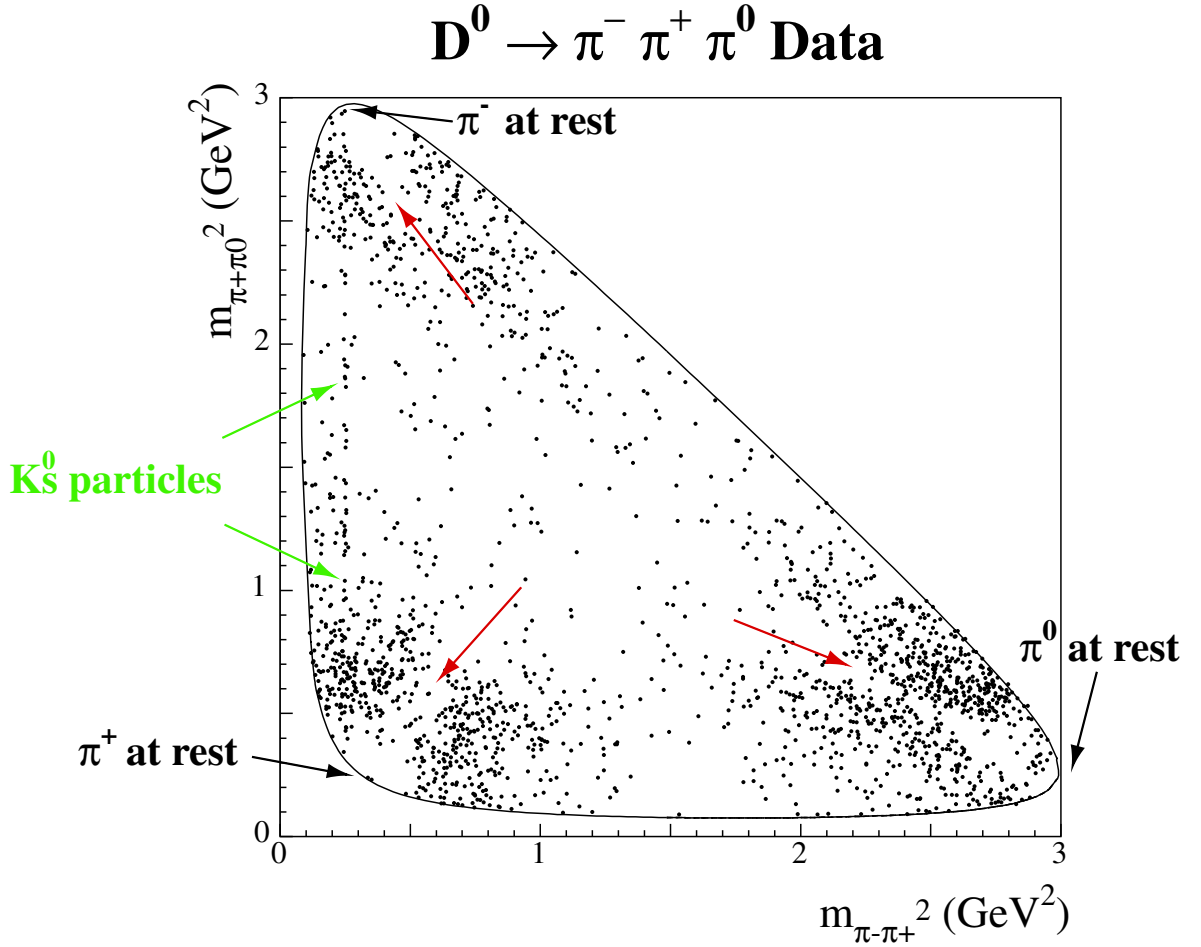


Figure 3.3: A plot of data from CLEO II.V of $m_{\pi^+\pi^0}^2$ versus $m_{\pi^-\pi^+}^2$ for reconstructed $D^0 \rightarrow \pi^-\pi^+\pi^0$ events. Note that each of the three corners is where one of the pions is at rest in the D^0 frame. The long thin vertical band on the left are K_S^0 . The colored arrows point to three regions on the Dalitz Plot where we can see destructive interference.

Spin	Factor
0	1
1	$\frac{\sqrt{1+R^2 p_r^2} e_s}{\sqrt{1+R^2 p^2}}$

Table 3.1: Blatt Weisskopf Penetration Factors. R is the radius of the meson. In our case, we have picked values from 0 GeV^{-1} and 10 GeV^{-1} with very little effect on the fit results.

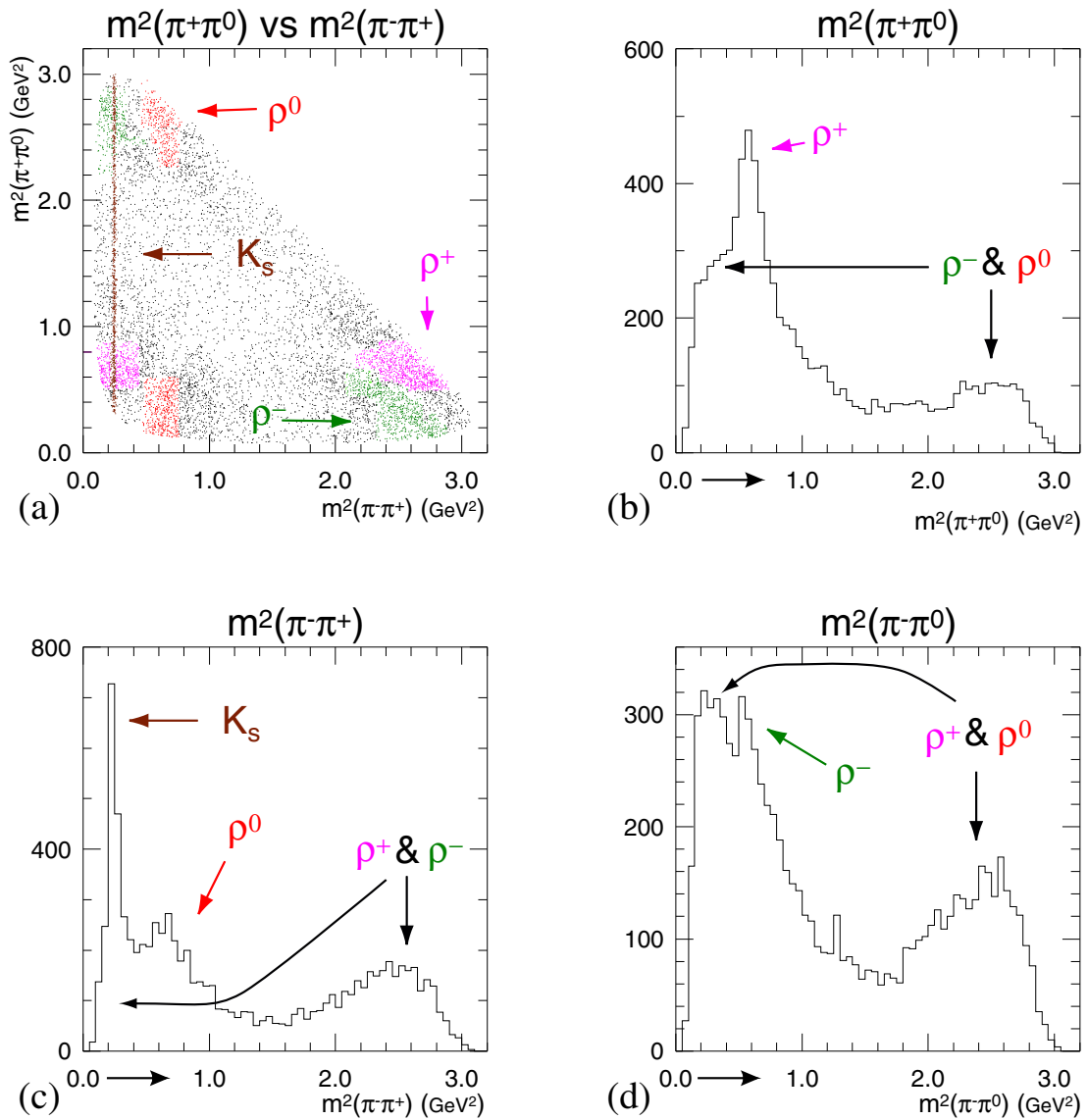


Figure 3.4: The $D^0 \rightarrow \pi^- \pi^+ \pi^0$ Dalitz plot (a) and the x (c), y (b), and z (d) projections. Note: All resonances are colored by hand for visualization.

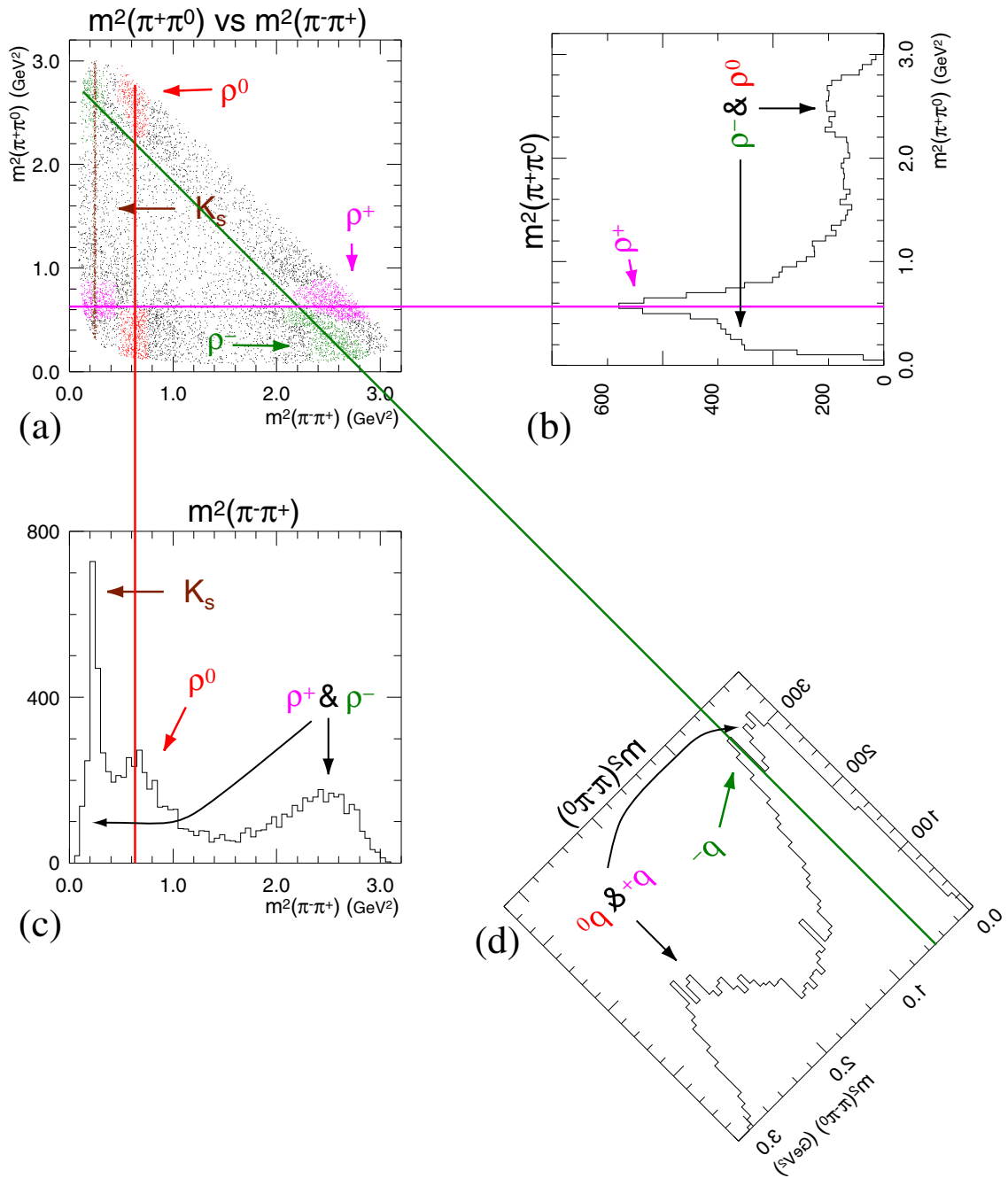


Figure 3.5: Imagine the three lines sweeping across the Dalitz plot (a) in order to understand how the projections are made. For this purpose, the x projection (c) ($m^2_{\pi^-\pi^+}$) is fine as presented. The y projection (b) ($m^2_{\pi^+\pi^0}$) needs to be rotated counter-clockwise by 90 degrees. The z projection ($m^2_{\pi^-\pi^0}$) (d) needs to be flipped about its vertical axis and then rotated counter-clockwise by 45 degrees. Note: All resonances are colored by hand for visualization.

but in practice they are often set to Blatt-Weisskopf penetration factors (see Table 3.1).[22] In addition, we now use a mass dependant function for the resonance's width that depends on the spin: [23]

$$\Gamma(q) = \Gamma_0 \left(\frac{P}{P_{res}} \right)^{2J+1} \left(\frac{m_{res}}{M} \right) F_{res}^2. \quad (3.4)$$

The matrix element is now:

$$\mathcal{M}_{D^0 \rightarrow AB_{res} C} = F_{D^0}(q^2) F_{res}(q^2) (P_D + P_C)_\mu \frac{\sum_\lambda \epsilon_\lambda^{\mu*} \epsilon_\lambda^\nu}{M_{res}^2 - M_{AB}^2 - im_{res}\Gamma(q)} (P_A - P_B)_\nu \quad (3.5)$$

The non-resonant matrix element is simply a constant (i.e. it does not change over the area of the Dalitz Plot).

For a scalar resonance, we simply get:

$$\mathcal{M}_{scalar} = F_{D^0} F_{res} \frac{1}{m_{res}^2 - m_{AB}^2 - im_{res}\Gamma(q)} \quad (3.6)$$

For a vector resonance, the spin sum in the numerator of Equation 3.3 can be evaluated to:[24]

$$-g^{\mu\nu} + \frac{P_{AB}^\mu P_{AB}^\nu}{m^2} \quad (3.7)$$

$$\mathcal{M}_{vector} = F_{D^0} F_{res} \frac{M_{AC}^2 - M_{BC}^2 + \frac{(M_D^2 - M_C^2)(M_B^2 - M_A^2)}{M_{res}^2}}{m_{res}^2 - m_{AB}^2 - im_{res}\Gamma(q)}. \quad (3.8)$$

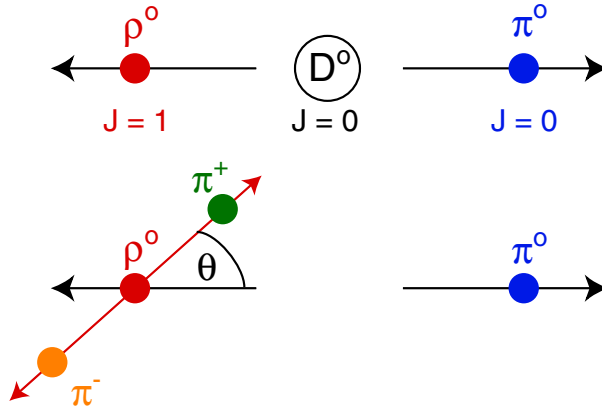
Although it is not obvious from looking at this formula, this matrix element is proportional to $\cos(\theta)$ in the D^0 rest frame (θ is the angle between the momentum vector of the resonance and the momentum vector of one of the daughters). See Figure 3.6 for clarification. It is this $\cos(\theta)$ dependance which causes the dip in the central region of the Dalitz plot characteristic of spin 1 resonances.

It is unknown, *a priori*, how much of each resonance we have. We therefore weigh each piece of the matrix element with an amplitude and a phase. The total matrix element is simply the sum of all of the pieces:

$$\begin{aligned}
\mathcal{M}_{D^0 \rightarrow \pi^- \pi^+ \pi^0} &= \mathcal{A}_{non\ res} \cdot e^{i \phi_{non\ res}} && + \\
&\mathcal{A}_{\rho^+ \pi^-} \cdot e^{i \phi_{\rho^+ \pi^-}} \cdot \mathcal{M}_{D^0 \rightarrow \rho^+ \pi^-} && + \\
&\mathcal{A}_{\rho^- \pi^+} \cdot e^{i \phi_{\rho^- \pi^+}} \cdot \mathcal{M}_{D^0 \rightarrow \rho^- \pi^+} && + \\
&\mathcal{A}_{\rho^0 \pi^0} \cdot e^{i \phi_{\rho^0 \pi^0}} \cdot \mathcal{M}_{D^0 \rightarrow \rho^0 \pi^0} && \\
&+ \dots && \\
&= \mathcal{A}_{non\ res} \cdot e^{i \phi_{non\ res}} && + \\
&\mathcal{A}_{\rho^+ \pi^-} \cdot e^{i \phi_{\rho^+ \pi^-}} && + \\
&\mathcal{A}_{\rho^- \pi^+} \cdot e^{i \phi_{\rho^- \pi^+}} && + \\
&\mathcal{A}_{\rho^0 \pi^0} \cdot e^{i \phi_{\rho^0 \pi^0}} && \\
&+ \dots &&
\end{aligned} \tag{3.9}$$

It is these amplitudes and phases (e.g. $\mathcal{A}_{\rho^- \pi^+}$, $\phi_{\rho^- \pi^+}$, etc.) that will be varied to fit the model to the data (i.e. they are the free fit parameters).

A final note about the matrix element. One can multiply all of the pieces of the



$$Y_1^0 = \sqrt{\frac{3}{4\pi}} \cos(\theta)$$

Figure 3.6: Since the D^0 is a spinless particle, the ρ^0 must be in a $|1, 0\rangle$ angular momentum state in the D^0 rest frame (when we quantize along the π^0 direction). The daughters of the ρ^0 therefore decay preferentially parallel to its momentum (i.e. The amplitude has a $\cos(\theta)$ dependence in the D^0 rest frame).

matrix element by complex constant (i.e. an amplitude and phase) and the results would be identical, since the observed rate is proportional to $|\mathcal{M}|^2$ and we are fitting only for the shape of $|\mathcal{M}|^2$, not its absolute value. Due to this ambiguity, we choose to fix it so that the ρ^+ (the dominant resonance) has an amplitude of 1 and a phase of 0.

3.2.2 How We Treat $D^0 \rightarrow K_S^0 \pi^0$

The K_S^0 is different from all other resonances accessible in the $D^0 \rightarrow \pi^- \pi^+ \pi^0$ channel in that it lives for a very long time. As a consequence, the K_S^0 is easily distinguishable from all other resonances and therefore will not interfere with other them.

As a result of this, the K_S^0 will be treated differently than the other intermediate resonances. First, it will be represented by a Gaussian instead of a Breit-Wigner³.

³In general a Breit-Wigner is used to properly describe the width of a particle. In the case of the

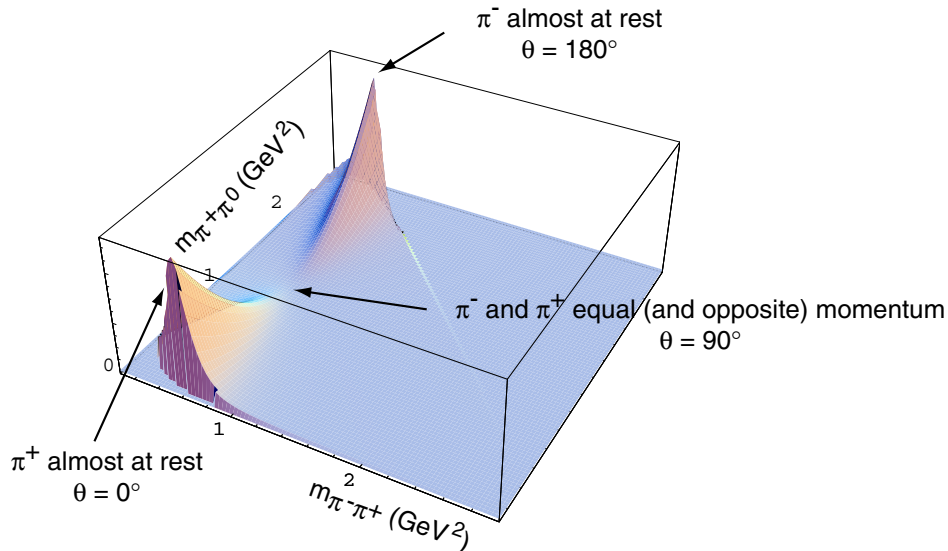


Figure 3.7: $|Amplitude|^2$ for the vector $\pi^-\pi^+$ resonance ρ^0 . When the π^+ comes out opposite to the ρ^0 direction, it is almost at rest and corresponds to $\theta = 0$ deg. The π^- is almost at rest when $\theta = 180$ deg. When the pions come out perpendicular to the ρ^0 ($\theta = 90$ deg), they have equal momentum. We can see the $\cos^2(\theta)$ dependence mentioned in Figure 3.6.

Second, it will be treated as a floating part of the background instead of as part of the signal. Specifically, there will be no phase describing the K_S^0 and the amplitude of the K_S^0 will not influence the fit fractions of the other resonances.

3.3 Analysis

This analysis uses *Driver++*, a mixture of C++ code that works within the existing FORTRAN framework using new technology that gives users access to all common blocks inside *C++*. In keeping with the latest CLEO II.V analysis techniques, we include a single include file *roar_coms.inc* and call a single fill routine *fill_coms.F*. Otherwise this analysis is a standard CLEO II.V analysis (see Appendix A for more

K_S^0 , the particle is so narrow that all of the width that we measure is detector resolution, not the intrinsic width of the K_S^0 . Detector resolution is better modelled by a Gaussian in this case.

details about Driver and *Driver++*).

3.3.1 General Overview

We are studying the following decay chain (particles in red are directly observed; those in black are constructed from the observed particles):

$$\begin{array}{l}
 D^{*+} \rightarrow D^0 \pi_{\text{slow}}^+ \\
 \quad \quad \quad \hookrightarrow \pi^- \pi^+ \pi^0 \\
 \quad \quad \quad \quad \quad \quad \hookrightarrow \gamma \gamma
 \end{array}$$

In this analysis, like most CLEO charm analyses, we are using a D^{*+} tag. We first construct π^0 candidates from photon candidates in the calorimeter. Next, we construct D^0 candidates from two oppositely charged tracks and one of the π^0 candidates. By adding suitable π_{slow}^+ candidates⁴, D^{*+} candidates are created. To increase our ability to distinguish signal from background, we refit the slow pion using the beam spot and the D^0 using a vertexing package called KWFIT (see Figure 3.9). For every candidate passing our event selection criteria, we calculate $m_{\pi^-\pi^+}^2$ and $m_{\pi^+\pi^0}^2$ (these are the x and y variables respectively that we use for the Dalitz plot; see below for their definition).

D^* Tagging

While we will discuss all cuts later in section 3.3.2, the slow pion from the D^* decay deserves special mention. It has two main purposes. First, we use it to tag the flavor of the D^0 candidate. Second, it is very effective for reducing the backgrounds.

We can use the sign of the slow pion to tell us whether we have a D^0 or a $\overline{D^0}$ candidate. A positive slow pion implies a D^0 while a negative slow pion means a

⁴The slow pion has its name for two reasons. First, it has a very low momentum in the D^* rest frame ($39 \text{ MeV}/c$). Second, we want to differentiate this pion from the other final state daughters.

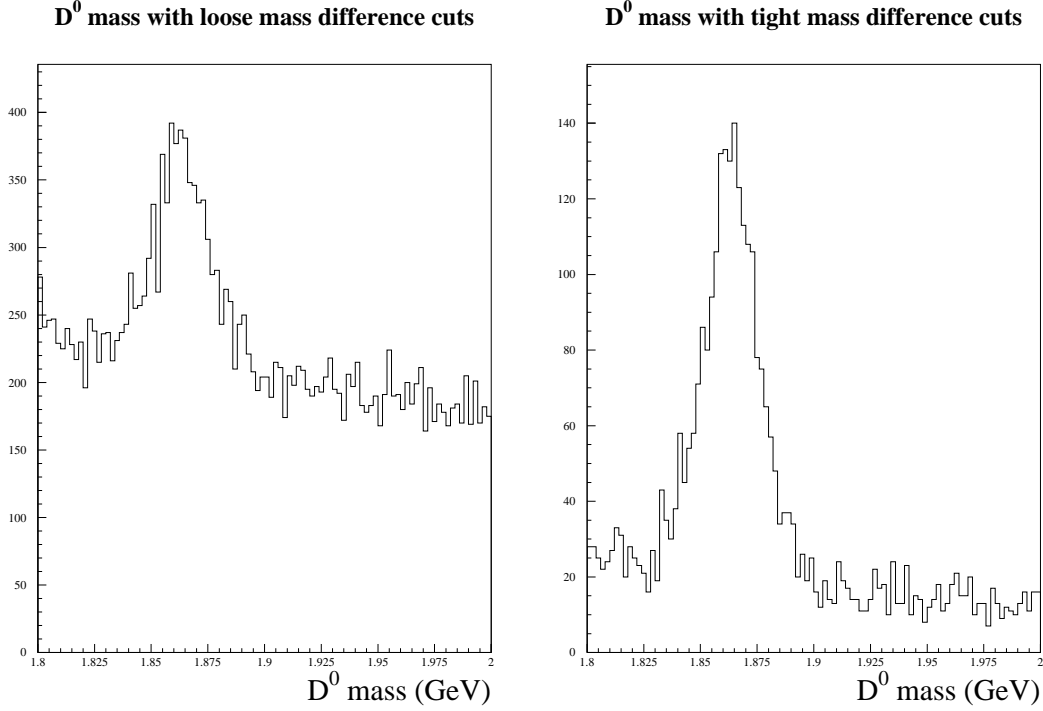


Figure 3.8: Shown are the D^0 mass distributions for loose mass difference cuts ($-10 \text{ MeV}/c^2 \leq \text{mass difference} \leq 15 \text{ MeV}/c^2$) and tight mass difference cuts ($-0.6 \text{ MeV}/c^2 \leq \text{mass difference} \leq 0.7 \text{ MeV}/c^2$) respectively.

$\overline{D^0}$. This will be particularly important in the next sections on charge conjugation (below) and CP violation measurements (Section 3.4.5).

By demanding that D^0 s come from D^{*+} s, we have another variable that we can use to discriminate between signal and background. We define a mass difference to be:

$$\text{mass difference} = m_{D^{*+}\text{candidate}} - m_{D^0\text{candidate}^-} - (m_{D^{*+}} - m_{D^0})_{PDG} \quad (3.10)$$

As can be seen in Figure 3.8, this can be a very powerful tool in discriminating signal from background: tightening the mass difference requirement clearly increases the signal to background ratio significantly.

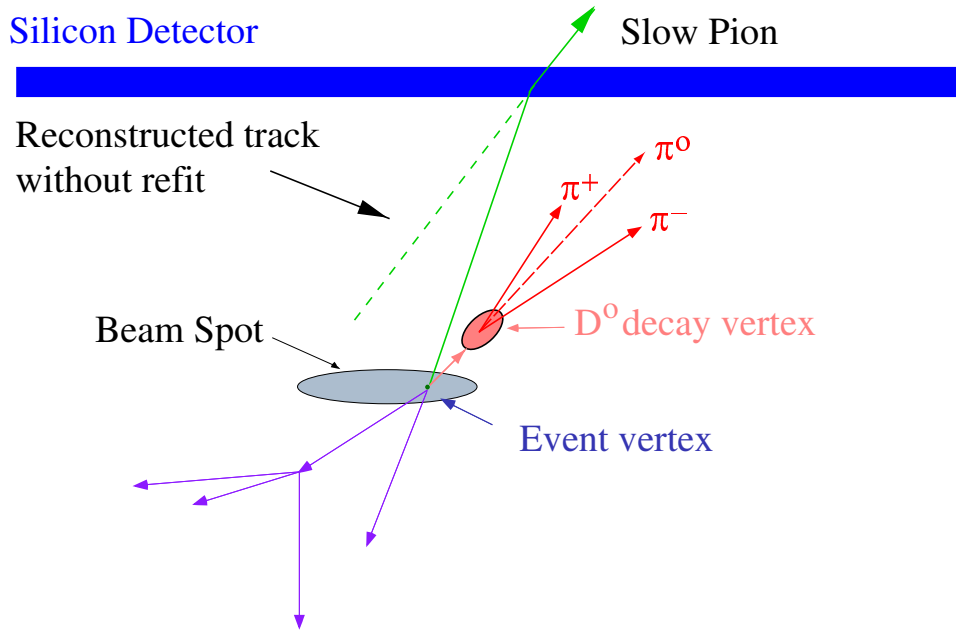


Figure 3.9: Using the D^0 and the beam spot we refit the slow pion. **Note:** We use the position information from the charged pions, not from the neutral π^0 , to calculate the vertex of the D^0 .

3.3.2 Event Selection

There are two types of event selection criteria (cuts, for short) that we use: track cuts and event cuts. The track cuts are in place to make sure we only use well reconstructed tracks. The event cuts are used to maximize signal while minimizing background.

Charged Tracks Candidates

All charged track cuts are designed to make sure we only use well-reconstructed track candidates. We require:

- $trackman > 0$
- not *dredge* or *z - escape*
- $kinCD == 0$ ($kinCD == 0$ or 2 for the slow pion)

- $VD + DR \text{ hits} \geq 15$
- At least two $r - \phi$ and two z silicon hits

The first two cuts are made to be sure that we do not reconstruct a ghost track (e.g. an out of time track or the wrong end of a particle that is curling multiple times in the drift chamber). The $kinCD == 0$ requirement ensures that we have particles coming from the primary vertex. When we allow also $kinCD == 2$, we let in particles that the track fitter believes may be from a secondary vertex. While the slow pion should come from the primary vertex, it may scatter sufficiently in the SVX so that it is reconstructed as a secondary vertex track (the pion daughters of the K_S^0 are a good example of secondary vertex tracks).

π^0 Candidates

We use a standard CLEO package for finding π^0 s called CCFC. This reconstructs π^0 candidates out of pairs of showers in the calorimeter. In order to be considered as a π^0 , the candidate must pass the following criteria:

- The invariant mass of the two photons must be between 105 MeV and 165 MeV .
- Neither photon daughter can be associated with any charged track.
- At least one daughter must be in the “good barrel” region ($|\cos(\theta_{daughter})| < 0.71$).
- The other daughter can be in the “good barrel”, “bad barrel” ($0.71 \leq |\cos(\theta_{daughter})| < 0.81$), or “good endcap” ($0.85 \leq |\cos(\theta_{daughter})| < 0.95$) region.
- Daughters in the “good barrel” region must be at least 30 MeV ; those in the other regions must have an energy of at least 50 MeV .

It is important to note that the preference for “good barrel” photons exists for two reasons. First, there is less material in between the “good barrel” parts of the CC and the interaction region than in the other regions of the CC, and we therefore get more accurate measurements of energy. Second, the closer the position of CC crystals gets

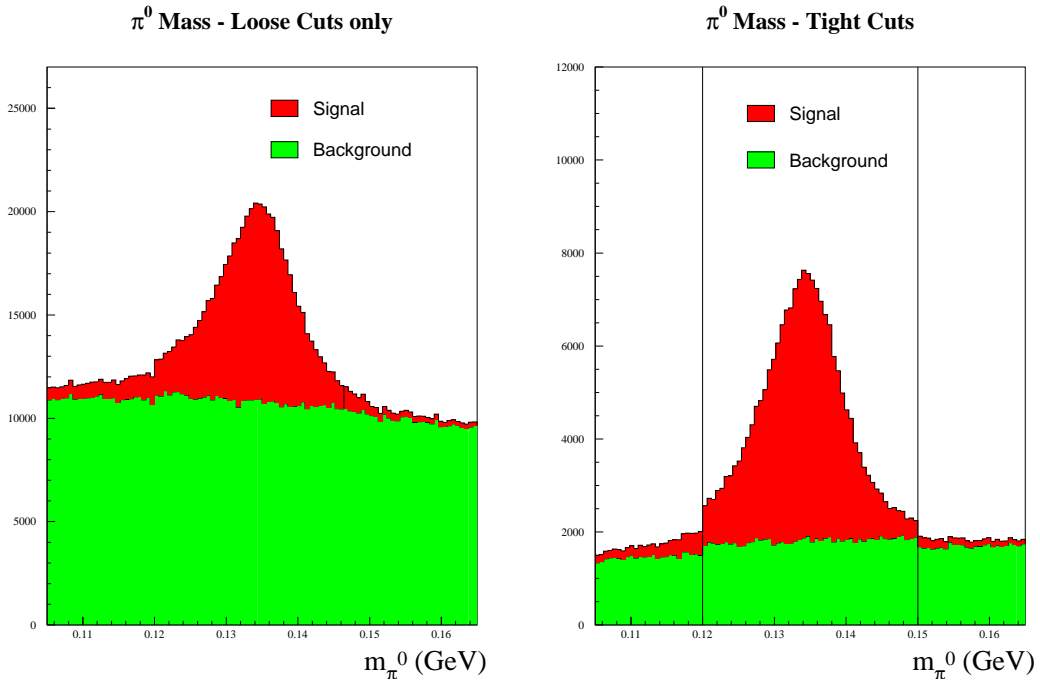


Figure 3.10: These two plots of reconstructed π^0 mass (the invariant mass of the two γ daughters) were generated from analyzing 100,000 MC events. The plot on the left shows real and fake π^0 s with only the CCFC cuts. The plot on the right is with all of our additional tighter cuts (except the mass cut). The vertical lines show the lower and upper mass cuts used in this analysis.

to the beam, the more likely that hits are from noise and beam backgrounds rather than the physics we want to study.

To further reduce the number of fake π^0 s, we tighten the above criteria. See Figure 3.10 to see the effects of the cuts below.

- The $\gamma - \gamma$ invariant mass be between 120 MeV and 150 MeV .
- The χ^2 of the π^0 mass refit be less than 100.
- Both daughters be in the good barrel.
- Both daughters have an energy of at least 100 MeV .

Event cuts

As mentioned above, event cuts are used to distinguish signal from background. All events must have:

- The KWFIT D^0 mass should be between 1.841 GeV and 1.885 GeV (see Figure 3.11).
- The difference between the KWFIT $D^{*+} - D^0$ mass difference and the Particle Data Group value should fall between -0.604 MeV and 0.691 MeV (see Figure 3.12). This cut is asymmetric because the PDG value of the mass difference is not identical to our average measured value of the mass difference.
- D^{*+} momentum fraction $X_{D^*} \equiv \frac{p_{D^*}}{p_{D^*max}}$ should be greater than 0.70 (see Figure 3.13). In general, most reconstructed tracks have relatively low momentum. By reconstructing only the fastest D^{*+} s (those with bigger X_{D^*}), we avoid reconstructing a lot of combinations where one or more of the tracks does not come from a real D^{*+} .

3.3.3 Possible Resonances

Before doing a Dalitz plot analysis, we must decide which possible intermediate resonances to consider. Table 3.2 lists all possible (and reasonable) resonances considered in this analysis.

3.4 Dalitz Fitter

3.4.1 Theory

We use an Unbinned Maximum Likelihood Fitter. This means that we minimize:

$$\mathcal{F} = \sum_{events} (-2 \ln \mathcal{L}), \quad (3.12)$$

D^0 Mass

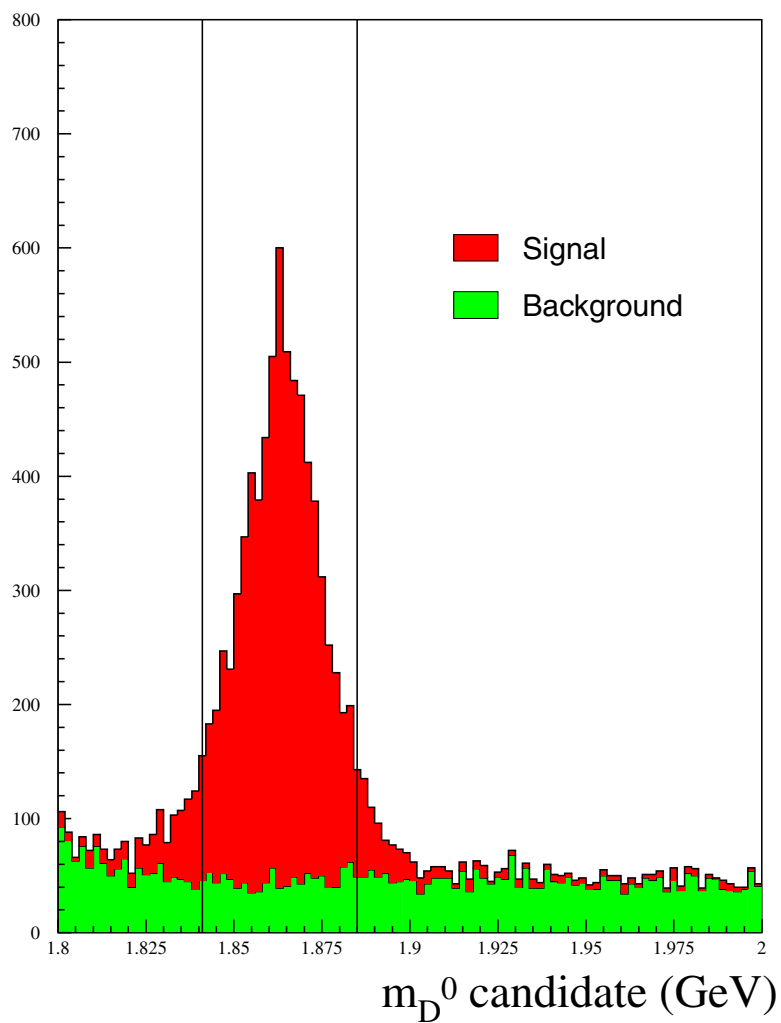


Figure 3.11: The analysis code was run on generic CLEO II.V MC (both $b\bar{b}$ and continuum) and all cuts were used except the D^0 mass cuts. The two vertical lines represent the lower and upper D^0 mass cuts used in this analysis..

$D^{*+} - D^0$ Mass Difference

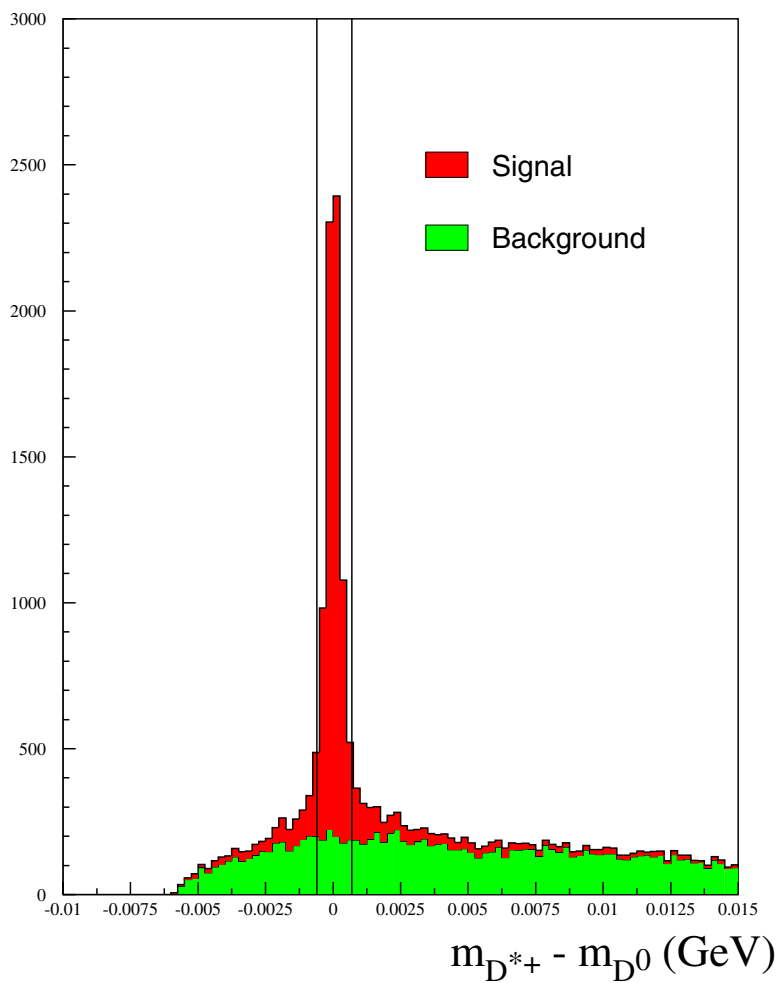


Figure 3.12: The analysis code was run on generic CLEO II.V MC (both $b\bar{b}$ and continuum) and all cuts were used except the $D^{*+} - D^0$ mass difference cuts. The two vertical lines represent the lower and upper $D^{*+} - D^0$ mass difference cuts used in this analysis.

D^{*+} Momentum Fraction

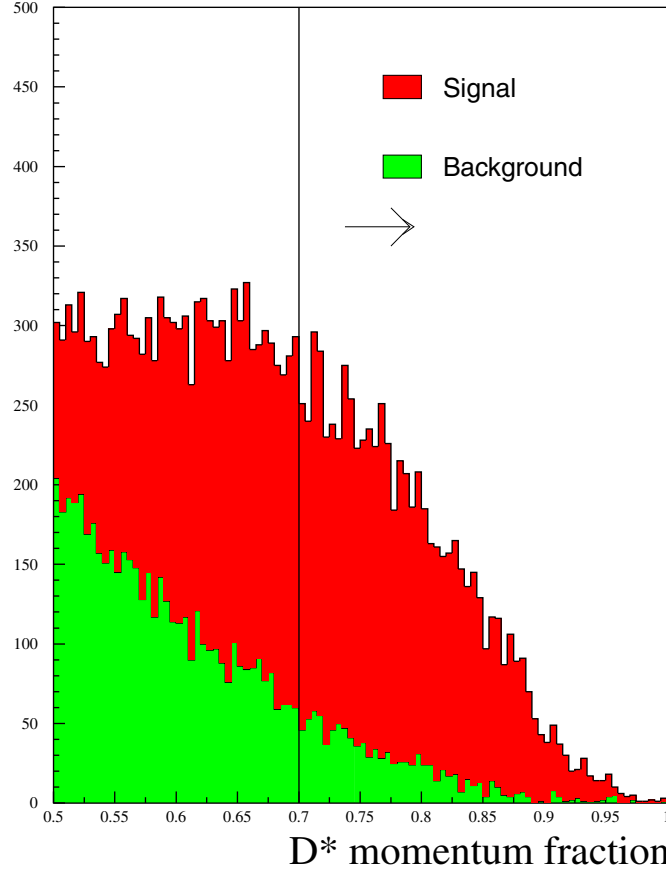


Figure 3.13: The analysis code was run on generic CLEO II.V MC (both $b\bar{b}$ and continuum) and all cuts were used except the X_{D^*} cut. The vertical line represents the lower X_{D^*} cut used in this analysis..

where

$$\mathcal{L} = \left(F \frac{\mathcal{E}(m_{\pi^-\pi^+}^2, m_{\pi^+\pi^0}^2) |\mathcal{M}_{D^0 \rightarrow \pi^-\pi^+\pi^0}|^2}{\mathcal{N}_{signal}} + (1 - F) \frac{\mathcal{B}(m_{\pi^-\pi^+}^2, m_{\pi^+\pi^0}^2)}{\mathcal{N}_{background}} \right) \quad (3.13)$$

- F is fraction of signal events in sample. This quantity is called “Signal Fraction”.
- $\mathcal{E}(m_{\pi^-\pi^+}^2, m_{\pi^+\pi^0}^2)$ is the efficiency for an event falling at point $(m_{\pi^-\pi^+}^2, m_{\pi^+\pi^0}^2)$

Particle	Charge	$\pi\pi$ BR	J^{pc}	Mass	Width
$f_0(400 - 1200)$	0	Dominant	0^{++}	400 – 1200	600 – 1000
$\sigma(500)$	0	Probably		478 ± 30	324 ± 50
$\rho(770)$	0,+,-	100%	1^{--}	769.3	150
$f_0(980)$	0	Dominant	0^{++}	980 ± 10	40 – 100
$f_2(1270)$	0	85%	2^{++}	1275.4	185.1
$\pi(1300)$	0	seen	0^{-+}	1300 ± 10	200 – 600
$f_0(1370)$	0	seen	0^{++}	1200 – 1500	200 – 500
$f_2(1430)$	0	seen?	2^{++}	1430	14 – 150
$\rho(1450)$	0,+,-	seen	1^{--}	1465 ± 25	310 ± 60
$f_0(1500)$	0	seen	0^{++}	1500 ± 10	112 ± 10
$\rho_3(1690)$	0	23.60%	3^{--}	1691 ± 5	161 ± 10
$\rho(1700)$	0,+,-	seen	1^{--}	1700 ± 20	240 ± 60
$f_0(1710)$	0	seen	0^{++}	1715 ± 7	125 ± 12

Table 3.2: A list of all resonances tried in this analysis.[1]

in the Dalitz plot to be detected by CLEO and to pass all of our analysis cuts (discussed in Section 3.5).

- $\mathcal{B}(m_{\pi^-\pi^+}^2, m_{\pi^+\pi^0}^2)$ is the background level at point $(m_{\pi^-\pi^+}^2, m_{\pi^+\pi^0}^2)$ (discussed in Section 3.6).
- $\mathcal{N}_{signal} = \int \mathcal{E}(m_{\pi^-\pi^+}^2, m_{\pi^+\pi^0}^2) |\mathcal{M}_{D^0 \rightarrow \pi^-\pi^+\pi^0}|^2 d\mathcal{DP}$ is the signal normalization.
- $\mathcal{N}_{background} = \int \mathcal{B}(m_{\pi^-\pi^+}^2, m_{\pi^+\pi^0}^2) d\mathcal{DP}$ is the background normalization.

In plain English, for every event we calculate $\mathcal{L} = \text{signal fraction} \times \text{“likelihood”}$ of a signal event being there + background fraction \times “likelihood” of a background event being there. Since we are summing $-2 \ln \mathcal{L}$, we want to minimize the number of “unlikely” events by adjusting the amplitudes and phases of the resonances.

3.4.2 Fitter

The fitter is a slightly modified version of the fitter used in the CLEO II $D^0 \rightarrow K^-\pi^+\pi^0$ analysis. It is written in FORTRAN and uses MINUIT (from CERNLib). The fitter takes as input the x, y coordinates ($m_{\pi^-\pi^+}^2$ and $m_{\pi^+\pi^0}^2$ respectively) of each event as well as a list of starting values for the parameters of the matrix element.

After the fitter has run, the amplitudes and phases for all of the resonances as well as the covariance matrix are extracted from the output files.

3.4.3 Goodness of Fit

Although a concern in all fits, judging the quality of a Dalitz Plot fit can be particularly difficult. Even qualitatively, the best way to do this isn't obvious. There are two quantitative methods that we use.

The first is a very natural extension of the fitting method. Since we are minimizing the log likelihood (see Equation 3.12), we can simply look at the average log likelihood per event ($\sum_{events} (-2 \ln \mathcal{L}) / n_{events}$). This does not give us a very intuitive indication of the quality of the fit, however, since this is not a quantity that is often used in judging fits.

χ^2 would be a great choice, but it requires the data to be binned, and we are doing an unbinned fit. A simple method would be to impose a grid over the Dalitz Plot and bin the events. The problem is that if we pick a reasonably sized grid (say, $150 MeV^2$ per division), we would end up with many bins with few to no events. To get around this problem, we group low occupancy bins together so that no bins have less than 20 events (see Figure 3.14). Now, we simply calculate as usual:

$$\chi^2 = \sum_{bins} \left(\frac{n_i - e_i}{\sigma_i} \right)^2 \quad (3.14)$$

where:

- n_i is the number of events in bin i ,
- e_i is the number of events in bin i according to the fit, and
- σ_i is the error on the number of events in bin i .

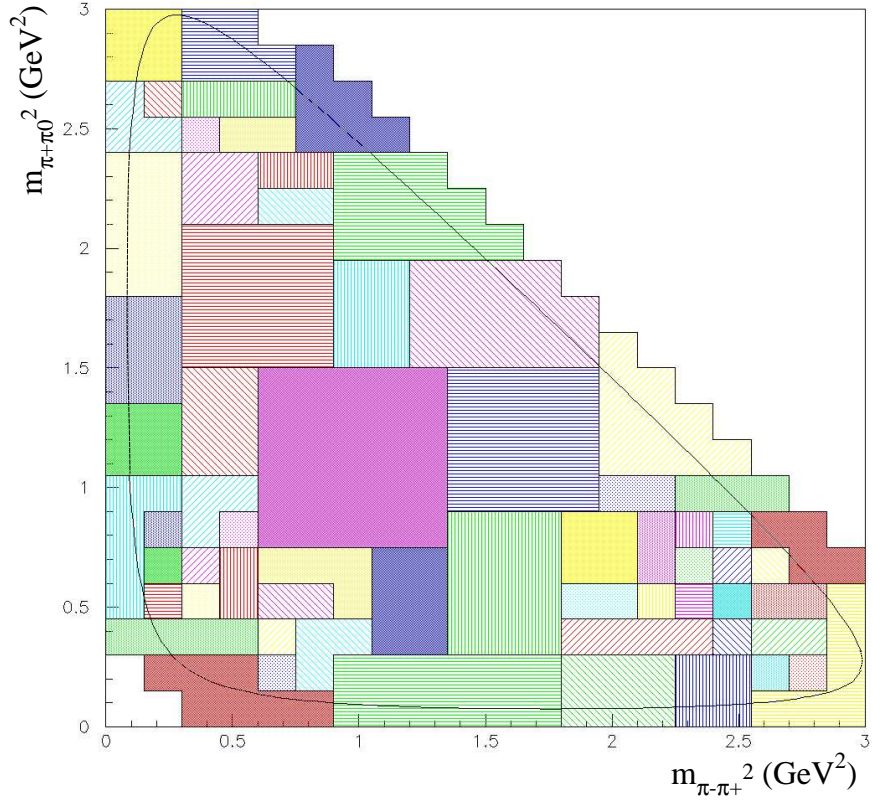


Figure 3.14: The binning that we will use to calculate χ^2 goodness of fit. We started with bins of 150 MeV per side and combined bins until each had a minimum of 20 data events.

3.4.4 Fit Fractions

Defining Fit Fractions

The concept of fit fractions isn't very difficult, but the details can get complicated in Dalitz analyses.

$$\text{The fit fraction of } D^0 \rightarrow X\pi = \frac{\int |\mathcal{M}_{D^0 \rightarrow X\pi}|^2 d\mathcal{DP}}{\int |\mathcal{M}_{D^0 \rightarrow \pi^-\pi^+\pi^0}|^2 d\mathcal{DP}}$$

It is important to note that, due to interference between the different pieces of the matrix element, the fit fraction does not need to add up to 100%. Once we have a best fit for the amplitudes and the phases, getting this number is simple to do using numerical integration. Finding the uncertainty of the fit fraction, however, requires more work.

Finding the Errors on the Fit Fractions

At first look, it seems that one can calculate the error on the fit fraction of a resonance by simply propagating the error on its amplitude. It soon becomes apparent, however, that this is not sufficient. For example, this naïve model would give no error for the ρ^+ since its amplitude is fixed to one, and also ignores how errors in the phase. In order to correctly calculate the error on the fit fractions, we generate a large number of parameter samples using a program that wiggles all of the amplitudes and phases of all the resonances around their fitted values according to the covariance matrix from the original fit. For each “trial,” the fit fraction for each resonance is computed and stored. After 1000 trials, we fit the distribution of fit fractions for each resonance with a Gaussian and use its mean and width as our central value and error respectively (see the left plot in Figure 3.15).

When fitting the fit fraction distributions, the mean is fixed to be non-zero. This can be important when studying resonances that are not very significant (see the right plot in Figure 3.15). In this case, we quote the width of the Gaussian that is fit to the distribution as the error on a zero fit fraction.

3.4.5 \mathcal{A}_{CP}

The concept of CP violation is easy: We look for any differences between the decays $D^0 \rightarrow A B$ and $\overline{D}^0 \rightarrow \overline{A} \overline{B}$ (e.g. are the phases the same? Are the amplitudes the

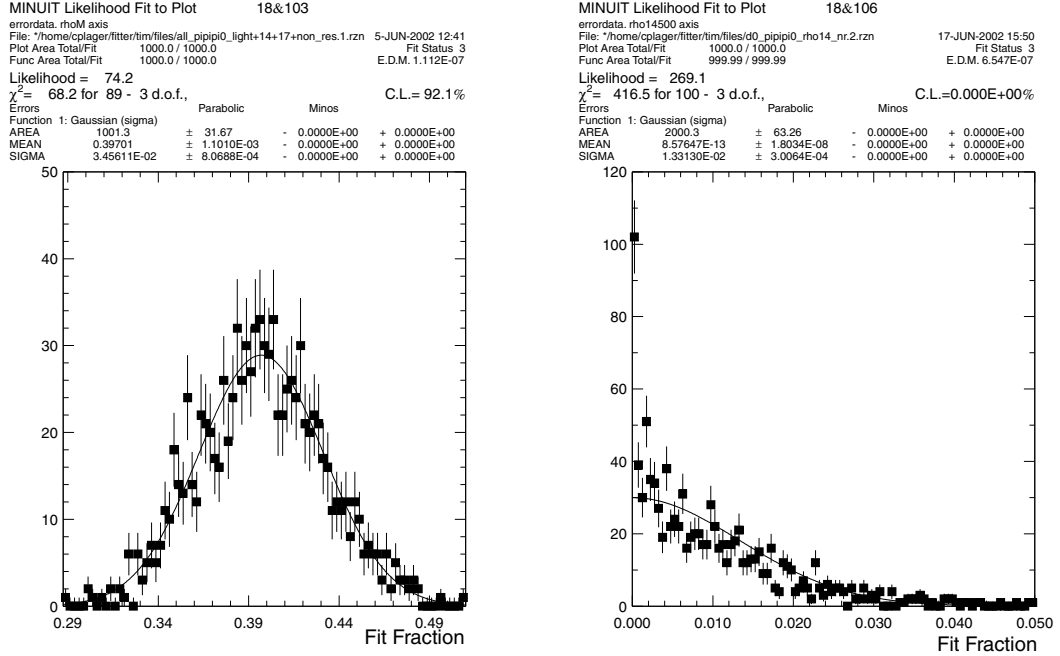


Figure 3.15: The fit of the ρ^- fit fraction distribution (left) and the fit of ρ_{1450}^0 fit fraction distribution (right), both from a set of 1000 trials where the matrix element parameters were varied according to the covariance matrix. For the ρ_{1450}^0 , the distribution is not well represented by a Gaussian. In this case, we quote a zero fit fraction with the error given by the Gaussian fit.

same?) In addition to looking at the fits piece by piece, we also want to define a single number to parameterize CP violation:

$$\mathcal{A}_{CP} = \frac{\int \frac{|\mathcal{M}_{D^0}|^2 - |\mathcal{M}_{\overline{D^0}}|^2}{|\mathcal{M}_{D^0}|^2 + |\mathcal{M}_{\overline{D^0}}|^2} dDP}{\int dDP} \quad (3.15)$$

Calculating \mathcal{A}_{CP} - The Classic Method

This process for calculating the central value and errors on \mathcal{A}_{CP} are is what has been done before[18] and is very similar to that of the fit fractions. In this case, we have two covariance matrices: one for the fit to the D^0 sample, the other for the fit to the $\overline{D^0}$ data. As with the fit fractions, we use the covariance matrices to wiggle the

parameters. For each trial, we calculate a value of \mathcal{A}_{CP} as above. After 10,000 trials, we take the distribution and calculate the median and the lower and upper errors.

Calculating \mathcal{A}_{CP} - The New Method

Up to now, we have been writing the total matrix element written as a sum of amplitudes, phases and partial matrix elements. To make this easier to manipulate, let's simply replace the real amplitude and phase by a single complex amplitude \mathcal{B} :

$$\begin{aligned}
\mathcal{M}_{D^0 \rightarrow \pi^- \pi^+ \pi^0} &= \mathcal{A}_{non\ res} \cdot e^{i \phi_{non\ res}} + \\
&\mathcal{A}_{\rho^+ \pi^-} \cdot e^{i \phi_{\rho^+ \pi^-}} \cdot \mathcal{M}_{D^0 \rightarrow \rho^+ \pi^-} + \\
&\mathcal{A}_{\rho^- \pi^+} \cdot e^{i \phi_{\rho^- \pi^+}} \cdot \mathcal{M}_{D^0 \rightarrow \rho^- \pi^+} + \dots \\
&= \mathcal{B}_{non\ res} + \\
&\mathcal{B}_{\rho^+ \pi^-} \cdot \mathcal{M}_{D^0 \rightarrow \rho^+ \pi^-} + \\
&\mathcal{B}_{\rho^- \pi^+} \cdot \mathcal{M}_{D^0 \rightarrow \rho^- \pi^+} + \dots
\end{aligned}$$

Let's use \mathcal{B} to represent the coefficients for $D^0 \rightarrow \pi^- \pi^+ \pi^0$ and $\overline{\mathcal{B}}$ for $\overline{D^0} \rightarrow \pi^+ \pi^- \pi^0$. So now we have:

$$\begin{aligned}
\mathcal{M}_{D^0 \rightarrow \pi^- \pi^+ \pi^0} &= \mathcal{B}_{non\ res} + \\
&\mathcal{B}_{\rho^+ \pi^-} \cdot \mathcal{M}_{D^0 \rightarrow \rho^+ \pi^-} + \\
&\mathcal{B}_{\rho^- \pi^+} \cdot \mathcal{M}_{D^0 \rightarrow \rho^- \pi^+} + \dots
\end{aligned}$$

and

$$\begin{aligned}
\mathcal{M}_{\overline{D^0} \rightarrow \pi^- \pi^+ \pi^0} &= \overline{\mathcal{B}}_{non\ res} + \\
&\overline{\mathcal{B}}_{\rho^+ \pi^-} \cdot \mathcal{M}_{D^0 \rightarrow \rho^+ \pi^-} + \\
&\overline{\mathcal{B}}_{\rho^- \pi^+} \cdot \mathcal{M}_{D^0 \rightarrow \rho^- \pi^+} + \dots
\end{aligned}$$

If there is no CP violation, then all of the \mathcal{B} s should be the same as all of the $\overline{\mathcal{B}}$ s. To search for CP violation it makes sense to split each \mathcal{B} into a CP conserving piece \mathcal{C} and a CP violating piece \mathcal{V} :

$$\mathcal{B} = \mathcal{C} + \mathcal{V}$$

and

$$\overline{\mathcal{B}} = \mathcal{C} - \mathcal{V}.$$

We now have:

$$\begin{aligned} \mathcal{M}_{D^0 \rightarrow \pi^- \pi^+ \pi^0} &= (\mathcal{C}_{non\ res} + \mathcal{V}_{non\ res}) + \\ &\quad (\mathcal{C}_{\rho^+ \pi^-} + \mathcal{V}_{\rho^+ \pi^-}) \cdot \mathcal{M}_{D^0 \rightarrow \rho^+ \pi^-} + \\ &\quad (\mathcal{C}_{\rho^- \pi^+} + \mathcal{V}_{\rho^- \pi^+}) \cdot \mathcal{M}_{D^0 \rightarrow \rho^- \pi^+} + \dots \end{aligned}$$

and

$$\begin{aligned} \mathcal{M}_{\overline{D}^0 \rightarrow \pi^- \pi^+ \pi^0} &= (\mathcal{C}_{non\ res} - \mathcal{V}_{non\ res}) + \\ &\quad (\mathcal{C}_{\rho^+ \pi^-} - \mathcal{V}_{\rho^+ \pi^-}) \cdot \mathcal{M}_{D^0 \rightarrow \rho^+ \pi^-} + \\ &\quad (\mathcal{C}_{\rho^- \pi^+} - \mathcal{V}_{\rho^- \pi^+}) \cdot \mathcal{M}_{D^0 \rightarrow \rho^- \pi^+} + \dots \end{aligned}$$

It is important to note that up to this point, we haven't done anything really differently. Any matrix element we could represent with the old parameterization, we can equally well represent with the new.

With this new parameterization, we fit the D^0 and \overline{D}^0 data samples simultaneously. We can now calculate \mathcal{A}_{CP} the same way as above (generating 10,000 samples of the fit parameters and calculating \mathcal{A}_{CP} for each sample of parameters), except now we are using a single covariance matrix instead of two matrices. We can also extract information about CP violation for each resonance.

One last note on the new \mathcal{A}_{CP} parameterization. When using the Dalitz fitter, we will be using explicit phases and amplitudes again. When using this new parameterization, we will be talking about the CP conserving (or just conserving for short) amplitudes and phases and the CP violating (or just violating) amplitudes and phases.

3.5 Efficiency

To measure the shape of the efficiency over the Dalitz plot, we generated flat (over the Dalitz Plot) signal Monte Carlo with no lifetime⁶. The sample consists of over 115,000 events each of D^0 and $\overline{D^0}$ signal decays, luminosity weighted over all of CLEO II.V datasets ($4sH$ to $4sT$). We used the same analysis code and event selection to analyze this Monte Carlo sample as it was used in real data. We placed successfully reconstructed events on the Dalitz Plot using their generated x and y values ($m_{\pi^-\pi^+}^2$ and $m_{\pi^+\pi^0}^2$ respectively). The Dalitz fitter was used to fit this sample to a simple two-dimensional cubic polynomial $E_0 + E_x x + E_y y + E_{xx} x^2 + E_{xy} xy + E_{yy} y^2 + E_{xxx} x^3 + E_{xxy} x^2 y + E_{xyy} xy^2 + E_{yyy} y^3$. The values are shown in Table 3.3. The MC distribution, the fit, and projections can be seen in Figure 3.16.

Due to the normalization term in the signal piece of equation 3.13, multiplying all of the coefficients by a common factor does not affect the results. We have decided to normalize the efficiency such that if we integrate the efficiency over the Dalitz Plot and normalize that integral by the area of the Dalitz Plot, we will get the average efficiency (3.68%).

Coefficient	Value (10^{-3})
E_0	30.7 (fixed)
E_x	-4.7 ± 4.0
E_y	-14.5 ± 3.4
E_{xx}	6.3 ± 2.1
E_{xy}	22.6 ± 2.9
E_{yy}	7.9 ± 2.1
E_{xxx}	-2.1 ± 0.4
E_{xxy}	-5.2 ± 0.8
E_{xyy}	-6.2 ± 0.8
E_{yyy}	-1.3 ± 0.4

Table 3.3: The efficiency parameters found from the fitting technique described in the text.

⁶MC with no lifetime means that all of the D^0 daughters decayed very close to where the D^0 was created. This works well to describe all D^0 resonances *except* $D^0 \rightarrow K_s^0 \pi^0$.

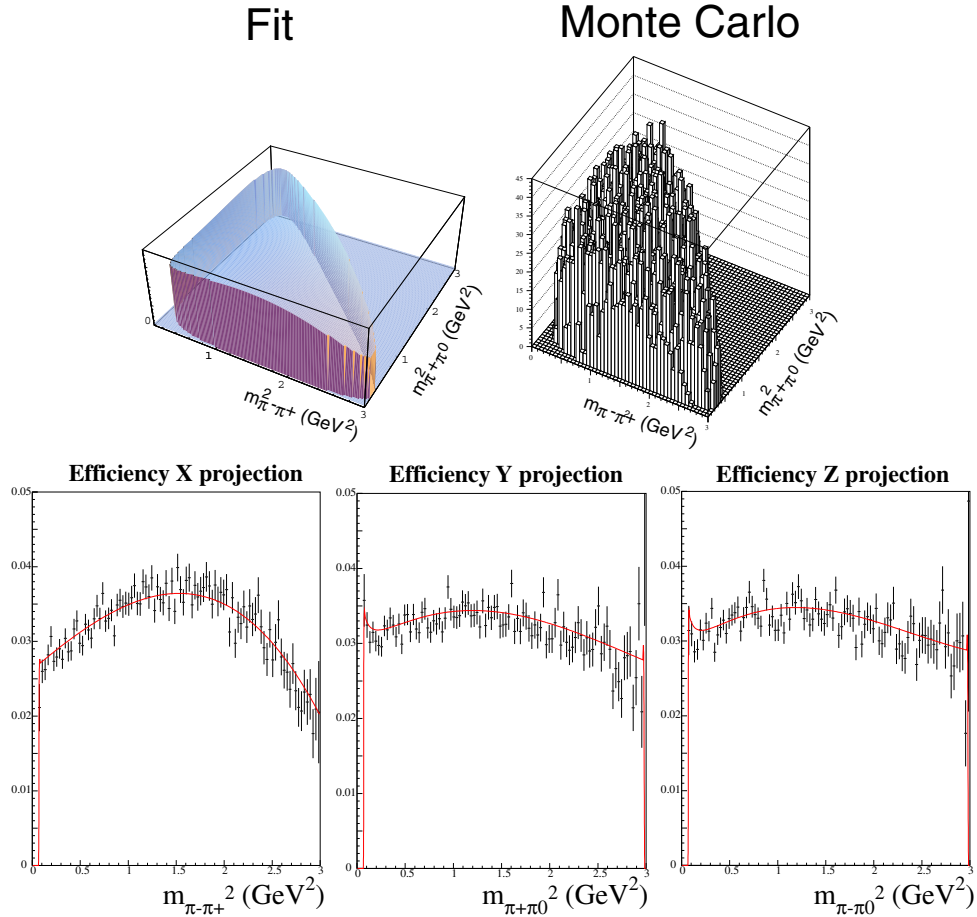


Figure 3.16: The best efficiency function and the Monte Carlo to which it was fit. For the projections, the red line is the fit and the black histogram is the MC. Note: The efficiency for each bin is normalized by the height of that bin.

3.6 Background

There are two questions that need to be answered about the background. First, how do we parameterize it? Second, what data sample do we use to find it?

The first question is much simpler. We again use a two-dimensional cubic polynomial (as used in the efficiency parameterization), but we also add four terms for background ρ s and K_S^0 s. Since we do not have a signal piece representing the K_S^0 , we let the background K_S^0 piece ($B_{K_{Short}^0}$) float in the fit. See Section 3.2.2 for more

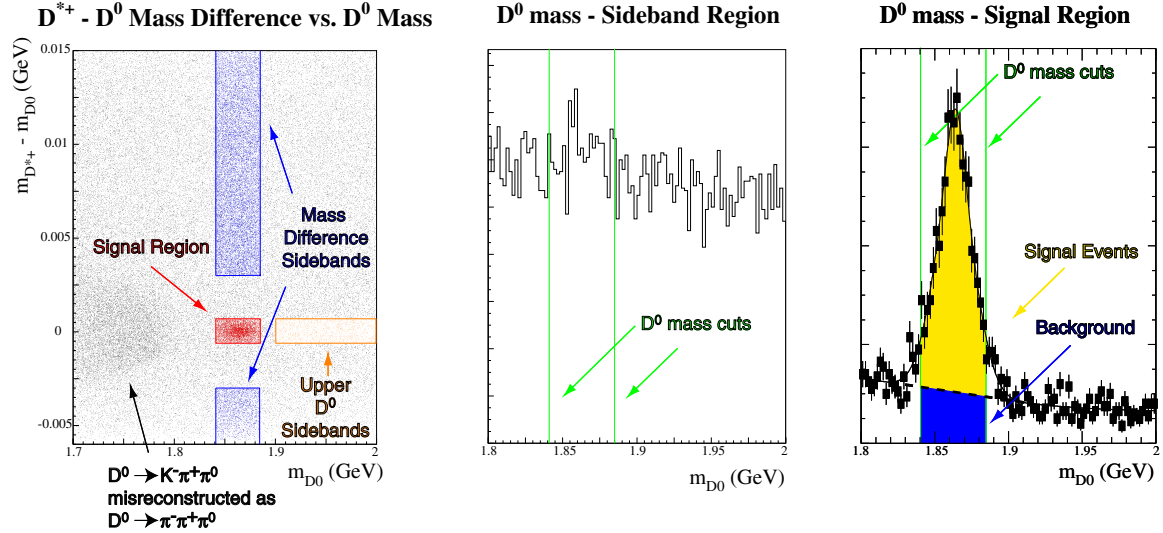


Figure 3.17: We use both the upper and lower mass difference sideband as well as the upper D^0 mass sideband. The middle and right plots show the projections onto the D^0 mass axis for the mass difference sideband and the signal region respectively. **Note:** The mass difference is centered at the PDG value.

details on the K_S^0 .

The second question is more complicated. What we would like to do is understand the shape of on the Dalitz plot of the background that is in the signal region. In Monte Carlo, we can do just that. We can look at events that pass all of our cuts, but are not signal. In data, the matter is more complicated. For any given event that passes all of our cuts, we have no way of knowing whether it is a signal event or a background event. The best that we can do is look at sidebands. A sideband is a place in cut space that is close to the signal region, but is far enough away that it has very few signal events in it. An example of a sideband is the upper mass difference sideband where our D^0 candidate has the right mass but our D^{*+} candidate's mass (and therefore, its mass difference) is too high. The hope is that the background under the signal region will be very similar to the events found in whatever sideband we choose.

There are a few possible choices of sidebands (see Figure 3.17). There are the upper and lower mass difference sidebands and the upper and lower D^0 sidebands. We do not

want to use the lower D^0 sidebands because it is dominated by $D^0 \rightarrow K^- \pi^+ \pi^0$ events being mis-reconstructed as $D^0 \rightarrow \pi^- \pi^+ \pi^0$ (see Figure 3.17). The choice is therefore between the mass difference sideband⁷ and the upper D^0 sideband⁸.

In order to decide which sideband to use, we need to know how well a background parameterization fit on one of the sidebands represents the background in the signal region. To accomplish this, we studied generic Monte Carlo. We ran our analysis code on all of the $b\bar{b}$ and continuum Monte Carlo staged on disk at the Cornell Analysis Farm. We then looked at three distinct samples: the background events in signal region (1115 events)⁹, all events in the mass difference sidebands (8507 events) and all events in the upper D^0 sideband (1621 events). We fit all three regions with the background parameterization mentioned above.

The goal of this exercise is to decide to which sideband we should fit our parameterization in order to get the best representation of the background. To achieve this, we compared the two sideband fits to the MC sample in the signal region.¹⁰ The results are shown in Table 3.4 below.

Resonances	$\frac{\text{likelihood}}{\text{event}}$	χ^2
Signal Region	2.83	69.9
Upper D^0 Sideband	2.89	120.4
Mass Difference Sideband	2.90	136.8

Table 3.4:

The comparisons between the fits of the two different sideband regions and the background in the signal region from generic Monte Carlo. For a point of reference, we also include the comparison between the fit to the signal region and the signal region sample as well. All χ^2 fits were done with 44 bins.

⁷We measure the mass difference from the nominal PDG $m_{D^{*+}} - m_{D^0}$ value. The upper sideband is defined as 3 to 15 MeV above this value; the lower sideband is 3 to 6 MeV below.

⁸ $1.9 GeV < m_{D^0} < 2.0 GeV$

⁹Since this is MC, we can make sure that the events we are looking at are *not* signal events.

¹⁰We do not care how well the different sidebands estimate the number of K_S^0 's since this floats in the fit. To minimize the difference between fits, we refit each parameterization to the signal region, letting *only* the K_S^0 component float.

A priori, we would have guessed that the mass difference side bands are better to use for two reasons. First, the mass difference sidebands are larger and therefore have more data to fit to. Second, in terms of the Dalitz Plot variables, the use of the mass difference sideband is consistent while the D^0 sideband is not.

To see what we mean by this, we begin by taking equation 3.1 and replacing $m_{\pi^-\pi^+}^2$, $m_{\pi^+\pi^0}^2$, and $m_{\pi^-\pi^0}^2$ by x , y , and z respectively. We get:

$$m_{D^0}^2 + m_{\pi^-}^2 + m_{\pi^+}^2 + m_{\pi^0}^2 = x + y + z \quad (3.16)$$

Instead of having the data centered around the D^0 mass, when we use a D^0 sideband to look at the background, equation 3.16 is no longer true and will not give us an accurate measurement of the contribution from the diagonal ρ^- s. This can be corrected for but is nonetheless an unpleasant complication.

For these two reasons, we have decided to use the mass difference side bands to fit the background parameterization even though the MC studies suggest the upper D^0 sideband may be a slightly better choice. We will repeat all of the fits with the D^0 sideband and report any differences as part of our systematic error.

In all cases, the background parameterizations were fit to their respective samples by using the unbinned maximum likelihood Dalitz fitter. As with the efficiency, there is an overall ambiguity due to the normalization in equation 3.13. The first coefficient is therefore fixed to be 1 for convenience. The values are found in Table 3.5. The fit and data can be seen in Figure 3.18.

3.7 Signal Fraction

Signal fraction is the percent of signal events that we believe we have in our data sample (see Figure 3.19). The method for measuring signal fraction is relatively straightforward. We start by looking at the D^0 mass distribution in data with all event selection criteria applied except the D^0 mass cuts. We then fit this distribution

Coefficient	Value
B_0	1.0 (fixed)
B_x	1.7 ± 0.7
B_y	0.2 ± 0.5
B_{xx}	-1.2 ± 0.5
B_{xy}	-2.3 ± 0.7
B_{yy}	0.1 ± 0.4
B_{xxx}	0.3 ± 0.1
B_{xxy}	0.8 ± 0.2
B_{xyy}	0.4 ± 0.2
B_{yyy}	-0.1 ± 0.1
B_{ρ^+}	0.0027 ± 0.0010
B_{ρ^-}	0.0038 ± 0.0014
B_{ρ^0}	0.0019 ± 0.0009
$B_{K_{Short}}$	Floats in fit

Table 3.5: The background parameters.

with one function representing the background events and another function for the signal events. By integrating the two fit functions between the D^0 mass cut limits, we get our estimation of numbers of signal and background events (see the upper plot in Figure 3.19) and a signal fraction of $(78 \pm 3)\%$.

There is no reason, however, why we couldn't use the same method on the $D^{*+} - D^0$ mass difference distribution (see the lower plot in Figure 3.19). The problem is that the two methods do not agree very well; the $D^{*+} - D^0$ mass difference distribution gives us a signal fraction of $(85 \pm 3)\%$. Further study demonstrated that fitting the $D^{*+} - D^0$ mass difference distribution consistently yields a higher signal fraction than the D^0 mass distribution. To resolve this problem, we looked at samples of generic MC where we can not only use the above method on the two distributions, but the "true" answer as well. In the Monte Carlo studies, the true answer consistently fell between the values from the two distributions. The fit fraction that we use, therefore, is the average of the two values, while the error is simply half of the difference between them $(81.4\% \pm 3.6\%)$. The effect of this error is studied further as a systematic error.

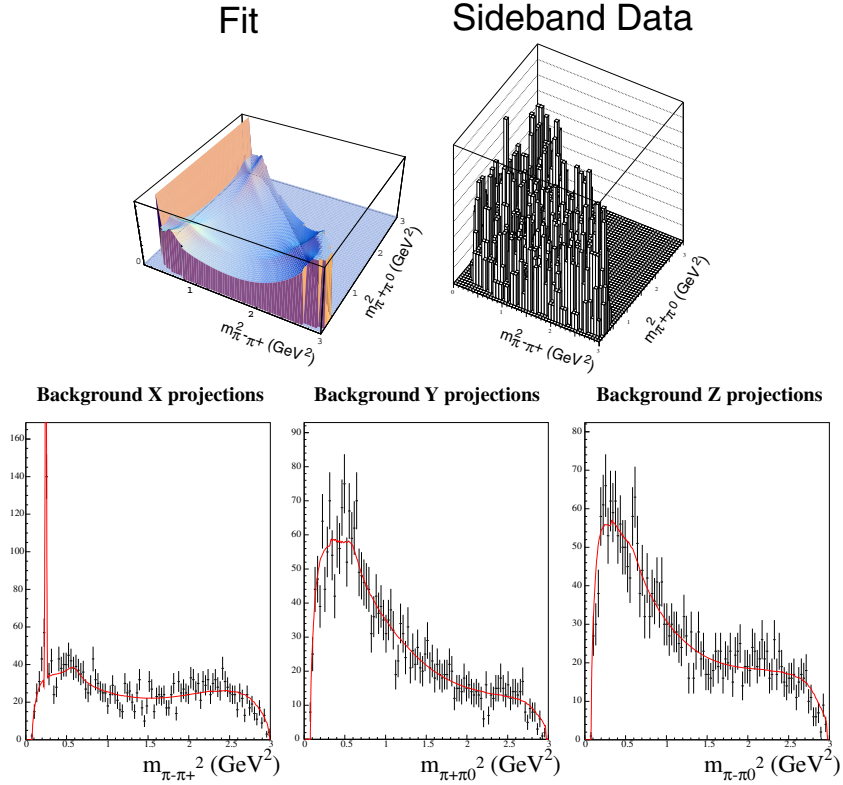


Figure 3.18: The background fit and the sideband data it was fit to. For the projections, the red line is the fit and the black histogram is the data.

3.8 Results

Everything presented here used the full CLEO II.V dataset (i.e. datasets $4sH$ to $4sT$). All numeric results are presented in the following order: first **the results for the D^0 sample**, then **the results for the $\overline{D^0}$ sample**, and finally **the results for the combined sample**. All quoted errors are statistical errors only.

Key
$D^0 \rightarrow \pi^-\pi^+\pi^0$ only
$\overline{D^0} \rightarrow \pi^+\pi^-\pi^0$ only
Both D^0 and $\overline{D^0} \rightarrow \pi\pi\pi^0$

To compare the quality of the different fits, we look at the final likelihood for each fit (see Table 3.6). For the purposes of illustration, we have included another example

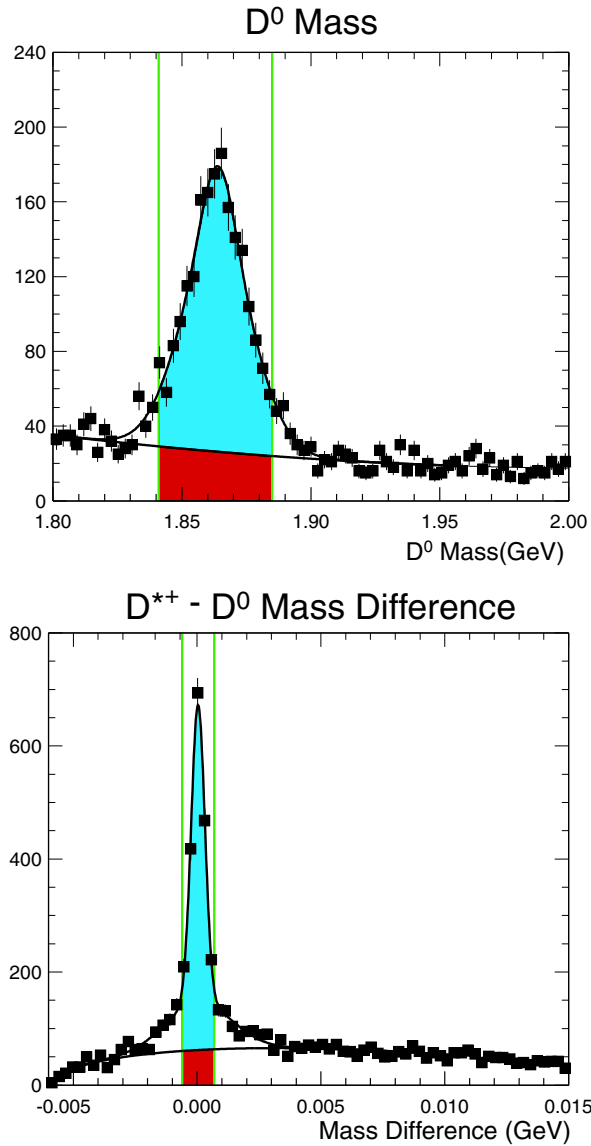


Figure 3.19: The distributions for the D^0 mass and the $D^{*+} - D^0$ mass difference (centered at the PDG value). These two plots were made with all cuts except the D^0 mass cuts for the upper and mass difference cuts in the lower. The green lines are the upper and lower cuts. In both plots, the area of the upper blue region is our estimation of signal events while the red area represents background events.

fit: with just the ρ^+ , ρ^- , and the non resonant term (we deliberately left out the ρ^0 resonance to show what a “bad” representation looks like).

The best results are with the three light ρ 's and a non-resonant term (see Table 3.7). Since all three light ρ 's play a significant part, we also tried adding the heavier ρ 's in groups of three to our fits. Table 3.8 illustrates the fits using the light ρ 's and ρ_{1450} 's. Table 3.9 is the results of the fits using the light ρ 's and ρ_{1700} 's.

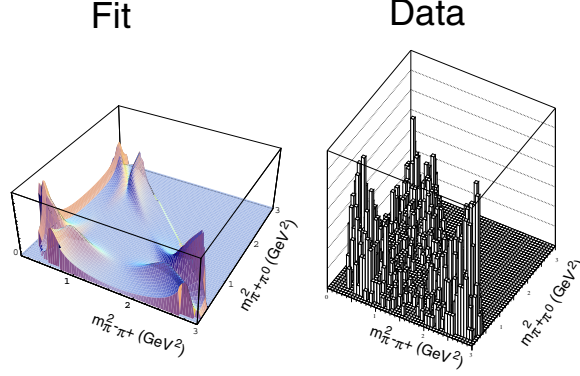
We also tried adding the $\sigma(500)$ (Table 3.10) and the $f_0(980)$ (Table 3.11).

Finally, we show the results for the intentionally bad fit. See Table 3.12 for the fit with ρ^+ and ρ^- .

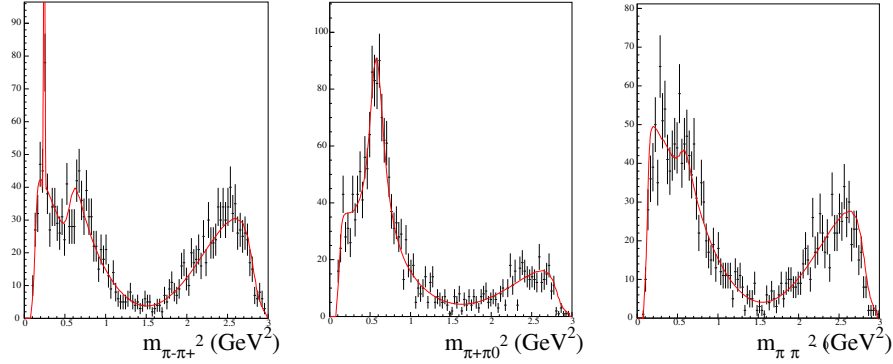
In all cases, adding the other resonances did not result in an improvement of the fit in any significant way. The fits did not get significantly better and none of the additional resonances had a significant fit fraction. For this reason, the final answer will quote only fits with the three light ρ s and the non-resonance piece.

Resonances	<i>likelihood</i>	$\frac{\textit{likelihood}}{\textit{event}}$	χ^2	$\chi^2/\text{d.o.f.}$
ρ^+ , ρ^- , and non res only (bad)	4359.5	2.28	295.0	5.00
ρ^+ , ρ^- , ρ^0 , and non res	3873.4	2.02	81.4	1.43
light ρ 's , non res, and ρ_{1450} 's	3861.0	2.02	78.6	1.54
light ρ 's , non res, and ρ_{1700} 's	3855.4	2.01	69.9	1.37
light ρ 's , non res, and $\sigma(500)$	3868.2	2.02	80.7	1.65
light ρ 's , non res, and $f_0(980)$	3871.2	2.02	84.5	1.54

Table 3.6: Likelihood and χ^2 for all of the fits presented. All χ^2 calculations are with 64 bins. Please note that the first fit (ρ^+ , ρ^- , and non res only) is presented for illustrative purposes only.



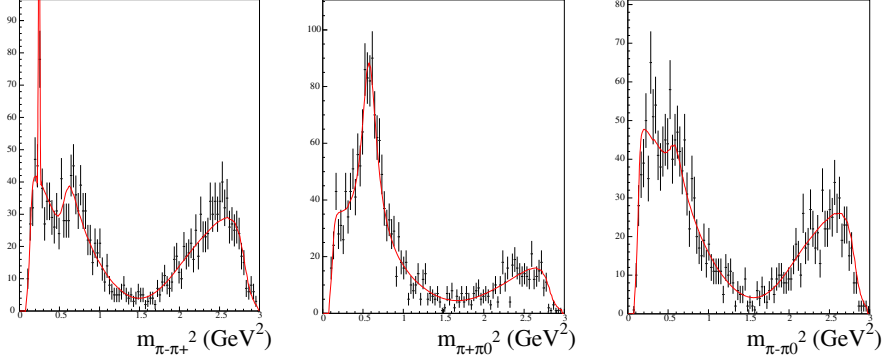
$D^0 \rightarrow \pi^- \pi^+ \pi^0$ Data - X projections $D^0 \rightarrow \pi^- \pi^+ \pi^0$ Data - Y projections $D^0 \rightarrow \pi^- \pi^+ \pi^0$ Data - Z projections



Resonance	Amplitude	Phase($^\circ$)	Fit Fraction(%)
ρ^+	1.0 (fixed)	0.0 (fixed)	76.6 ± 2.5
			76.0 ± 2.7
			76.5 ± 1.8
ρ^0	0.57 ± 0.03	10 ± 4	24.9 ± 2.4
	0.55 ± 0.04	9 ± 4	22.5 ± 2.7
	0.56 ± 0.02	10 ± 3	23.9 ± 1.8
ρ^-	0.64 ± 0.03	176 ± 4	31.0 ± 2.8
	0.67 ± 0.04	177 ± 4	34.0 ± 3.0
	0.65 ± 0.03	176 ± 3	32.3 ± 2.1
<i>non res.</i>	1.03 ± 0.24	72 ± 11	2.8 ± 1.4
	1.03 ± 0.24	84 ± 11	2.7 ± 1.4
	1.03 ± 0.17	77 ± 8	2.7 ± 0.9

Table 3.7: Shown are the results using all of the data (i.e. both D^0 and $\overline{D^0}$) fitting with the three light ρ s and a non-resonance term only. The data is represented by the black points with errors while the fit is the solid red line. The results are presented in the order as the D^0 sample, the $\overline{D^0}$ sample, and the combined D^0 and $\overline{D^0}$ sample. The errors quoted are statistical only.

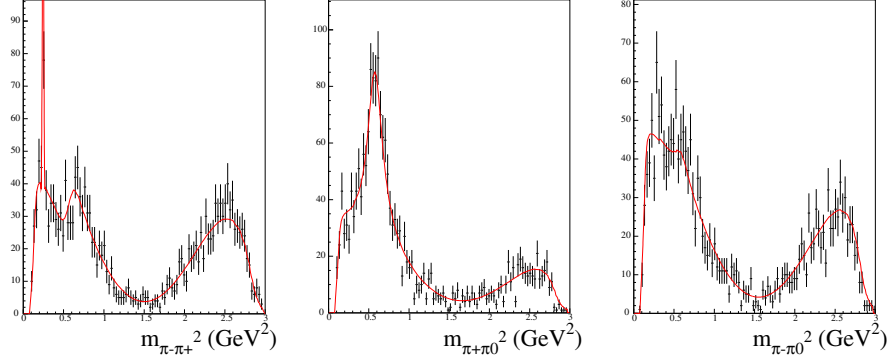
$D^0 \rightarrow \pi^- \pi^+ \pi^0$ Data - X projections $D^0 \rightarrow \pi^- \pi^+ \pi^0$ Data - Y projections $D^0 \rightarrow \pi^- \pi^+ \pi^0$ Data - Z projections



Resonance	Amplitude	Phase($^\circ$)	Fit Fraction(%)
ρ^+	1.0 (fixed)	0.0 (fixed)	71.3 ± 3.9
			73.7 ± 4.0
			72.5 ± 2.8
ρ^0	0.59 ± 0.04	12 ± 5	24.7 ± 2.9
	0.54 ± 0.05	13 ± 5	21.9 ± 3.3
	0.57 ± 0.03	12 ± 3	23.6 ± 2.2
ρ^-	0.70 ± 0.05	177 ± 4	35.1 ± 3.8
	0.68 ± 0.05	180 ± 4	34.4 ± 4.2
	0.69 ± 0.04	178 ± 3	35.0 ± 3.0
<i>non res.</i>	0.89 ± 0.24	73 ± 13	1.9 ± 1.1
	0.98 ± 0.25	86 ± 13	2.4 ± 1.3
	0.92 ± 0.18	80 ± 9	2.1 ± 0.8
ρ_{1450}^0	0.55 ± 0.31	-31 ± 28	0.0 ± 1.2
	0.34 ± 0.31	-45 ± 47	0.0 ± 0.7
	0.47 ± 0.22	-38 ± 24	0.0 ± 0.8
ρ_{1450}^+	0.26 ± 0.30	23 ± 81	0.0 ± 0.6
	0.28 ± 0.33	199 ± 80	0.0 ± 0.7
	0.04 ± 0.23	-6 ± 402	0.0 ± 0.2
ρ_{1450}^-	0.77 ± 0.28	104 ± 25	1.0 ± 1.3
	0.43 ± 0.32	112 ± 41	0.0 ± 1.0
	0.65 ± 0.22	107 ± 21	0.8 ± 0.8

Table 3.8: Shown are the results using all of the data fitting with the three light ρ s, a non-resonance term, and ρ_{1450} 's. The results are presented in the order as the D^0 sample, the $\overline{D^0}$ sample, and the combined D^0 and $\overline{D^0}$ sample. As can be seen, there are not any significant differences between these three plot projections and those in Table 3.7. The errors quoted are statistical only.

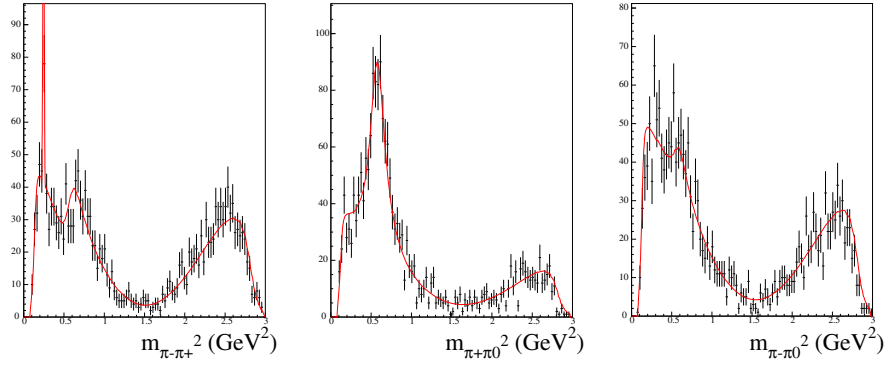
$D^0 \rightarrow \pi^- \pi^+ \pi^0$ Data - X projections $D^0 \rightarrow \pi^- \pi^+ \pi^0$ Data - Y projections $D^0 \rightarrow \pi^- \pi^+ \pi^0$ Data - Z projections



Resonance	Amplitude	Phase($^\circ$)	Fit Fraction(%)
ρ^+	1.0 (fixed)	0.0 (fixed)	79.3 ± 4.0
			72.0 ± 5.2
			76.8 ± 3.0
ρ^0	0.54 ± 0.04	12 ± 4	22.8 ± 3.2
	0.57 ± 0.05	12 ± 5	23.8 ± 3.8
	0.55 ± 0.03	12 ± 3	23.2 ± 2.5
ρ^-	0.62 ± 0.05	178 ± 4	30.6 ± 4.0
	0.72 ± 0.07	179 ± 4	37.2 ± 5.4
	0.66 ± 0.04	178 ± 3	33.0 ± 3.1
<i>non res.</i>	0.99 ± 0.23	76 ± 11	2.7 ± 1.2
	0.86 ± 0.30	90 ± 14	1.4 ± 1.7
	0.97 ± 0.17	82 ± 8	2.5 ± 0.8
ρ_{1700}^0	1.92 ± 0.90	18 ± 26	0.0 ± 2.1
	2.71 ± 0.90	13 ± 19	2.1 ± 2.1
	2.18 ± 0.62	12 ± 16	1.7 ± 1.1
ρ_{1700}^+	1.50 ± 0.77	-23 ± 35	0.0 ± 1.3
	2.02 ± 1.34	44 ± 29	0.0 ± 2.6
	1.32 ± 0.60	2 ± 30	0.0 ± 0.9
ρ_{1700}^-	2.00 ± 0.78	189 ± 26	0.7 ± 1.7
	2.37 ± 0.80	178 ± 29	1.5 ± 1.6
	2.13 ± 0.56	185 ± 18	1.6 ± 0.9

Table 3.9: Shown are the results using all of the data fitting with the three light ρ s, a non-resonance term, and ρ_{1700} 's. The results are presented in the order as the D^0 sample, the $\overline{D^0}$ sample, and the combined D^0 and $\overline{D^0}$ sample. As can be seen, there are not any significant differences between these three plot projections and those in Table 3.7. The errors quoted are statistical only.

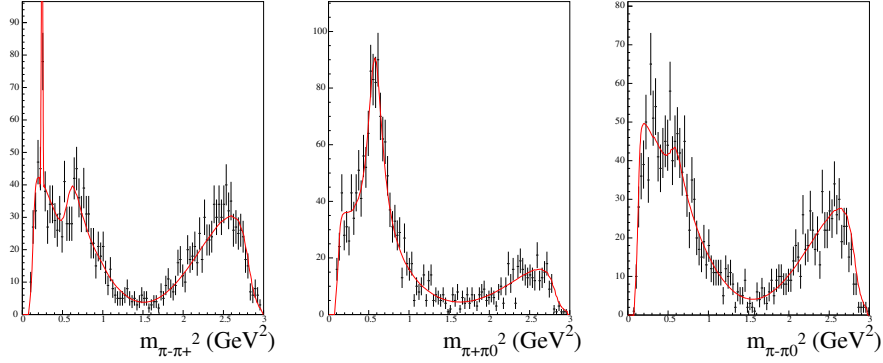
$D^0 \rightarrow \pi^- \pi^+ \pi^0$ Data - X projections $D^0 \rightarrow \pi^- \pi^+ \pi^0$ Data - Y projections $D^0 \rightarrow \pi^- \pi^+ \pi^0$ Data - Z projections



Resonance	Amplitude	Phase($^\circ$)	Fit Fraction(%)
ρ^+	1.0 (fixed)	0.0 (fixed)	77.8 ± 2.4
			76.2 ± 3.0
			77.4 ± 1.8
ρ^0	0.57 ± 0.03	9 ± 4	25.0 ± 2.5
	0.54 ± 0.04	10 ± 4	21.9 ± 2.7
	0.56 ± 0.02	9 ± 3	23.7 ± 1.9
ρ^-	0.61 ± 0.04	173 ± 4	28.8 ± 2.9
	0.67 ± 0.04	178 ± 5	34.4 ± 3.3
	0.64 ± 0.03	175 ± 3	31.1 ± 2.2
$\sigma(500)$	0.23 ± 0.09	26 ± 22	0.3 ± 1.4
	0.19 ± 0.10	-75 ± 60	0.0 ± 1.1
	0.16 ± 0.07	-5 ± 24	0.0 ± 0.8
<i>non res.</i>	1.10 ± 0.26	49 ± 15	3.4 ± 1.6
	0.78 ± 0.28	96 ± 31	0.8 ± 1.7
	0.92 ± 0.20	64 ± 12	2.3 ± 1.0

Table 3.10: Shown are the results using all of the data fitting with the three light ρ s, a non-resonance term, and the $\sigma(500)$. The results are presented in the order as the D^0 sample, the $\overline{D^0}$ sample, and the combined D^0 and $\overline{D^0}$ sample. As can be seen, there are not any significant differences between these three plot projections and those in Table 3.7. The errors quoted are statistical only.

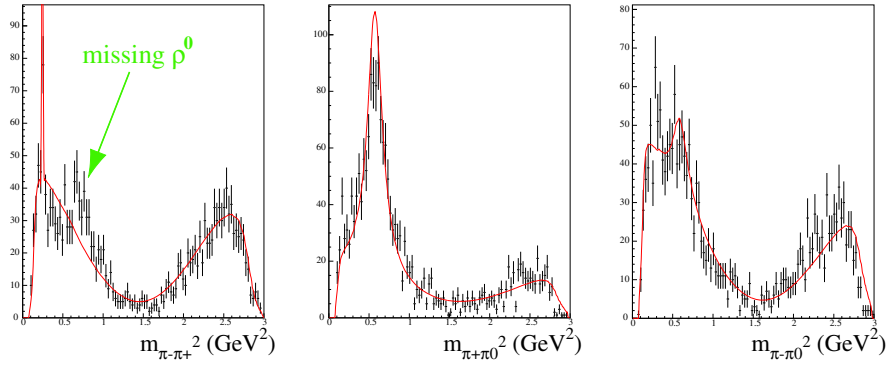
$D^0 \rightarrow \pi^- \pi^+ \pi^0$ Data - X projections $D^0 \rightarrow \pi^- \pi^+ \pi^0$ Data - Y projections $D^0 \rightarrow \pi^- \pi^+ \pi^0$ Data - Z projections



Resonance	Amplitude	Phase($^\circ$)	Fit Fraction($\%$)
ρ^+	1.0 (fixed)	0.0 (fixed)	77.0 ± 2.4
			76.6 ± 2.6
			77.0 ± 1.8
ρ^0	0.57 ± 0.03	11 ± 4	24.6 ± 2.5
	0.55 ± 0.04	9 ± 4	23.0 ± 2.7
	0.56 ± 0.02	10 ± 3	24.0 ± 1.9
ρ^-	0.63 ± 0.03	178 ± 4	30.3 ± 2.8
	0.66 ± 0.04	178 ± 4	32.8 ± 3.1
	0.64 ± 0.03	178 ± 3	31.5 ± 2.1
$f_0(980)$	0.08 ± 0.04	31 ± 39	0.0 ± 0.6
	0.10 ± 0.05	-69 ± 31	0.0 ± 0.8
	0.06 ± 0.03	-26 ± 33	0.0 ± 0.3
<i>non res.</i>	0.97 ± 0.25	70 ± 12	2.6 ± 1.4
	0.84 ± 0.26	93 ± 15	1.5 ± 1.5
	0.91 ± 0.18	80 ± 9	2.2 ± 0.9

Table 3.11: Shown are the results using all of the data fitting with the three light ρ s, a non-resonance term, and the $f_0(980)$. The results are presented in the order as the D^0 sample, the $\overline{D^0}$ sample, and the combined D^0 and $\overline{D^0}$ sample. As can be seen, there are not any significant differences between these three plot projections and those in Table 3.7. The errors quoted are statistical only.

$D^0 \rightarrow \pi^- \pi^+ \pi^0$ Data - X projections $D^0 \rightarrow \pi^- \pi^+ \pi^0$ Data - Y projections $D^0 \rightarrow \pi^- \pi^+ \pi^0$ Data - Z projections



Resonance	Amplitude	Phase($^\circ$)	Fit Fraction($\%$)
ρ^+	1.0 (fixed)	0.0 (fixed)	77.9 ± 2.2
			78.7 ± 2.2
			78.5 ± 1.6
ρ^-	0.58 ± 0.03	185 ± 5	26.0 ± 2.9
			28.2 ± 3.0
			27.1 ± 2.1
<i>non res.</i>	1.89 ± 0.24	84 ± 7	9.4 ± 2.3
			7.1 ± 2.0
			8.2 ± 1.5

Table 3.12: Shown are the results using all of the data fitting with the ρ^+ , ρ^- , and a non-resonance term. As can be seen in the x projection (see arrow), this set of resonances does not do as well, either in terms of the projections or in terms of the goodness of fit. The results are presented in the order as the D^0 sample, the $\overline{D^0}$ sample, and the combined D^0 and $\overline{D^0}$ sample. The errors quoted are statistical only.

3.8.1 \mathcal{A}_{CP}

Using the standard parameterization, we calculated \mathcal{A}_{CP} of $0.0097_{-0.0706}^{+0.0905}$ with a 90% confidence level of $-0.115 < \mathcal{A}_{CP} < 0.134$. With the new parameterization we found \mathcal{A}_{CP} of $0.0024_{-0.0592}^{+0.0584}$ with a 90% confidence level of $-0.1015 < \mathcal{A}_{CP} < 0.1026$. See Figure 3.20 for both distributions.

Resonance	Conserving Amplitude	ConservingPhase($^{\circ}$)	Violating Amplitude
ρ^+	1.0 (fixed)	0.0 (fixed)	0.04 ± 0.21
ρ^0	0.56 ± 0.02	9.7 ± 2.8	0.03 ± 0.19
ρ^-	0.65 ± 0.03	176.4 ± 2.8	0.03 ± 0.11
<i>non res.</i>	1.03 ± 0.17	78.1 ± 8.2	0.07 ± 0.18

Table 3.13: Shown are the results of the fit using the CP conserving-violating parameterization. In principle, each resonance should have both a CP conserving and CP violating phase and amplitude. Since the error on each CP violating amplitude is much bigger than its value, the phase is completely unknown and not reported.

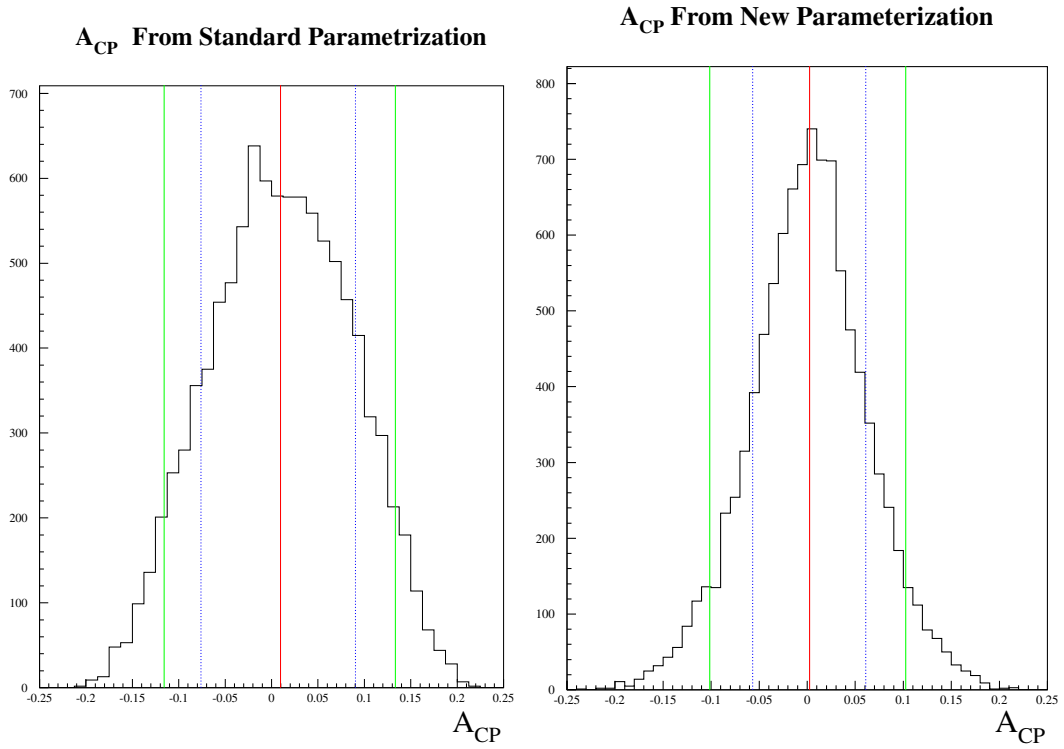


Figure 3.20: The standard parameterization is presented on the left, the new on the right. In both plots, the solid red line in the center is the median value. The dashed blue lines are at $\pm 1\sigma$ and The solid green lines are 90% limit.

3.9 Systematic Errors

No analysis can be complete without a discussion of systematic errors. In particular, we are going to be discussing the systematic errors associated with the efficiency and background measurements and those due to event selection criteria as well as the fit fraction measurement.

3.9.1 General Method

Regardless of the type of systematic errors, the method for calculating them is very similar. In all cases, we varied the parameters of concern and re-ran the Dalitz Fitter to assess how sensitive the final answers are to these parameters. Systematic errors will be quoted in three groups: the phase, amplitude, and fit fraction for the standard parameterization; the CP conserving phase and the CP conserving and violating phase for the new parameterization; and finally, the \mathcal{A}_{CP} numbers for both methods.

3.9.2 Efficiency

The efficiency was probably the most straight-forward systematic calculation to do. We took the covariance matrix from the fit of the efficiency parameterization and generated 400 samples of efficiency parameters. After having run the Dalitz Fitter with each set of efficiency parameters, we have distributions of all necessary phases, amplitudes and fit fractions. See Table 3.14 for the systematic errors due to efficiency parameterization.

3.9.3 Background

The background error was calculated exactly as above, except that there is a separate piece (to be added in quadrature) to assess the variance due to using the mass difference sidebands instead of the upper D^0 sideband. See Table 3.15 for the systematic

Resonance	Amplitude	Phase($^{\circ}$)	Fit Fraction(%)
ρ^+	fixed	fixed	± 0.5 ± 0.5 ± 0.5
ρ^0	± 0.004 ± 0.005 ± 0.004	± 0.3 ± 0.3 ± 0.3	± 0.27 ± 0.29 ± 0.28
ρ^-	± 0.007 ± 0.008 ± 0.007	± 0.4 ± 0.4 ± 0.4	± 0.5 ± 0.6 ± 0.5
<i>non res.</i>	± 0.02 ± 0.02 ± 0.02	± 1.4 ± 1.3 ± 1.3	± 0.11 ± 0.12 ± 0.12

Resonance	Conserving Amplitude	Conserving Phase($^{\circ}$)	Violating Amplitude
ρ^+	fixed	fixed	± 0.019
ρ^0	± 0.0043	± 0.3	± 0.010
ρ^-	± 0.007	± 0.4	± 0.014
<i>non res.</i>	± 0.023	± 1.3	± 0.014

	Standard Parameterization	New Parameterization
\mathcal{A}_{CP}	± 0.0006	± 0.04

Table 3.14: The systematic errors associated with the efficiency. The top table shows the errors on the standard parameterization, presented in the usual order (the D^0 sample, the \overline{D}^0 sample, and the combined D^0 and \overline{D}^0 sample). The middle table shows the errors on the new parameterization. The bottom table shows the errors on the \mathcal{A}_{CP} numbers.

errors due to background parameterization.

3.9.4 Signal Fraction

Using statistical error on the signal fraction as our range, we ran the Dalitz fitter at the minimum (77.8%) and maximum (85.0%) values and see the effects on the final answers. See Table 3.16 for the systematic errors due to errors in signal fraction calculation.

3.9.5 Event Selection

The general idea is very simple. For each cut made, we varied the cut by some sensible amount, re-ran the Dalitz Fitter, and saw how much varying the cuts affected the final answer. The only question was: How much is sensible? What we did was loosen (tighten) each cut until the data sample had the same minimum (maximum) fit fraction as in the Signal Fraction section above.

The variations in the cuts are shown in Table 3.17 and the associated systematic errors are shown in Table 3.18.

3.9.6 Total Systematic Errors

For the total systematic errors, the four types of systematic errors are added in quadrature. See Table 3.18 for the total systematic errors.

Resonance	Amplitude	Phase($^{\circ}$)	Fit Fraction(%)
ρ^+	fixed	fixed	$\pm 0.17 \pm 0.27 = \pm 0.32$ $\pm 0.14 \pm 0.26 = \pm 0.30$ $\pm 0.32 \pm 0.26 = \pm 0.42$
ρ^0	$\pm 0.001 \pm 0.003 = \pm 0.003$ $\pm 0.004 \pm 0.003 = \pm 0.005$ $\pm 0.005 \pm 0.003 = \pm 0.006$	$\pm 0.4 \pm 0.2 = \pm 0.5$ $\pm 0.4 \pm 0.2 = \pm 0.4$ $\pm 0.8 \pm 0.2 = \pm 0.8$	$\pm 0.17 \pm 0.18 = \pm 0.25$ $\pm 0.39 \pm 0.18 = \pm 0.43$ $\pm 0.53 \pm 0.18 = \pm 0.56$
ρ^-	$\pm 0.004 \pm 0.003 = \pm 0.006$ $\pm 0.005 \pm 0.004 = \pm 0.006$ $\pm 0.010 \pm 0.003 = \pm 0.011$	$\pm 0.6 \pm 0.2 = \pm 0.6$ $\pm 0.6 \pm 0.2 = \pm 0.6$ $\pm 1.1 \pm 0.2 = \pm 1.1$	$\pm 0.37 \pm 0.22 = \pm 0.43$ $\pm 0.48 \pm 0.28 = \pm 0.56$ $\pm 0.87 \pm 0.24 = \pm 0.90$
<i>non res.</i>	$\pm 0.001 \pm 0.021 = \pm 0.022$ $\pm 0.003 \pm 0.025 = \pm 0.025$ $\pm 0.001 \pm 0.023 = \pm 0.023$	$\pm 2.1 \pm 1.2 = \pm 2.4$ $\pm 2.8 \pm 1.2 = \pm 3.0$ $\pm 4.8 \pm 1.2 = \pm 4.9$	$\pm 0.01 \pm 0.11 = \pm 0.11$ $\pm 0.01 \pm 0.13 = \pm 0.13$ $\pm 0.00 \pm 0.12 = \pm 0.12$

Resonance	Conserving Amplitude	Conserving Phase($^{\circ}$)	Violating Amplitude
ρ^+	fixed	fixed	$\pm 0.009 \pm 0.020 = \pm 0.021$
ρ^0	$\pm 0.005 \pm 0.003 = \pm 0.006$	$\pm 0.85 \pm 0.18 = \pm 0.87$	$\pm 0.007 \pm 0.011 = \pm 0.013$
ρ^-	$\pm 0.010 \pm 0.003 = \pm 0.010$	$\pm 1.2 \pm 0.2 = \pm 1.2$	$\pm 0.004 \pm 0.013 = \pm 0.013$
<i>non res.</i>	$\pm 0.003 \pm 0.023 = \pm 0.023$	$\pm 4.9 \pm 1.2 = \pm 5.0$	$\pm 0.007 \pm 0.015 = \pm 0.017$

	Standard Parameterization	New Parameterization
\mathcal{A}_{CP}	$\pm 0.0007 \pm 0.0013 = \pm 0.0015$	$\pm 0.010 \pm 0.037 = \pm 0.038$

Table 3.15: The systematic errors associated with the background. In each place, the first number is the error associated with using the mass difference sideband instead of the D^0 sideband. The second error is due to the background parameterization. These two numbers are added in quadrature to form the third number. The top table shows the errors on the standard parameterization, presented in the usual order (the D^0 sample, the $\overline{D^0}$ sample, and the combined D^0 and $\overline{D^0}$ sample). The middle table shows the errors on the new parameterization. The bottom table presents the errors on the \mathcal{A}_{CP} numbers.

Resonance	Amplitude	Phase($^{\circ}$)	Fit Fraction(%)
ρ^+	fixed	fixed	± 0.4 ± 0.9 ± 0.4
ρ^0	± 0.014 ± 0.021 ± 0.004	± 0.6 ± 0.4 ± 0.2	± 1.3 ± 2.0 ± 0.5
ρ^-	± 0.0195 ± 0.0189 ± 0.0039	± 0.3 ± 0.5 ± 0.1	± 2.0 ± 1.9 ± 0.6
<i>non res.</i>	± 0.16 ± 0.18 ± 0.17	± 6.6 ± 7.5 ± 0.4	± 0.9 ± 1.0 ± 0.9

Resonance	Conserving Amplitude	Conserving Phase($^{\circ}$)	Violating Amplitude
ρ^+	fixed	fixed	± 0.015
ρ^0	± 0.005	± 0.3	± 0.03
ρ^-	± 0.003	± 0.2	± 0.02
<i>non res.</i>	± 0.17	± 0.6	± 0.05

	Standard Parameterization	New Parameterization
\mathcal{A}_{CP}	± 0.006	± 0.010

Table 3.16: The systematic errors associated with the signal fraction. The top table shows the errors on the standard parameterization, presented in the usual order (the D^0 sample, the \overline{D}^0 sample, and the combined D^0 and \overline{D}^0 sample). The middle table shows the errors on the new parameterization. The bottom table shows the errors on the \mathcal{A}_{CP} numbers

Event Selection Variable (units)	Standard Cut	Looser Cut	Tighter Cut
D^0 Mass (GeV/c^2)	$1.841 < x < 1.885$	$1.833 < x < 1.893$	$1.8515 < x < 1.8745$
D^{*+} Momentum Fraction	$x > 0.70$	$x > 0.655$	$x > 0.75$
$D^{*+} - D^0$ Mass Difference (MeV/c^2)	$-0.604 < x < 0.691$	$-0.824 < x < 0.911$	$-0.331 < x < 0.403$
Minimum π^0 Daughter Energy (MeV)	$x > 100$	$x > 75$	$x > 150$

Table 3.17: Summary of how much event selection criteria were tighten and loosened. See Section 3.3.2 for a complete discussions of these criteria.

Resonance	Amplitude	Phase($^{\circ}$)	Fit Fraction(%)
ρ^+	fixed	fixed	$\pm 3.4 \pm 3.0 \pm 1.0 \pm 5.1 = \pm 6.9$ $\pm 2.5 \pm 1.1 \pm 0.9 \pm 3.2 = \pm 4.3$ $\pm 1.0 \pm 1.8 \pm 0.9 \pm 4.2 = \pm 4.8$
ρ^0	$\pm 0.05 \pm 0.05 \pm 0.01 \pm 0.08 = \pm 0.11$ $\pm 0.02 \pm 0.02 \pm 0.01 \pm 0.05 = \pm 0.06$ $\pm 0.015 \pm 0.025 \pm 0.005 \pm 0.064 = \pm 0.070$	$\pm 2.0 \pm 2.9 \pm 1.6 \pm 0.9 = \pm 3.9$ $\pm 1.9 \pm 2.5 \pm 1.5 \pm 2.0 = \pm 4.0$ $\pm 0.8 \pm 2.0 \pm 1.1 \pm 1.2 = \pm 2.7$	$\pm 3.0 \pm 3.1 \pm 1.1 \pm 5.6 = \pm 7.1$ $\pm 1.1 \pm 1.2 \pm 0.4 \pm 3.4 = \pm 3.8$ $\pm 1.0 \pm 1.5 \pm 0.4 \pm 4.1 = \pm 4.6$
ρ^-	$\pm 0.031 \pm 0.013 \pm 0.020 \pm 0.037 = \pm 0.054$ $\pm 0.031 \pm 0.017 \pm 0.015 \pm 0.033 = \pm 0.051$ $\pm 0.012 \pm 0.011 \pm 0.004 \pm 0.033 = \pm 0.037$	$\pm 1.4 \pm 0.6 \pm 1.1 \pm 1.6 = \pm 2.5$ $\pm 4.2 \pm 4.3 \pm 3.0 \pm 2.8 = \pm 7.3$ $\pm 2.7 \pm 2.0 \pm 1.0 \pm 1.6 = \pm 3.9$	$\pm 1.7 \pm 0.8 \pm 1.9 \pm 1.4 = \pm 3.0$ $\pm 2.1 \pm 1.4 \pm 1.4 \pm 2.0 = \pm 3.5$ $\pm 0.7 \pm 0.8 \pm 0.4 \pm 1.4 = \pm 1.8$
<i>non res.</i>	$\pm 0.03 \pm 0.32 \pm 0.19 \pm 0.05 = \pm 0.37$ $\pm 0.19 \pm 0.02 \pm 0.15 \pm 0.07 = \pm 0.25$ $\pm 0.12 \pm 0.15 \pm 0.17 \pm 0.03 = \pm 0.26$	$\pm 11 \pm 18 \pm 8 \pm 4 = \pm 23$ $\pm 13 \pm 11 \pm 7 \pm 5 = \pm 19$ $\pm 5 \pm 7 \pm 4 \pm 4 = \pm 10$	$\pm 0.1 \pm 1.9 \pm 1.0 \pm 0.2 = \pm 2.2$ $\pm 0.9 \pm 0.1 \pm 0.8 \pm 0.5 = \pm 1.3$ $\pm 0.6 \pm 0.8 \pm 0.9 \pm 0.1 = \pm 1.4$

8

Resonance	Conserving Amplitude	Conserving Phase($^{\circ}$)	Violating Amplitude
ρ^+	fixed	fixed	$\pm 0.03 \pm 0.11 \pm 0.01 \pm 0.07 = \pm 0.13$
ρ^0	$\pm 0.01 \pm 0.02 \pm 0.01 \pm 0.06 = \pm 0.07$	$\pm 0.9 \pm 1.9 \pm 0.6 \pm 1.3 = \pm 2.5$	$\pm 0.03 \pm 0.04 \pm 0.02 \pm 0.01 = \pm 0.05$
ρ^-	$\pm 0.014 \pm 0.009 \pm 0.004 \pm 0.034 = \pm 0.038$	$\pm 2.8 \pm 2.0 \pm 1.3 \pm 1.8 = \pm 4.1$	$\pm 0.02 \pm 0.07 \pm 0.02 \pm 0.06 = \pm 0.10$
<i>non res.</i>	$\pm 0.13 \pm 0.13 \pm 0.17 \pm 0.04 = \pm 0.25$	$\pm 4.5 \pm 6.6 \pm 4.4 \pm 4.8 = \pm 10.3$	$\pm 0.15 \pm 0.21 \pm 0.04 \pm 0.08 = \pm 0.27$

	Standard Parameterization	New Parameterization
\mathcal{A}_{CP}	$\pm 0.04 \pm 0.07 \pm 0.03 \pm 0.03 = \pm 0.09$	$\pm 0.04 \pm 0.20 \pm 0.07 \pm 0.22 = \pm 0.31$

Table 3.18: The systematic errors associated with the event selection criteria. Each error is presented as the error due to D^0 mass cuts, D^{*+} momentum cuts, mass difference cuts, π^0 daughter energy cuts, and the total systematic error due to cuts. The top table displays the errors on the standard parameterization, presented in the usual order (the D^0 sample, the \overline{D}^0 sample, and the combined D^0 and \overline{D}^0 sample). The middle table shows the errors on the new parameterization. The bottom table shows the errors on the \mathcal{A}_{CP} numbers.

Resonance	Amplitude	Phase($^{\circ}$)	Fit Fraction(%)
ρ^+	fixed	fixed	$\pm 6.9 \pm 0.5 \pm 0.3 \pm 0.4 = \pm 6.9$ $\pm 4.3 \pm 0.5 \pm 0.3 \pm 0.9 = \pm 4.4$ $\pm 4.8 \pm 0.5 \pm 0.4 \pm 0.4 = \pm 4.8$
ρ^0	$\pm 0.107 \pm 0.004 \pm 0.003 \pm 0.014 = \pm 0.108$ $\pm 0.057 \pm 0.005 \pm 0.005 \pm 0.021 = \pm 0.061$ $\pm 0.070 \pm 0.004 \pm 0.006 \pm 0.004 = \pm 0.071$	$\pm 3.9 \pm 0.3 \pm 0.5 \pm 0.6 = \pm 4.0$ $\pm 4.0 \pm 0.3 \pm 0.4 \pm 0.4 = \pm 4.1$ $\pm 2.7 \pm 0.3 \pm 0.8 \pm 0.2 = \pm 2.8$	$\pm 7.1 \pm 0.3 \pm 0.2 \pm 1.3 = \pm 7.3$ $\pm 3.8 \pm 0.3 \pm 0.4 \pm 2.0 = \pm 4.3$ $\pm 4.6 \pm 0.3 \pm 0.6 \pm 0.5 = \pm 4.6$
ρ^-	$\pm 0.054 \pm 0.007 \pm 0.006 \pm 0.020 = \pm 0.058$ $\pm 0.051 \pm 0.008 \pm 0.006 \pm 0.019 = \pm 0.055$ $\pm 0.037 \pm 0.007 \pm 0.011 \pm 0.004 = \pm 0.039$	$\pm 2.5 \pm 0.4 \pm 0.6 \pm 0.3 = \pm 2.6$ $\pm 7.3 \pm 0.4 \pm 0.6 \pm 0.5 = \pm 7.3$ $\pm 3.9 \pm 0.4 \pm 1.1 \pm 0.1 = \pm 4.0$	$\pm 3.0 \pm 0.5 \pm 0.4 \pm 2.0 = \pm 3.6$ $\pm 3.5 \pm 0.6 \pm 0.6 \pm 1.9 = \pm 4.1$ $\pm 1.8 \pm 0.5 \pm 0.9 \pm 0.6 = \pm 2.2$
<i>non res.</i>	$\pm 0.37 \pm 0.02 \pm 0.02 \pm 0.16 = \pm 0.41$ $\pm 0.25 \pm 0.02 \pm 0.03 \pm 0.18 = \pm 0.31$ $\pm 0.26 \pm 0.02 \pm 0.02 \pm 0.17 = \pm 0.31$	$\pm 22.8 \pm 1.4 \pm 2.4 \pm 6.6 = \pm 23.9$ $\pm 19.3 \pm 1.3 \pm 3.0 \pm 7.5 = \pm 21.0$ $\pm 10.0 \pm 1.3 \pm 4.9 \pm 0.4 = \pm 11.2$	$\pm 2.2 \pm 0.1 \pm 0.1 \pm 0.9 = \pm 2.4$ $\pm 1.3 \pm 0.1 \pm 0.1 \pm 1.0 = \pm 1.7$ $\pm 1.4 \pm 0.1 \pm 0.1 \pm 0.9 = \pm 1.7$

Resonance	Conserving Amplitude	Conserving Phase($^{\circ}$)	Violating Amplitude
ρ^+	fixed	fixed	$\pm 0.13 \pm 0.02 \pm 0.02 \pm 0.02 = \pm 0.14$
ρ^0	$\pm 0.065 \pm 0.004 \pm 0.006 \pm 0.005 = \pm 0.066$	$\pm 2.5 \pm 0.3 \pm 0.9 \pm 0.3 = \pm 2.7$	$\pm 0.05 \pm 0.01 \pm 0.01 \pm 0.03 = \pm 0.06$
ρ^-	$\pm 0.038 \pm 0.007 \pm 0.010 \pm 0.003 = \pm 0.040$	$\pm 4.1 \pm 0.4 \pm 1.2 \pm 0.2 = \pm 4.3$	$\pm 0.10 \pm 0.01 \pm 0.01 \pm 0.02 = \pm 0.10$
<i>non res.</i>	$\pm 0.25 \pm 0.02 \pm 0.02 \pm 0.17 = \pm 0.30$	$\pm 10.3 \pm 1.3 \pm 5.0 \pm 0.6 = \pm 11.6$	$\pm 0.27 \pm 0.01 \pm 0.02 \pm 0.05 = \pm 0.27$

	Standard Parameterization	New Parameterization
\mathcal{A}_{CP}	$\pm 0.085 \pm 0.001 \pm 0.002 \pm 0.006 = \pm 0.086$	$\pm 0.31 \pm 0.20 \pm 0.04 \pm 0.10 = \pm 0.38$

Table 3.19: The total systematic errors presented in order of event section, efficiency, background, signal fraction, and total. The top table shows the errors on the standard parameterization, presented in the usual order (the D^0 sample, the $\overline{D^0}$ sample, and the combined D^0 and $\overline{D^0}$ sample). The middle table shows the errors on the new parameterization. The bottom table shows the errors on the \mathcal{A}_{CP} numbers.

3.10 Final Results

The final results are presented in Table 3.20

Resonance	Amplitude	Phase($^\circ$)	Fit Fraction(%)
ρ^+	1. (fixed)	0. (fixed)	$76.6 \pm 2.5 \pm 6.9$ $76.0 \pm 2.7 \pm 4.4$ $76.5 \pm 1.8 \pm 4.8$
ρ^0	$0.57 \pm 0.03 \pm 0.11$ $0.55 \pm 0.04 \pm 0.06$ $0.56 \pm 0.02 \pm 0.07$	$10 \pm 4 \pm 4$ $9 \pm 4 \pm 4$ $10 \pm 3 \pm 3$	$24.9 \pm 2.4 \pm 7.3$ $22.5 \pm 2.7 \pm 4.3$ $23.9 \pm 1.8 \pm 4.6$
ρ^-	$0.64 \pm 0.03 \pm 0.06$ $0.67 \pm 0.04 \pm 0.06$ $0.65 \pm 0.03 \pm 0.04$	$176 \pm 4 \pm 3$ $177 \pm 4 \pm 7$ $176 \pm 3 \pm 4$	$31.0 \pm 2.8 \pm 3.6$ $34.0 \pm 3.0 \pm 4.1$ $32.3 \pm 2.1 \pm 2.2$
<i>non res.</i>	$1.03 \pm 0.24 \pm 0.41$ $1.03 \pm 0.24 \pm 0.31$ $1.03 \pm 0.17 \pm 0.31$	$72 \pm 11 \pm 24$ $84 \pm 11 \pm 21$ $77 \pm 8 \pm 11$	$2.8 \pm 1.4 \pm 2.4$ $2.7 \pm 1.4 \pm 1.7$ $2.7 \pm 0.9 \pm 1.7$

Resonance	Conserving Amplitude	Conserving Phase($^\circ$)	Violating Amplitude
ρ^+	1. (fixed)	0. (fixed)	$0.04 \pm 0.21 \pm 0.14$
ρ^0	$0.56 \pm 0.02 \pm 0.07$	$10 \pm 3 \pm 3$	$0.03 \pm 0.19 \pm 0.06$
ρ^-	$0.65 \pm 0.03 \pm 0.04$	$176 \pm 3 \pm 4$	$0.03 \pm 0.11 \pm 0.10$
<i>non res.</i>	$1.03 \pm 0.17 \pm 0.30$	$78 \pm 8 \pm 12$	$0.07 \pm 0.18 \pm 0.27$

	Standard Parameterization	New Parameterization
A_{CP}	$0.01_{-0.07}^{+0.09} \pm 0.09$	$0.02 \pm 0.06 \pm 0.38$

Table 3.20: All numbers are quoted with statistical errors first and then systematic errors. The top table shows the numbers from the standard parameterization, presented in the usual order (the D^0 sample, the $\overline{D^0}$ sample, and the combined D^0 and $\overline{D^0}$ sample). The middle table shows the values of the new parameterization. The bottom table shows the values on the two A_{CP} fits.

3.11 Conclusions

We have reported on our Dalitz Analysis of $D^0 \rightarrow \pi^- \pi^+ \pi^0$. While we find large fit fractions for the three light ρ resonances ($D^0 \rightarrow \rho^+ \pi^-$, $D^0 \rightarrow \rho^- \pi^+$, and $D^0 \rightarrow \rho^0 \pi^0$) as well as a small but significant non-resonant contribution, we do not find any significant contributions from any other resonances (including the $\sigma(500)$, the ρ_{1450} s, and the ρ_{1700} s).

The $\sigma(500)$ is a controversial particle whose existence has not yet been confirmed. E791[19] found strong evidence for it in their $D^+ \rightarrow \pi^- \pi^+ \pi^+$ analysis (they found a fit fraction of almost 50%), but we see none here. Whether the lack of evidence for the $\sigma(500)$ in this analysis indicates a lack of sensitivity or suggests that this particle does not exist is very interesting question which deserves further study.

The lack of the heavy ρ 's is also interesting. In CLEO's analysis $D^0 \rightarrow K^- \pi^+ \pi^0$, [18] the ρ_{1700}^+ was needed for the final fits. If $D^0 \rightarrow K^- \rho_{1700}^+$, one might expect to see the $D^0 \rightarrow \pi^- \rho_{1700}^+$ as well. It is interesting to note that in $D^0 \rightarrow K^- \pi^+ \pi^0$, the nominal peak location of the ρ_{1700}^+ is outside the boundary of the Dalitz plot making this analysis sensitive only to the tail of this resonance. In $D^0 \rightarrow \pi^- \pi^+ \pi^0$, the peak of the ρ_{1700} resonances are all be contained within the boundary of the Dalitz plot, making $D^0 \rightarrow \pi^- \pi^+ \pi^0$ a more suitable laboratory for studying these heavy resonances. Again, this begs for further investigation as more statistics become available.

Finally, we see no evidence for CP violation, either from comparing the amplitudes, phases, and fit fractions from the separate $D^0 \rightarrow \pi^- \pi^+ \pi^0$ and $\overline{D}^0 \rightarrow \pi^+ \pi^- \pi^0$ fits, from our analysis using the new CP parameterization, or in either of the \mathcal{A}_{CP} numbers. The recent theoretical work expects asymmetries on the order of 0.1%. [20, 21] but we do not yet have enough sensitivity to confirm or refute these findings.

Chapter 4

The CLEO III Trigger

I spent the largest part of my time as a graduate student working on the simulation, design, layout, testing, commissioning, and maintenance of the CLEO III Trigger. This chapter is an overview of the trigger system as a whole and an in-depth look at the CLEO III Stereo Tracking Trigger (STTR).

4.1 CLEO III Detector

Before talking about the trigger, I want to provide a glimpse of the differences between CLEO II.V and CLEO III. The largest difference is that instead of having two drift chambers that go out to just under 1 *m* and Time of Flight scintillator paddles, CLEO III has a smaller unique drift chamber ($r = 80$ *cm*) followed by a Ring Imaging Cherenkov detector (RICH). The RICH uses Cherenkov radiation to aid in particle identification (see Figure 2.3 for a picture of CLEO II.V and Figure 4.1 for a picture of CLEO III).

4.2 Trigger Requirements and Realities

There were two requirements for the CLEO III trigger. The first was that the specifications for the CLEO III Data Acquisition (DAQ) allowed for the CLEO III detector

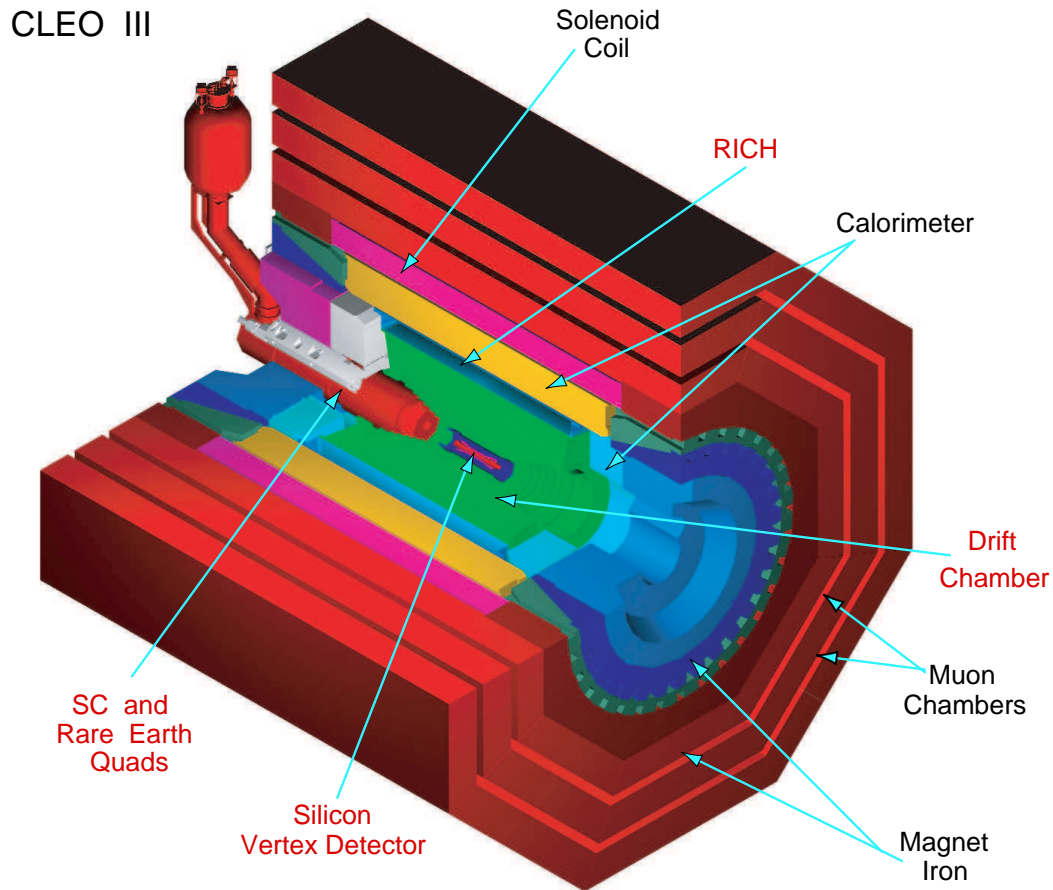


Figure 4.1: A view of the CLEO III detector.

to be read out up to 1000 hz. The second was that the trigger needed to decide whether to accept an event or not in under $3 \mu s$.

With the advance of available technology, it was decided that unlike the CLEO II Trigger which had 3 distinct hardware triggers (i.e. Level 0, Level 1, and Level 2; see Section 2.2.7 for a description of the CLEO II trigger), we could do what was needed in a single hardware trigger (Level 1). Another important difference is deadtime. While the CLEO II L1 or L2 trigger was deciding about an interesting event, it froze the detector and ignored all events until it made a decision. With CLEO III, there is no deadtime until after the trigger decision has been made and an event is being

read out of the detector.

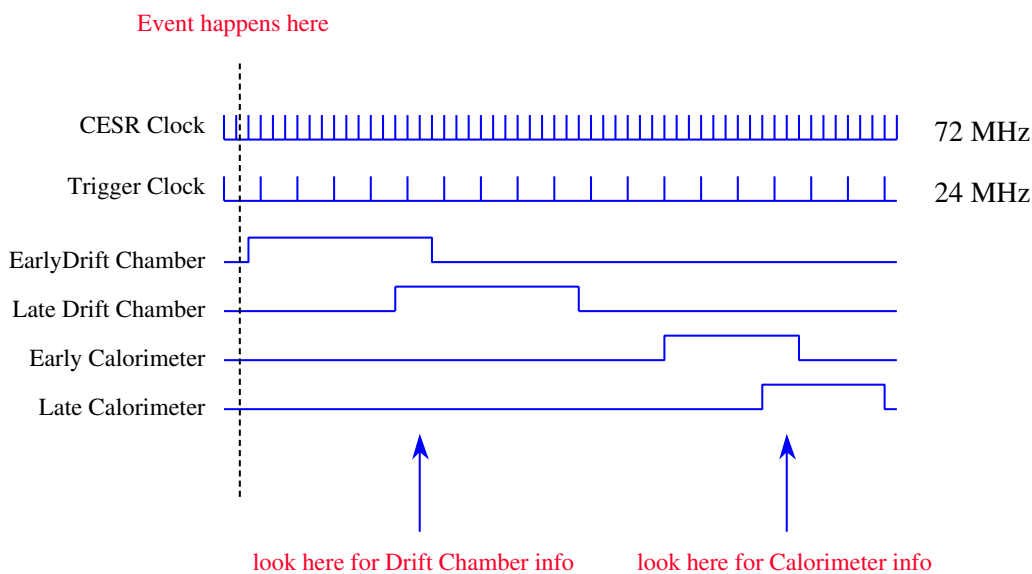


Figure 4.2: A diagram showing event timing in the CLEO III trigger.

Ideally, we would like the trigger to examine every bunch crossing to see if anything interesting has occurred. Unfortunately, CESR runs with a bunch spacing of only 14 ns and with current technology this is just not enough time to finish the type of calculations we need to do during each such step. As a compromise it was decided to examine the detector every three crossings, or 42 ns . Since the probability is very small that any given beam crossing will result in detector hits, this effective integration is not a problem.

The complete trigger processing of a single crossing involves many such 42 ns steps being done in a pipelined fashion. In addition to this, information from the calorimeter takes longer to reach the trigger than information from the drift chamber, which means that the tracking trigger output needs to be delayed by a simple "bucket brigade" type pipeline. See Figure 4.2 for a diagram of the timing of the trigger.

Although a trigger decision is made every 42 ns , the pipelined nature of the trigger hardware means that the decision for any given beam crossing appears about $2.7\text{ }\mu\text{s}$

after the crossing that caused it.

The CLEO III trigger looks at the information from the Crystal Calorimeter (CC) and the Drift Chamber (DR). The tracking and calorimeter information is processed in parallel and combined in the Level 1 decision crate to make a final decision (see Figure 4.3).

Unfortunately, without a fast system like the Time of Flight system in CLEO II, it is much more difficult to determine the event time exactly. Our solution to this problem will be presented in Section 4.5.3.

4.3 Hardware Implementation

With the exception of the Analog Crystal Calorimeter, all trigger components are remarkably similar¹. All are 9 *u* VME boards made with Printed Circuit Board (PCB) construction. All of the boards rely heavily on Field Programmable Gate Array (FPGA) technology. FPGAs are essentially complicated reprogrammable assemblies of digital “AND”s, “OR”s, and other simple logic components such as latches. All of the FPGAs are reprogrammable *in-situ*.

The general structure is as follows (see Figure 4.4): From the input connectors, all boards pass signals both to the circular buffers (to be read out) and to the trigger logic. The output of the trigger logic goes to the output connectors and then to the next board in the chain. To help diagnose trigger problems, all trigger boards record their inputs in circular buffers (except for the last board in the series which instead records its outputs).

¹This includes the TPRO, SURF, AXTR, AXPR, STTR, TRCR, LUMI, and L1Trig. As an interesting aside, due to the many different needs of the CLEO III trigger, there are more types of data boards in the trigger than the rest of the experiment combined.

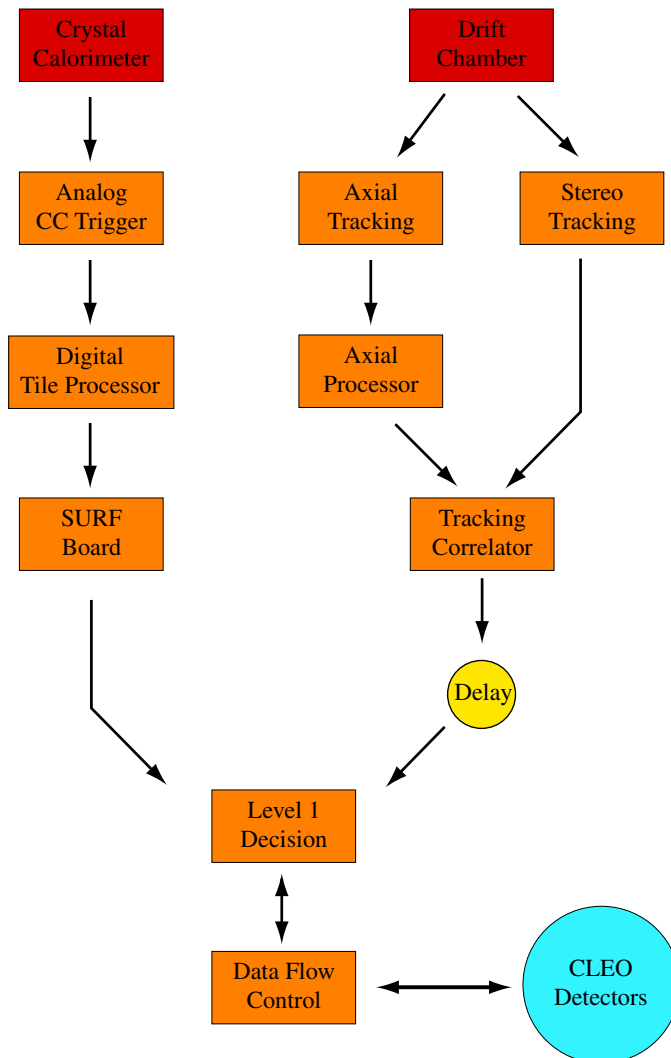


Figure 4.3: An overview of the CLEO III Trigger system.

4.4 Crystal Calorimeter Trigger

CLEO III uses the same thallium-doped cesium-iodide crystals used in CLEO II.V. The layout of the barrel is identical and the endcaps have been rearranged slightly to allow for CESR's superconducting quadrupole focusing magnets. The trigger uses both the endcap and barrel crystals. The layout and function of the barrel CC trigger are presented; the function of the endcap is almost identical.

Trigger Board Structure

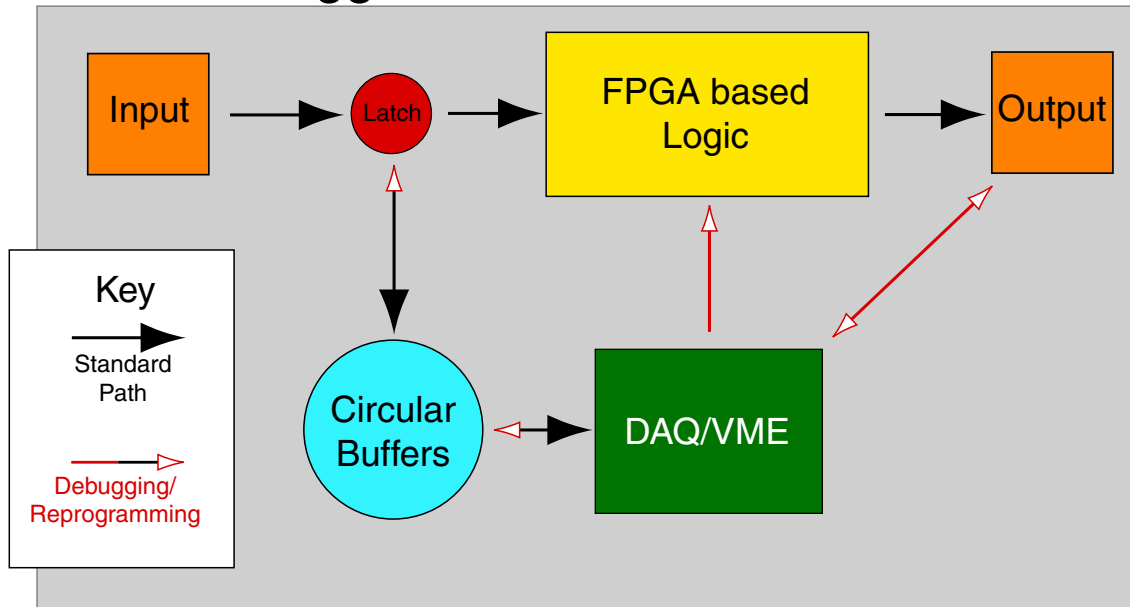


Figure 4.4: An overview of the general trigger board. The standard path is for the inputs to through a latch and go to both the trigger logic and the circular buffers. The outputs of the logic section then to the output connectors on the boards. For debugging purposes, we can fill the circular buffers from the VME interface, forcing the bits through the trigger logic and putting the output back into the VME interface. We can also use the VME interface to reprogram some of the logic FPGAs. Last but not least, we can also use VME to set various output patterns to test the output connector, the cables, and the input connectors of the next board.

If the barrel is “unrolled”, it is a rectangle of 48 ($45 < \theta < 135$) by 128 crystals ($0 \leq \phi < 360$). The 6144 crystals that make up the barrel are too many to process individually, so we group them in “tiles” of 4×4 crystals (\Rightarrow 384 tiles in the barrel).

4.4.1 Analog Crystal Calorimeter Trigger

The first step of the CC Trigger is the Analog CC Trigger. It receives analog inputs from CC crates and produces a multi-level digital output: off, low, medium, high².

²The thresholds for each level are individually set for each tile.

One of the biggest problems with the CLEO II.V CC trigger is that of the boundaries of the tiles. Regardless of the granularity, it is always possible for a photon (or other particle) to deposit its energy in more than one tile. A 1.7 GeV photon that leaves all of its energy in one tile will easily pass a 1.5 GeV threshold (the “high” threshold for the $\Upsilon(4s)$ running). The same photon, however, may not even pass the “medium” threshold (700 MeV) if it shares its energy equally over 4 tiles by hitting the common corner of the tiles.

To address this problem, the Analog CC trigger has been built with the ability to do “tile summing” or “sharing”. When tile summing is enabled, every tile looks not only at its own energy, but its three nearest neighbors’ as well (the tile to the right, the tile below, and the tile diagonal; see Figure 4.5). Using the tile summing, our 1.7 GeV photon that hit the corner of 4 tiles would now satisfy the 1.5 GeV high threshold.

Because of the slow nature of light produced in the crystals, the Analog CC Trigger can take up to $1.5\ \mu\text{s}$ to produce its output. It is by far the slowest part of the trigger system.

4.4.2 Digital Crystal Calorimeter Trigger

Tile summing is a great method for efficiency, but it can also cause over-counting. With the first example above, a 1.7 GeV photon that leaves all of its energy in one tile will now have 4 tiles reporting a high hit. It is the first job of the Tile Processor (TPRO) to undo this over-counting (see Figure 4.6). The TPRO also makes binned ϕ and θ projections.

The final part of the CC Trigger is the SURF boards³. These boards look at the information provided by the TPROs and look for geometric patterns (e.g. back-to-back high showers). The outputs for both the TPROs and the SURFs are passed to

³Like CLEO, SURF was supposed to be an acronym for something and like CLEO, we never got around to deciding *what* it should stand for.

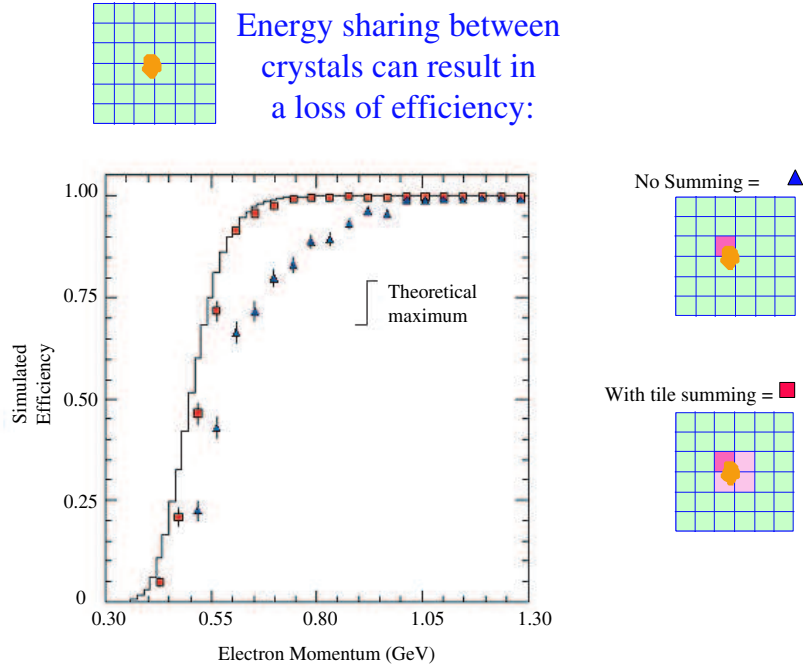


Figure 4.5: A turn-on curve with and without tile summing.

the Level 1 Decision Crate.

4.5 Tracking Trigger

There are several differences between the CLEO II and CLEO III drift chambers. First, there is a single drift chamber for CLEO III as compared to the vertex detector and the outer drift chambers in CLEO II.V. Second, the outer radius of the CLEO III drift chamber is significantly smaller than that of CLEO II (80 *cm* versus 100 *cm*). Finally, instead of having intermingled rows of axial and stereo⁴ sense wires as in CLEO II, the inner 16 sense layers are all axial and the outer 31 sense layers are all stereo. This last difference led us to do axial tracking and stereo tracking separately in the trigger.

⁴Axial wires are parallel to the beam pipe, and without charge division information, give only ϕ information. Stereo wires are tilted slightly with respect to the beam pipe and can be used to give us z information when the tracks of charged particles are reconstructed.

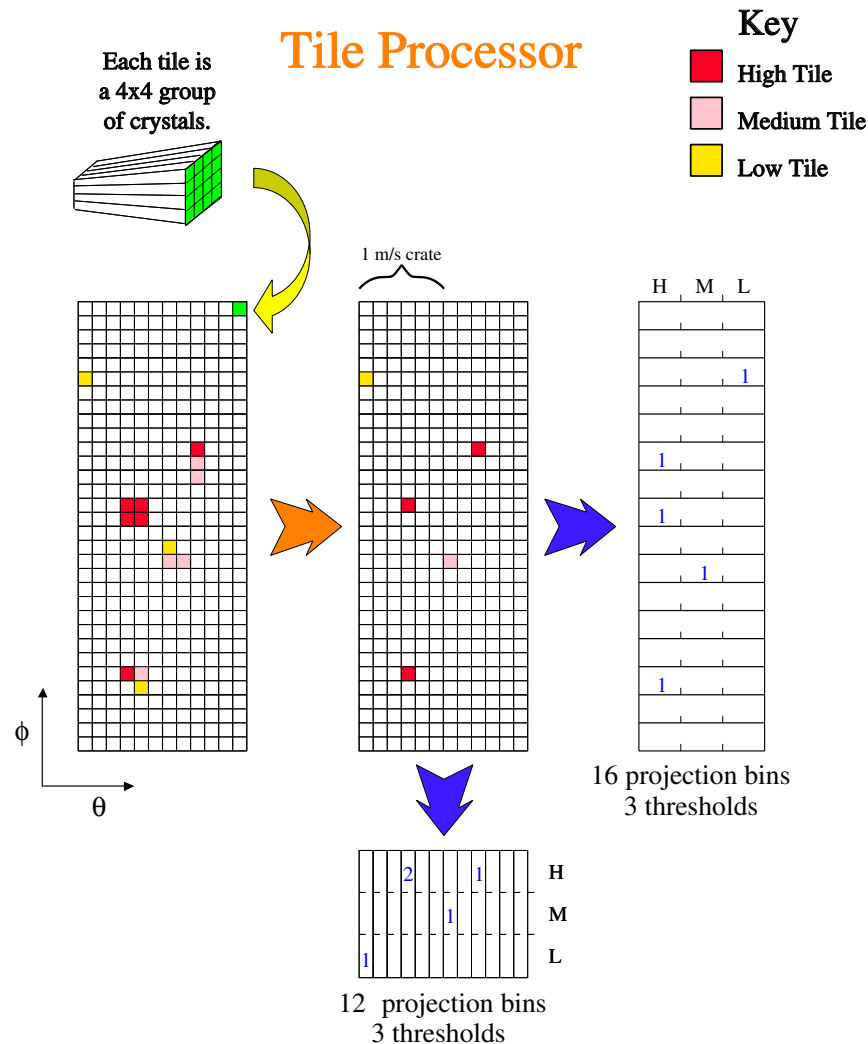


Figure 4.6: The Tile Processor takes care of both over-counting and making ϕ and θ projections.

It is very important to remember that there is a large range of drift times associated with a drift chamber. In the case of the CLEO III Drift Chamber, the drift time can range from 0 (as the charge track can pass arbitrarily close to the sense wire) up to over 400 ns (if the charged track passes through the edge of the drift cell). To deal with this range, any wire that has been “hit” will remain so for 750 ns. This assures that the wires hit the earliest are still counted as hit when the last stragglers come

home.

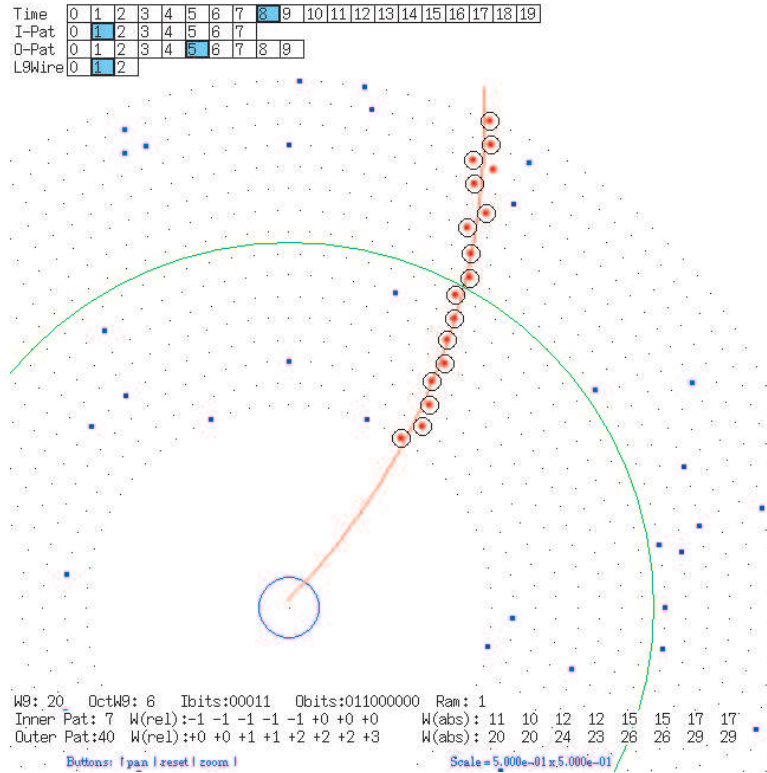


Figure 4.7: The AXTR looks at the inner eight and outer eight layers separately. In this case, since there is one hit per layer for the inner eight layers and at least one hit per layer in the outer eight layers, multiple patterns are satisfied.

4.5.1 Axial Tracking Trigger

In the axial section of the CLEO III Drift Chamber, there are 1696 sense wires. The Axial Tracking Trigger (AXTR) looks at each individual wire. For the purpose of finding tracks, the AXTR looks at the inner eight and the outer eight layers separately. For each possible inner and outer pattern, if hits are successfully found in at least six out of eight layers, the pattern is projected to the layer 9 wire (“key wire”) it would hit. If both inner and outer patterns for a key wire are hit and the slopes of the inner and outer patterns point in the same direction, the key wire is asserted as

having found a track. There are 112 key wires and 16 AXTR boards. See Figure 4.7 for a graphical example. It is important to note that using the layer 9 wires as the key wires is a bookkeeping trick. A track can still be found even if its corresponding layer 9 wire is not hit.

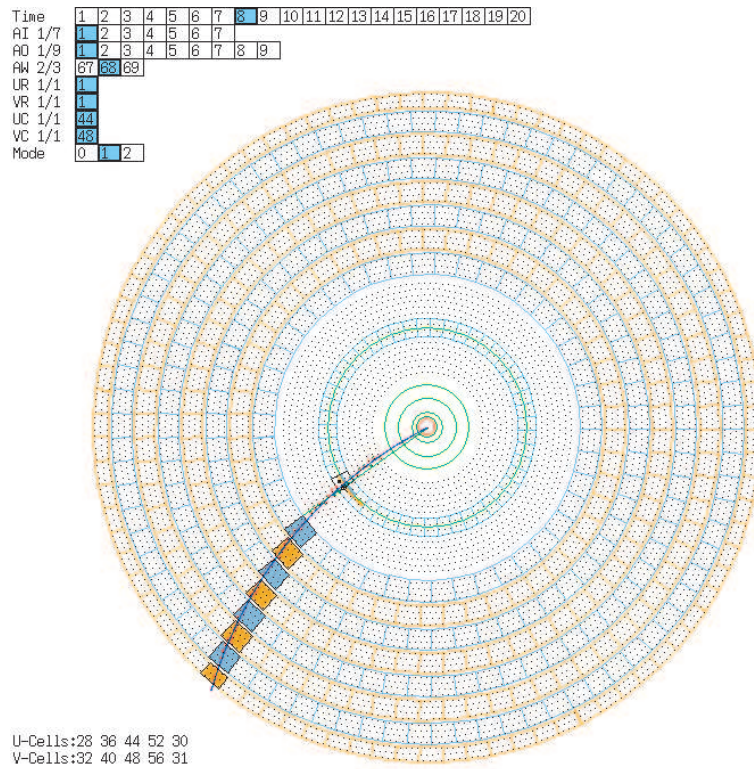


Figure 4.8: The STTR tracks the U superlayers and V superlayers separately. In order for a stereo track to be found, all four blocks (U or V) must be present.

4.5.2 Stereo Tracking Trigger

In the stereo section of the Drift Chamber, there are 8100 sense wires. As mentioned earlier, stereo wires are not parallel to the beam pipe, but rather have a slight tilt. The Drift Chamber was constructed so that the first four stereo layers tilt one way, the next four tilt the other way, the third group of four tilt the first way, etc. These alternating groups of four layers are called “superlayers.” The U superlayers contain

layers 17 – 20, 25 – 28, 33 – 36, and 41 – 44; the V superlayers contain layers 21 – 24, 29 – 32, 37 – 40, and 45 – 47.

Since it would prove to be very costly to build a group of boards that looks at all 8100 wires individually, the Drift Chamber electronics sends us information as to whether a 4×4 block of wires is “on” if there are hits in three out of four layers⁵. See Figure 4.8. The U and V superlayers are tracked independently. In order to have a U or V stereo track, blocks in all four superlayers must be present. When a stereo track is found, it is projected back to determine where it would cross layer 9 (the axial key layer) and projected to where in ϕ it would enter in the CC barrel. When projected back to the axial key layer, information is also provided as to whether the track is a low momentum positively charged track, a low momentum negatively charged track, or a high momentum track (for which no charge interpretation is made).

4.5.3 The Axial Processor and the Tracking Correlator

The last section of the Tracking Trigger is the Axial Processor (AXPR) and the Tracking Correlator (TRCR). The AXPR has two important functions. First, we reduce the granularity of the axial tracking. The 112 key wires are reduced to 48 ϕ bins.

Second, since we do not have a fast timing system in CLEO III (i.e. there is no equivalent to the Time of Flight in CLEO II), we need a way to decide when the event happened. In the axial section of the drift chamber, the wires that were hit the earliest will start to disappear 750 ns (the width of the discriminator) after the event. The wires that are hit the latest can take over 1,150 ns ($= 750 ns$ for the discriminator width $+400 ns$ for the drift time). If we look at how many of the key wires are hit every 42 ns , we will see that right after the event happens there are none. After several buckets, we will start seeing tracks. When the number of

⁵Deciding whether a 4×4 block is “on” is a more difficult task than it would originally appear. This is discussed in much greater detail later in Section 4.7.2.

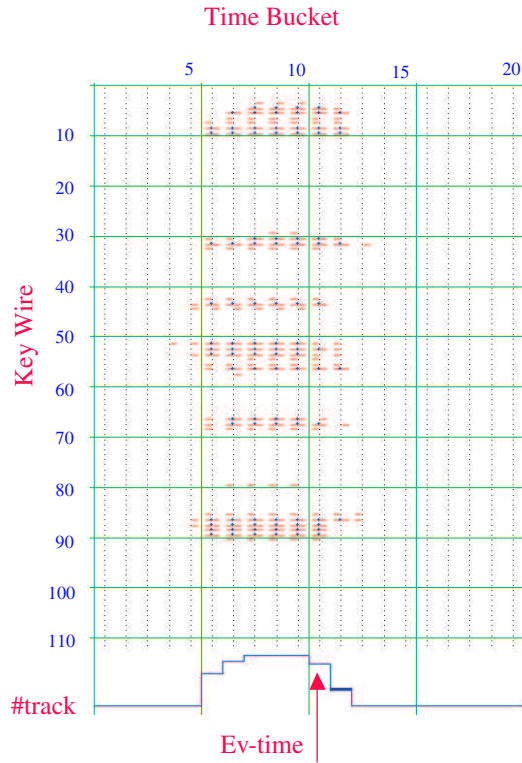


Figure 4.9: The AXPR calculates event time by watching the number of the 112 key wires that are hit.

tracks starts to decrease, we know we have as much information as we are going to get, and we set an event time (See Figure 4.9). Put another way, when using this algorithm, we are sensitive to when the very first hits appeared in the drift chamber. A similar calculation is made in the Crystal Calorimeter Trigger system as well, with the numbers of low, medium, and high showers.

The TRCR is used to find the overlap between the axial and stereo tracks. Due to the tilt in the stereo wires, a given track will often point back to a dozen key wires. In order for a stereo track to be asserted, there must be an overlapping axial track.

All of the information from the AXPR and the TRCR is passed through a pipelined delay to the Level 1 Trigger boards.

Inputs to the Level 1 Decision
24 bits of axial track topologies 24 bits of stereo projections into the CC 8 bits of low energy barrel ϕ topology 8 bits of high energy barrel ϕ topology
Number of high momentum stereo tracks Number of low momentum stereo tracks Number of axial tracks Number of low energy barrel showers Number of medium energy barrel showers Number of high energy barrel showers Number of low energy endcap showers Number of medium energy endcap showers Number of high energy endcap showers
Barrel CC low energy back-to-back status Barrel CC medium energy back-to-back status Barrel CC high energy back-to-back status Endcap CC low energy back-to-back status Endcap CC medium energy back-to-back status Endcap CC high energy back-to-back status
Tracking timing bits Barrel CC timing bits Endcap CC timing bits
Flag if only low momentum positive tracks are present 8 external trigger inputs (1 currently used for random trigger)

Table 4.1: The inputs to the Level 1 decision making process present as signals on the L1D backplane.

4.6 The Level 1 Decision and Data Flow Control

The outputs of the CC trigger from the SURF boards as well as the tracking trigger from the Axial Processor and the Tracking Correlators are put on the custom backplane of the Level 1 Decision (L1D) crate (see Table 4.1 for a complete list of inputs). The two types of boards that make up the Level 1 Decision, the LUMI and the Level 1 Trigger (L1TRIG) boards, read all of the information from the backplane. The L1TRIG boards make the decision to accept an event. They look at both counts (e.g.

Trigger Line	Requirements
Barrel Bhabha	Back-to-back showers in barrel CC
μ -pair	Back-to-back high stereo tracks with exactly 2 high tracks
Hadron	At least three axial tracks and one low shower in barrel CC

Table 4.2: Examples of our current Level 1 trigger lines. Note, first, that the lines are named by the processes we are hoping to trigger on, not a guarantee of only getting that process. Second, a single event will often pass more than one Level 1 trigger line at a time. All barrel bhabhas (electron and positron scatter off of each other) should pass both the Barrel Bhabha line as well as the μ -pair line.

number of high showers in the barrel calorimeter) and topology (e.g. back-to-back high momentum charged tracks). Sample trigger lines are shown below in Table 4.2. As mentioned earlier, the L1TRIG records its outputs, not its inputs.

The LUMI board has three major functions. First, it records all of the trigger primitives on the L1D backplane. Second, it looks at back-to-back high showers in the endcap calorimeter to calculate the luminosity (from which this board gets its name). Finally, the LUMI looks at all of the L1Trig boards for a Level 1 accept and sends the result to the Data Flow control crate.

The system is both expandable and flexible. We can have up to 8 L1TRIG boards in the system and each board can produce up to 24 active trigger lines (= 192 total lines). We can change which trigger lines are used by loading different constants at the start of a data collection run.

The final part of the CLEO III is the Data Flow Control Crates. In these crates are boards that communicate with every part of the CLEO III detector that gets read out during a trigger. This is the system that fans out the L1 Trigger signal to all crates while making sure that none of these crates are busy reading out a previous trigger (since not all detectors read out the same amount of data, it is often true that one part of the system has finished reading out an event while other parts are not yet finished).

4.7 The CLEO III Stereo Trigger In Depth

In this section I will talk about the details that went into designing, simulating, building and commissioning the CLEO III Stereo Trigger⁶. I will briefly describe the computer simulation that was used for the trigger development. Next, I will talk about the logic to decide whether a block is “hit” or not. Then I will talk about finding the patterns that form a stereo track. Finally, I will go into the maintenance of the STTR.

4.7.1 Simulation Basics

The basic tracking trigger simulation code was written mostly by Mats Selen. Its basic function was to take tracks of known initial momentum and position and “swim” them through the drift chamber. The simulation allows for less than perfect wire efficiency, multiple wires being hit on a layer⁷, and even keeps track of the timing of hits. In this simplified (as compared to full CLEO MC) simulation, particle interactions with material were completely ignored. It was this simulation that was used for generating patterns for axial and stereo tracks as well as stereo blocks.

4.7.2 Stereo Blocks

Before describing the logic of whether a block is hit or not, let us start with where the signals come from. Attached to the CLEO III Drift Chamber (DR) are pre-amplifiers that amplify the current on every DR sense wire. The output of the pre-amps are then sent to “TQT” boards which declare when a sense wire was hit and how much charge was deposited⁸. From the stereo section of the DR, each TQT board handles

⁶Just as an example to show to what length the author was dedicated to this hardware project, CLEO III Stereo Trigger, the dog, has recently celebrated his fourth birthday.

⁷If a track goes through the boundary between two sense wires, it is possible that both sense wires will record a hit. In this simulation, we could set it up to allow these multiple hit or simply assert the single wire closest to the track.

⁸The first “T” stands for time, the “Q” stands for charge, and the last “T” is for trigger.

a group of wires 4 layers deep (a superlayer) and 12 wires wide. In other words, each TQT board looks at three 4×4 blocks (see Figure 4.12).

In the TQT board, two separate paths of information develop. The time and charge information (as mentioned above) gets sent to DR crates to be read out in the event of a trigger. The other path is destined for the trigger. For the trigger, it is unimportant how much charge was deposited on the wire, but rather whether it passes a certain threshold or not. Once a wire has been determined to have been hit, it is set “on” for a controllable period of time (currently 750 *ns*).

The constraints on the logic for blocks are as follows:

- A block should be on if at least three out of four layers were hit with a recognized pattern.
- With no more than one hit per layer, no more than one block should be “hit”.
- Inputs can be shared from neighboring TQT boards, but not outputs. In other words, it is possible to know if one of the neighbors’ wires is hit, but it is not possible to know if the neighbor is calling a block hit.

Using the trigger simulation, we “generated” several million events of single tracks with transverse momentum (i.e. momentum perpendicular to the beam pipe) between 250 *MeV* and 5 *GeV* with perfect wire efficiency and only 1 hit per layer. We looked at all of the patterns found and kept all except the most rare (we threw out 9 patterns out of 25 because these nine patterns together occurred with a frequency of less than 0.01%). See Figure 4.10 for an example.

After finding our 14 patterns, we needed to decide which block is hit for each pattern. For every pattern, we designated a wire on layer 1 of the superlayer. The block that contains the layer 1 wire is considered hit.

Up to this point, everything has been pretty straightforward. Unfortunately, things are going to become more complicated. We want to make sure that we consider the block being hit even if only three out of four hits of a pattern are present. So, for every pattern found, we allow five possibilities (one possibility for each missing layer

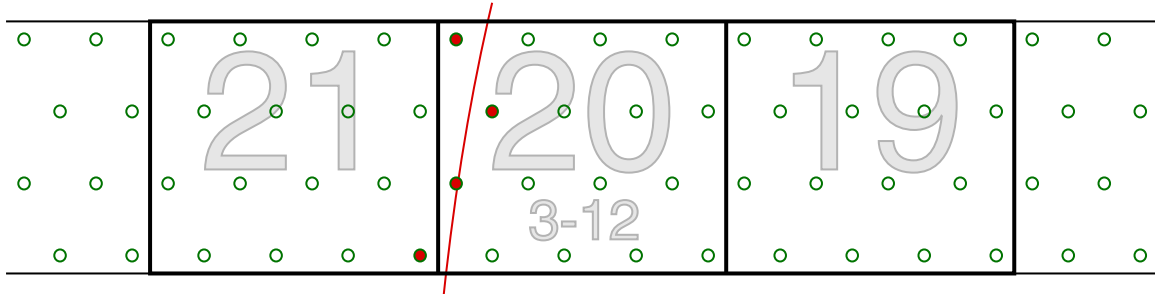


Figure 4.10: Here we have blocks 19 through 21 in superlayer 6 (see top center of Figure 4.12 to see where the blocks are in the Drift Chamber). The green circles are the wires that make up the blocks. These three blocks are fed information about their 48 wires by a single TQT card (in crate 3 slot 12). The red line is a track traversing the drift chambers with the red-filled circles being the wires that are hit.

(four possibilities) plus one possibility if all hits are present. Herein lies the problem. If you have a block that satisfies at least one of the 14 patterns with all layers hit, chances are good that you are going to also satisfy one of the other patterns with three out of four hits. If both patterns assert the same layer 1 wire, there isn't a problem. If, however, they assert two different layer 1 wires, we can end up with two blocks hit when there is only one hit per layer (see Figure 4.11 for an example).

In cases like this, we need to restrict some of the patterns. In this case, if we redefine pattern 6 so that it will not assert itself if it is missing the hit on the third wire, then we avoid this problem. Unfortunately, for most tracks of one hit per layer (as in the example of Figure 4.10), five different patterns will be satisfied. In order to make sure we only have one block hit when you only have one hit per layer, we had to study the overlaps between the different patterns. All patterns, their overlaps, and the exclusions placed on them are detailed in Appendix B.

One final word on the patterns. Consider at Figure 4.11 and imagine that the example near block 20, would be on the edge of block 21 instead. Since block 21 is on the boundary between TQT boards and it requires knowledge about the hits in block 22, this block needs to know about hits on a different TQT board. To allow for this,

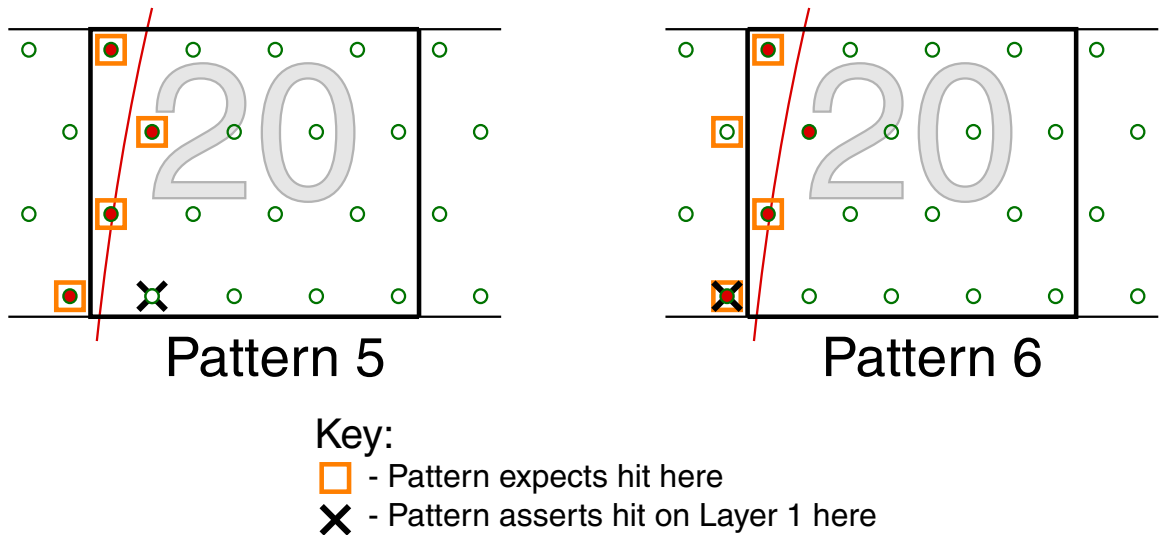


Figure 4.11: Continuing with the example in Figure 4.10, we have four wires hit in/near block 20. In this case, two different patterns are satisfied (pattern 5 has four out of four wires hit while pattern 6 has only three out of four wires hit). In this case there is a problem because the two different patterns would set two different blocks as being hit, violating the second constraint.

we share the some of the inputs of wires on each TQT board with their neighbors.

4.7.3 Stereo Trigger Tracks

Before talking about how we find the stereo tracks, let us review the purpose of the Stereo Trigger. Given the pattern of the blocks hit, we want to have the best estimate of where the track was in the axial part of the drift chamber and where the track is going into the calorimeter. In addition, we want to know whether we have a low momentum positively charged track, a low momentum negatively charged track, or a high momentum track.

To accomplish this, we generated 50,000,000 tracks of varying θ (angle from beam pipe), ϕ (as measured in the x - y plane) and transverse momentum (from 250 MeV to 5 GeV) using the trigger simulation with perfect wire efficiency and only one hit per layer (see Section 4.7.1 above).

Since the U layers and the V layers are tilted in opposite directions, they are analyzed separately. A stereo track, therefore, consists of four U layer blocks or four V layer blocks. For each stereo pattern (i.e. 4 U layer blocks or 4 V layer blocks), we want to record what type of tracks hit it (e.g. charge of track, transverse momentum, where they track hit in the axial section of the DR, where the track enters the calorimeter).

The last step is to use the symmetry of the stereo section of the drift chamber to effectively increase statistics. As shown in Figure 4.12, there is a three-fold symmetry in the stereo portion. Within each third, there is mirror symmetry. In other words, for every track that we generated with the trigger simulation, we gain information: 6 U patterns and 6 V patterns. Consider U stereo pattern superlayer 1 block 1, superlayer 3 block 2, superlayer 5 block 3, and superlayer 7 block 5 (henceforth known as 1-2-3-5)⁹ also gives information about patterns 16-21-26-32 and 31-40-49-59. Each of the three above patterns has a reflection: $1-2-3-5 \Rightarrow 15-18-21-23$, $16-21-26-32 \Rightarrow 30-37-44-50$, and $31-40-49-59 \Rightarrow 45-56-67-77$.

For bookkeeping purposes, every pattern organized by the third out of four numbers (e.g. U pattern 1-2-3-5 is ordered under '3'). Given such organization, there 69 such groups for the U super layers and 75 groups for the V superlayers, each group with approximately 30 patterns. To accommodate the number of patterns, we have split the patterns into 6 U boards and 6 V boards (see Figure 4.12).

4.7.4 Maintenance

Maintenance of the stereo trigger falls into two categories. First, making sure the trigger gets the signals it is supposed to be getting and second, given the right inputs, making sure the trigger produced the right outputs.

⁹For clarity, for a U pattern A-B-C-D means superlayer 1 block A, superlayer 3 block B, superlayer 5 block C, and superlayer 7 block D. For a V pattern, it would mean superlayer 2 block A, superlayer 4 block B, superlayer 6 block C, and superlayer 8 block D.

The Inputs

There are two methods for making sure that the right inputs are getting to the STTR. The first, which is done when we are not taking data, is to go around the drift chamber and turn on each block one at a time and make sure that the STTR receives the information that the right block and only the right block is on.

The second method is slightly more complicated and is done with the data collecting during running conditions. Before talking about this method, we need to talk about the exact inputs into the STTR boards. As mentioned above, each TQT board corresponds to 4 layers by 12 wires and sends three inputs corresponding to three stereo blocks. In addition, each TQT sends four “efficiency” bits. Since we do not send each wire to the stereo trigger, it is much more difficult to find out if one of the wires in the TQT is not firing. The efficiency bits are a way around this problem. Each bit is a logical OR of the twelve wires in each of the four layers.

In order to look at the wire-by-wire efficiencies, we look at events with reconstructed tracks¹⁰. We then go through and look at every hit on that track that is in the stereo section of the drift chamber and place it into one of two histograms: the “good” histogram if the corresponding efficiency bit is set and the “bad” histogram if the bit is not set. You will occasionally get good hits for a dead wire, but looking over a run of 150,000 events (an average run), we can find most problem wires.

The Outputs

To check the outputs of the STTR, there are again two methods. First, we can look at the inputs to the STTR and the inputs of the TRCR (which are the outputs of the STTR) and make sure that the outputs of the STTR are what they should be based on the inputs. Second, we can load test patterns into the circular buffers and push them through the logic section of the board. By reading out the outputs, we

¹⁰We look only at hits on tracks instead of all hits to reduce using hits that are due to noise instead of charged particles from the event recorded.

can check that everything is working properly.

STTR Block and TQT Map

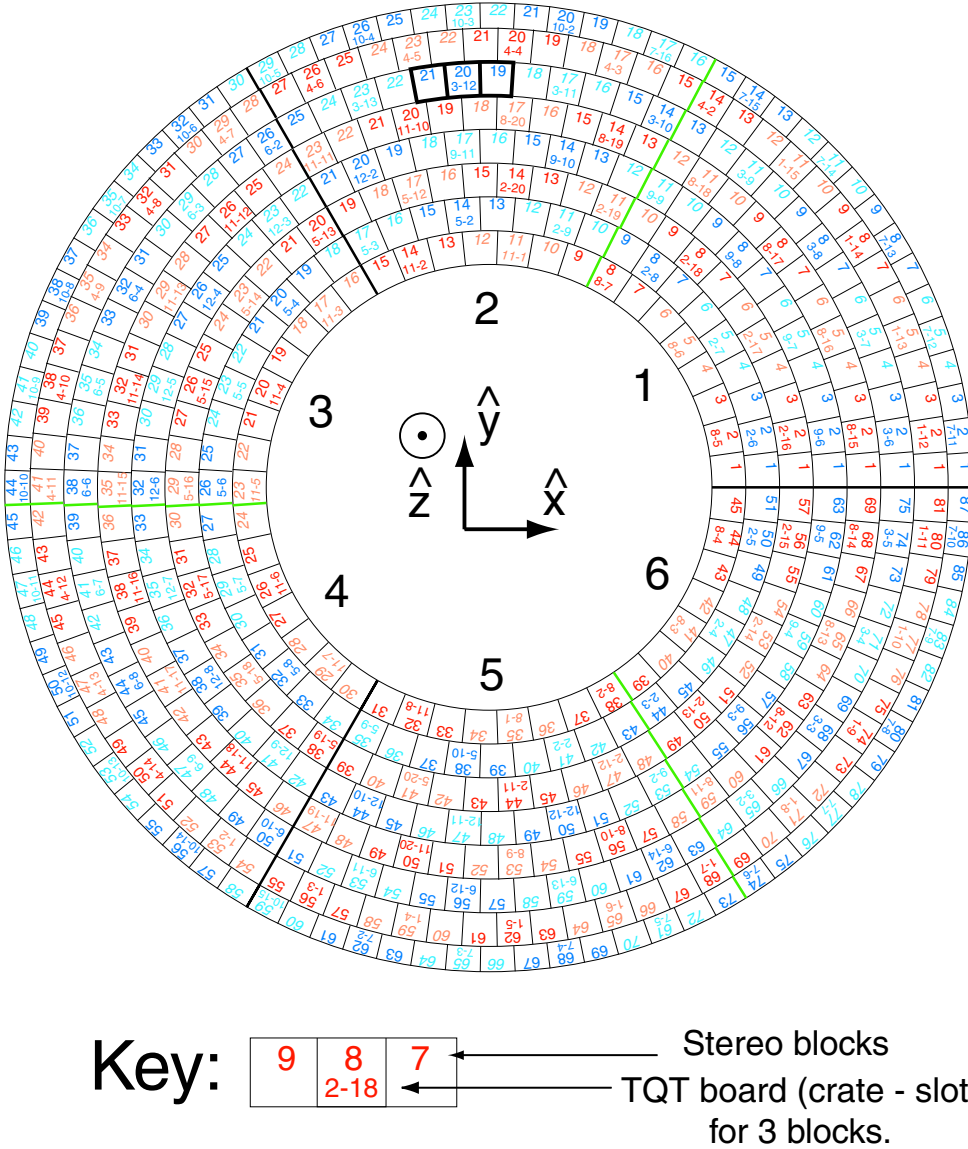


Figure 4.12: The map of stereo blocks (U super layers in red; V superlayers in blue). The beam pipe is coming out of the middle of the circle (along \hat{z}). Each three blocks gets its signal from a TQT board. Superlayer 6 blocks 19 through 21 are highlighted since they are the example in Figure 4.10. The three thick black lines (at 3 o'clock, 7 o'clock and 11 o'clock) are boundaries of the three-fold symmetry as well as STTR board boundaries. The thick green lines are STTR board boundaries. The numbers "1" through "6" on the inside refer to the regions covered by the stereo boards (6 U boards and 6 V boards).

Chapter 5

Final Remarks

Using the $9fb^{-1}$ data sample collected with the CLEO II.V detector at the Cornell Electron Storage Ring, we study the resonant substructure of the Cabibbo suppressed decay $D^0 \rightarrow \pi^+\pi^-\pi^0$. We observe significant contributions from the $\rho^-\pi^+$, $\rho^+\pi^-$, $\rho^0\pi^0$, and non-resonant channels, and present results of the amplitudes, phases, and fit fractions for these and other sub-modes. No significant evidence for the $\sigma(500)$ or any other resonance was found. \mathcal{A}_{CP} has been measured as $0.01^{+0.09}_{-0.07} \pm 0.09$.

The CLEO III trigger has been successfully running for over three years. It has been very reliable, checking every 42 *ns* for interesting physics.

Appendix A

Driver++ Analysis Tools

In this chapter I will talk about the standard analysis tools for CLEO and my additions to these tools that I call “Driver++”.

A.1 Driver

The standard analysis package for CLEO II and CLEO II.V is Driver, a FORTRAN based package that stores all its information in common blocks¹. When a user wants to write a piece of analysis code, she writes five subroutines that are called at various times.

ANAL1 is called first at the beginning of every analysis job and is usually used to open any output sources (histogram files, etc) that are used to store the results of the analysis. ANAL2 is called at the beginning of every data run² and is used to fill the common blocks with information as run energy. ANAL3 is called every event and is the main part of any analysis job. This is where reconstructed tracks are combined into candidates, etc. ANAL4, called at the end of every data run, is rarely used³. ANAL5, called at the end of the analysis job, is generally used to close any

¹A common block is just a group of variables in a contiguous block of computer memory.

²When running, data collecting is usually split into different “data runs” that last about an hour. While CLEO does take data at different energies, a given data run is at a unique energy.

³It is common practice to run over many different data runs at once and store all of the output in one histogram file. In certain situations, one may want to create one histogram file for every data

files opened in ANAL1.

A.2 C++ access to FORTRAN common blocks

Running C++ code from FORTRAN and vice versa is a relatively common and well understood procedure. The problem in trying to use C++ to do data analysis with Driver was that access to the common blocks didn't exist. Common blocks are defined in include files (".inc"). The definition of the common blocks includes a list of the variables as well as their types (e.g. integer, real) and sizes (e.g. single and multi-dimensional arrays).

To get access to the variables defined in the common blocks, I wrote a Perl script named "inc2h⁴" which reads the include files, learns about the common blocks, and then writes code to be compiled (both C++ and Fortran). One of the biggest problems when trying to get access to these variables is that we are not guaranteed where in memory the common block variables lie (this is highly compiler dependent). To get around this problem, I took advantage of the fact that FORTRAN passes all variables by address instead of by value. I simply initialize each common block by asking a FORTRAN subroutine for the memory address of each variable.

The final question that needed to be answered about common blocks is which ones to get access to and how to fill them. This has been a long-standing problem in CLEO II analyses and I borrowed the solution as presented to me by Mark Palmer (former Illinois research postdoctoral fellow). His solution was to have one include file that included all of the common blocks that could be needed and one fortran subroutine that made sure that all of these common blocks were properly filled in ANAL3⁵.

run. In this case, the histogram files would be opened in ANAL2 and closed in ANAL4.

⁴This script is currently used not only for Driver++, but for Suez, the CLEO III analysis software package as well.

⁵As one might imagine, these two files have evolved and grown over the years as people used more and more tools to do analyses

A.3 Additional Tools

To run driver from a C++ environment was very simple after getting access to the common blocks. A standard FORTRAN analysis job was made up of a file called “ANAL.F” that included the 5 ANAL subroutines. In my new environment, I still have a file called “ANAL.F” that includes ANAL1, ANAL2, ANAL4 and ANAL5. At the end of each of these subroutines, they call their own ANALnc (e.g. ANAL1 calls “anal1c”) subroutine so I can access all of these from C++. ANAL3 is now defined in a C++ file “anal3.cc”.

Once I was able to use C++ to do analysis, I was free to create new C++ tools to help. I created a base class called “Particle”, and derived classes for reconstructed charged particles (“ChargedParticle”), π^0 s (“PiZero”) and showers (“Photon”). One of the biggest advantages of this class structure is we now have very similar ways of accessing that is essentially the same information from different types of particles. For example, getting the four momentum for a π^0 candidate is exactly the same as getting it from a charged particle.

Driver++ grew out of necessity. As I needed more features, I wrote more classes. One of the most useful classes that I created was “QQDecayChain” (which, incidentally, was possible due to the fact that the three particle types are all derived from a single base class). As mentioned in the Introduction (see Section 2.4), for every MC event, we can look and see what the decay tree was for that event. It is also possible to match reconstructed tracks with QQ generated tracks. With these two types of information, it is possible to not only check if a particular decay is present, but whether you have correctly reconstructed that decay or not.

Before QQDecayChain, every time somebody wanted to tag a decay, they had to write a separate subroutine to first see if that decay is in fact present, and another subroutine to see if they reconstructed the right decay. With QQDecayChain, each new decay just took a couple of lines of code and even let us look for decays where

one of the particles was unknown.

This last feature was necessary when I was using generic MC to evaluate background sidebands (see Section 3.6), as we wanted to be able to remove all signal events to study what the background in the signal region looked like. Since we do not know exactly how the generic MC was generated (e.g. specifically which resonances were present), the only way to make sure we found them all was to look for decays with unknown X:

$$\begin{array}{l}
 D^{*+} \rightarrow D^0 \pi_{slow}^+ \\
 \quad \quad \quad \searrow \\
 \quad \quad \quad X^0 \pi^0 \\
 \quad \quad \quad \quad \quad \searrow \\
 \quad \quad \quad \quad \quad \pi^+ \pi^-
 \end{array}$$

where X could be a ρ , K_S^0 , etc. This ability was very important because unless one knows all of the resonances used when the MC was generated, there is no way to be sure that you have removed all signal from the MC background samples, for example.

The final tool that will be mentioned is my “makeHbook” utility. In standard Driver, users had to very carefully create and fill their own histograms and ntuples⁶. One of the most common mistakes with ntuples is assigning the label of “momentum” to array element 4, for example, and filling the values of “momentum” in element 5.

With “makeHbook”, the user creates a commented list that describes all ntuples and histograms that she wants created. “makeHbook” then creates the necessary FORTRAN and C++ code to automatically book the ntuples and makes filling them very easy. Using the above example, the user would assign a value to the ntuple by typing

```
ntuple_example.momentum() = 3.0;
```

⁶A histogram keeps track of a distribution of one number. When setting it up, one must specify the lower and upper limits as well as the number of bins. Every time a histogram is filled, one of the bin counters is incremented. An ntuple is a group of (up to 512) numbers. Every time it is filled, the tuple of numbers is stored. Ntuples are very useful for looking at correlations while histograms take up very little space.

down on errors committed while filling ntuples.

The last feature of “makeHbook” that I want to discuss is structures. Given that users often want to store the same information for multiple particles, candidates, etc., it made sense to let users copy a structure of variables. For example, let’s say a user wants to keep track of momentum, charge, and quality for 10 different particles. She could simply write the following:

```
group {
    mom ! magnitude of momentum
    chg ! sign of the charged track
    qul ! 0 if it is a good track, else an error code
}

one_[mom] ! definition of the first particle
two_[mom] ! definition of second particle
:
ten_[mom] ! definition of tenth particle
```

where she would access the momentum of the second particle by

```
ntuple_example.two_mom() = 2.0;
```

Appendix B

Block patterns for the Stereo Trigger

B.1 The Patterns

There are 14 valid patterns for blocks superlayers 1 through 7. superlayer 8 will be discussed below in Section B.2. The fourteen patterns are shown in Figure B.1. In order to figure out how to modify the patterns to avoid having two blocks hit at the same time, we must first look at the overlap. See Table B.1 to see the overlap between patterns. Given these overlaps, we made the restrictions on each pattern as shown in Table B.2.

B.2 Superlayer 8

For those of you paying particularly good attention, you will have realized that with only 31 wires in the stereo section of the CLEO III drift chamber, it isn't possible to have 8 superlayers of 4 layers each. As it was designed, superlayer 8 only has 3 layers. Instead of a block being hit when three out of four wires are hit, a block in superlayer 8 is on when two out of three layers are hit. There is a different set of patterns (albeit found exactly the same way as for superlayers 1 through 7) as well as a different set of conflicts and pattern exclusions. The patterns are shown in B.2, the table of conflicts shown on Table B.3 and the exclusions shown on Table B.4.

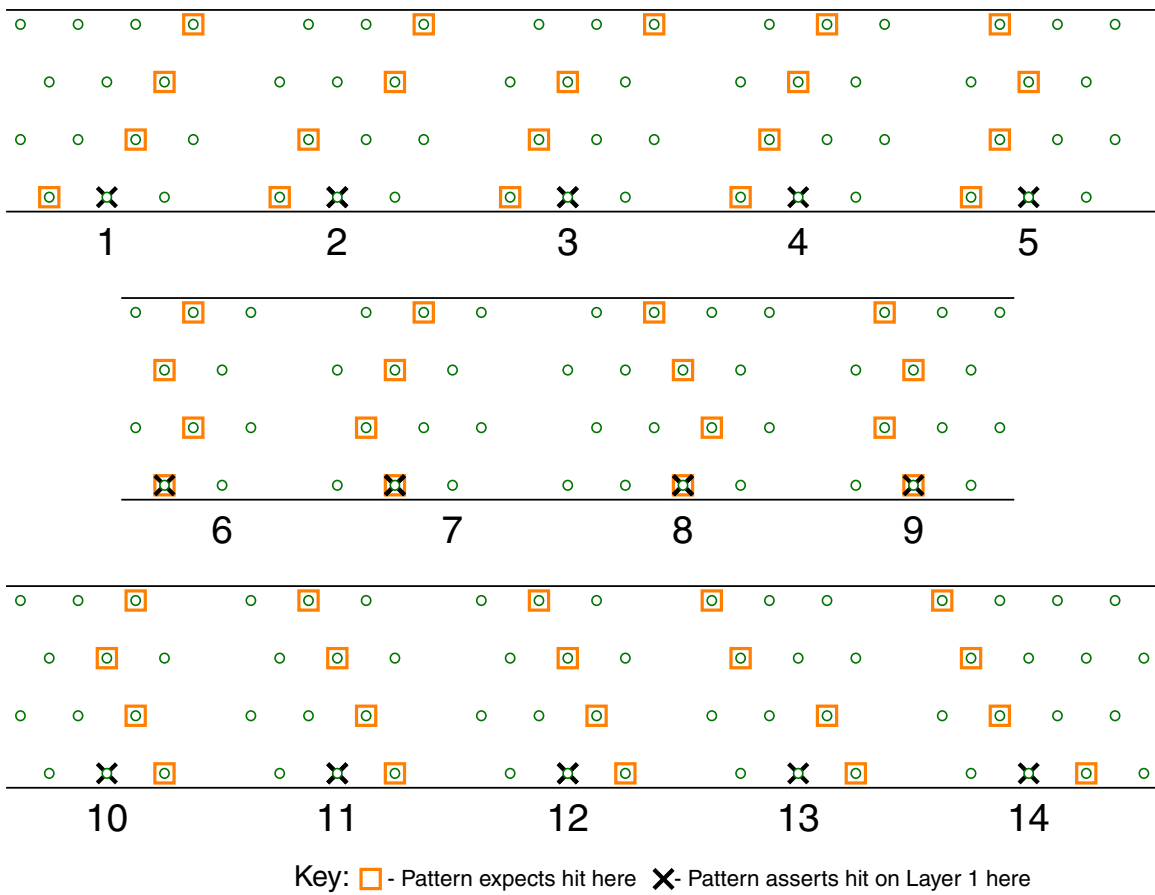


Figure B.1: The fourteen patterns for super layers 1 through 7.

	1	2	3	4	5	6	7	8	9	10	11	12	13	14
14								a			a		2	*
13												c	*	2
12										d	d	*	c	
11								a		d	*	d		a
10						a			3	*	d	d		
9					a		d	b	*	3				
8						d		*	b		a			a
7	a			a		b	*		d					
6					3	*	b	d		a				
5			d	d	*	3			a					
4	a		d	*	d		a							
3		c	*	d	d									
2	2	*	c											
1	*	2		a			a							

	Key
*	Looking at pattern with itself
a-d	Non-conflicting overlap with layer 1-4 (respectively) missing
1-4	Conflicting overlap with layer 1-4 missing

Table B.1: We have the overlap of the patterns above. Conflicting means that the two patterns will set off different layer 1 wires. Non-conflicting means that the patterns will set off the same layer 1 wire.

Pattern	Exclusions
1	None
2	Wire 2 missing or no wires are missing
3	Wire 3 missing
4	None
5	Wire 1 missing
6	Wire 3 missing or no wires missing
7	Wire 2 or wire 4 missing
8	Wire 2 or wire 4 missing
9	Wire 3 missing or no wires missing
10	Wire 1 missing
11	None
12	Wire 3 missing
13	Wire 2 missing or no wires are missing
14	None

Table B.2: The exclusions of stereo block patterns. “None” means that all five possibilities of the patterns are used (again, the five possibilities are: All four wires are hit, wire one is missing (i.e. wires two, three, and four are hit, but wire one is not), wire two is missing, wire three is missing, and wire four is missing.). “Wire 3 missing” means that all possibilities are used except where the third wire is missing. “Wire 3 missing or no wires missing” means that this pattern is only satisfied if the “Wire 1 missing”, “Wire 2 missing”, or the “Wire 4 missing” possibilities are satisfied. It is *not* satisfied if either the “Wire 3” possibility or “All 4 layers” possibility are satisfied.

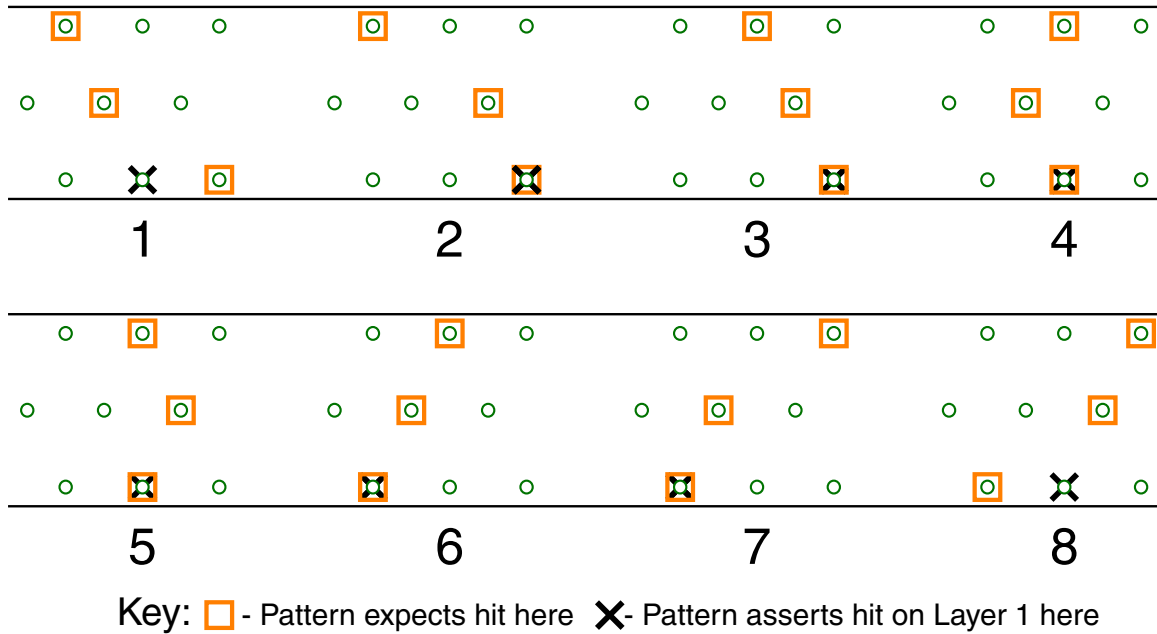


Figure B.2: The eight patterns for super layer 8.

	1	2	3	4	5	6	7	8
8				1		a	2	*
7					c	c	*	2
6				1	c	*	c	a
5	1		1	b	*	c	c	
4		c	c	*	b	1		1
3	a	c	*	c	1			
2	2	*	c	c				
1	*	2	a		1			

Key	
*	Looking at pattern with itself
a-d	Non-conflicting overlap with layer 1-4 (respectively) missing
1-4	Conflicting overlap with layer 1-4 missing

Table B.3: The exclusions of stereo block patterns for superlayer 8. See Table B.1 for explanation.

Pattern	Exclusions
1	Wire 1 missing or wire 2 missing or no wires missing
2	Wire 3 missing
3	Wire 1 missing or no wires missing
4	Wire 3 missing
5	Wire 3 missing
6	Wire 1 missing or no wires missing
7	Wire 3 missing
8	Wire 1 missing or wire 2 missing or no wires missing

Table B.4: The exclusions of stereo block patterns for superlayer 8. See Table B.2 for explanation of terms.

References

- [1] Particle Data Group, Phys. Rev. D. **66** (2002)
- [2] Q. Ahmad et al., (SNO Collaboration), nucl-ex/0204009.
- [3] David Griffiths, *Introduction to Elementary Particles*, New York, John Wiley and Sons (1987)
- [4] M. Gell-Mann and A. Pais, Phys. Rev. **97**, 1387 (1955)
- [5] J. H. Christenson et al., Phys. Rev. Lett. **13**, 138 (1964)
- [6] K. Abe *et al.*, arHiv:hep-ex/0208025
- [7] B. Aubert *et al.*, Phys. Rev. Lett. **87**, 091801
- [8] B. Aubert *et al.*, Phys. Rev. Lett. **88**, 231801
- [9] F. Wilczek, Scientific American (December 1980)
- [10] Conversations with and lectures from Scott Willenbrock.
- [11] Y. Kubota *et al.*, Nucl. Instrum. Methods Phys. Res. **A 320**, 66 (1992).
- [12] CESR and CLEO Staff, CLNS **93/1265** (1993). <http://www.lns.cornell.edu/public/CLNS/CLEO.html>
- [13] T.S. Hill, Nucl. Instrum. Methods Phys. Res. **A 418**, 32 (1998); D. Peterson, Nucl. Phys. **B** (Proc. Suppl.) **54B**, 31 (1997).

- [14] http://wwwinfo.cern.ch/asdoc/geant_html3/geantall.html
- [15] CLEO Collaboration, “The CLEOIII Detector: Design and Physics Goals”, CLNS 94/1277.
- [16] D. Bortoletto, *et al.*, Nucl. Instrum. Methods Phys. Res. **A 320**, 114 (1992).
- [17] C. Bebek, *et al.*, Nucl. Instrum. Methods Phys. Res. **A 302**, 261 (1991).
- [18] S. Kopp *et al.*, Physical Review D **63**, 092001 (2001)
- [19] C. Gobel, arXiv:hep-ex/0012009
- [20] F. Buccella, M. Lusignoli, and A. Pugliese, Phys. Lett. B **379**, 249 (1996)
- [21] P. Santorelli, arXiv:hep-ph/9608236
- [22] J. Blatt and V. Weisskopf, *Theoretical Nuclear Physics*, New York, John Wiley and Sons (1987)
- [23] H. Pilkuhn, *The Interactions of Hadrons*, Amsterdam: North-Holland(1967)
- [24] A. Weinstein, CBX 99-55 (unpublished).

Vita

Charles Plager was born in Chicago, Illinois on June 11, 1970. He graduated college with a B.S. in Mathematics, Physics, and Psychology from the University of Illinois in 1992. After receiving his Masters degree in Physics in 1995, he moved from the state of Illinois (where he had lived his whole life) to Africa, where he was a Peace Corps volunteer for two years. In 1997, he moved back to Champaign-Urbana and started working on the CLEO experiment with Prof. Mats Selen. In the fall of 1998, he moved out to the Cornell Univeristy campus in Ithaca, NY to be “on-site” at the CLEO experiment, where he stayed until a few months before he graduated.